

**NUMERICAL SIMULATION OF MIXED CONVECTION OVER  
A THREE-DIMENSIONAL HORIZONTAL  
BACKWARD-FACING STEP**

A Dissertation

by

JUAN GABRIEL BARBOSA SALDANA

Submitted to the Office of Graduate Studies of  
Texas A&M University  
in partial fulfillment of the requirements for the degree of

DOCTOR OF PHILOSOPHY

May 2005

Major Subject: Interdisciplinary Engineering

© 2005

JUAN GABRIEL BARBOSA SALDANA

ALL RIGHTS RESERVED

**NUMERICAL SIMULATION OF MIXED CONVECTION OVER  
A THREE-DIMENSIONAL HORIZONTAL  
BACKWARD-FACING STEP**

A Dissertation

by

JUAN GABRIEL BARBOSA SALDANA

Submitted to Texas A&M University  
in partial fulfillment of the requirements  
for the degree of

DOCTOR OF PHILOSOPHY

Approved as to style and content by:

---

Nagamangala K. Anand  
(Co-Chair of Committee)

---

Vivek Sarin  
(Co-Chair of Committee)

---

Sai C. Lau  
(Member)

---

Valerie E. Taylor  
(Member)

---

Nagamangala K. Anand  
(Head of Department)

May 2005

Major Subject: Interdisciplinary Engineering

## ABSTRACT

Numerical Simulation of Mixed Convection over a Three-Dimensional Horizontal  
Backward-Facing Step. (May 2005)

Juan Gabriel Barbosa Saldana, B.S.; M.S., National Polytechnic Institute, Mexico

Co-Chairs of Advisory Committee: Dr. Nagamangala K. Anand  
Dr. Vivek Sarin

A FORTRAN code was developed to numerically simulate the mixed convective flow over a three-dimensional horizontal backward-facing step. The momentum and energy equations under the assumption of the Boussinesq approximation were discretized by means of a finite volume technique. The SIMPLE algorithm scheme was applied to link the pressure and velocity fields inside the domain while an OpenMP parallel implementation was proposed to improve the numerical performance and to accelerate the numerical solution.

The heating process corresponds to a channel heated from below at constant temperature keeping insulated all the other channel walls. In addition, the back-step was considered as a thermally conducting block and its influence in the heating process was explored by holding different solid to fluid thermal conductivity ratios.

The effects over the velocity and temperature distribution of buoyancy forces, acting perpendicular to the mainstream flow, are studied for three different Richardson numbers  $Ri=3$ , 2, and 1 and the results are compared against those of pure forced convection  $Ri=0$ . In these simulations the Reynolds number is fixed at 200 while the

bottom wall temperature is adjusted to fulfill the conditions for the different  $Ri$ . Under this assumption, as  $Ri$  increases the buoyancy effects are the dominant effects in the mixed convective process.

The numerical results indicate that the velocity field and the temperature distribution for pure forced convection are highly distorted if compared with the mixed convective flow. If the  $Ri$  parameter is increased, then the primary re-circulation zone is reduced. Similarly, as the buoyancy forces become predominant in the flow, the convective rolls, in the form of spiral-flow structures, become curlier and then higher velocity components are found inside the domain.

The temperature field distribution showed that as the  $Ri$  is increased a thicker layer of high temperature flow is located at the channel's top wall as a result of the higher rates of low-density flow moving to the top wall. The flow is ascending by the channel sidewalls, while descending by the channel span-wise central plane.

The parallel numerical strategy is presented and some results for the performance of the OpenMP implementation are included. In this sense, linear speedup was obtained when using 16 processors in parallel.

To my parents *Raquel Saldana* and *Luis Barbosa*,  
my brother *Luis Enrique*,  
my sisters *Zoila Beatriz* and *Maria de Lourdes*,  
my nieces *Jeaninne*, *Linnette Xiadani*, and *Raquel Iyali*.

Thanks, *MY LORD GOD*, for the gift of breathing.

Thanks, *MY LORD GOD*, for the gift of giving me my FAMILY.

## ACKNOWLEDGEMENTS

I would like to express my deepest appreciation to Dr. N.K. Anand for his guidance through these four years of my doctoral studies. His patience, confidence and encouragement helped me to successfully complete this research. I will always be in debt to him for his professional support and for his wise words. My sincere gratitude goes to Dr. Vivek Sarin, who served as co-chair of this project and assisted and counseled me to make this an interdisciplinary research project. Gratitude is extended to committee members Dr. Valerie Taylor and Dr. Sai Lau for their suggestions concerning this dissertation.

This project would not have been possible without the support of my family. I am grateful to them for their love, encouragement, and prayers. Thanks for filling my life every Sunday with your voice.

I also express my thankfulness to Claudia and Jose Alfredo, for all the moments, and best of all, for all that is still in the future. I wish to thank all my friends who believed in me and showed me their warmth and friendship through the mail.

My friendship and gratitude go to Kang-Hoon Ko, Bruno Miranda, and Haitham for sharing the Numerical Heat Transfer Laboratory, and for sharing their experience and understanding in the complicated but amazing world of the numerical simulation. Thanks for all that camaraderie at Texas A&M.

Also I want to say thanks to Nagesh, from the supercomputer help desk at Texas A&M University, and to Hemant for making my experience with the supercomputers a lot easier.

I want to extend my gratefulness to the staff of the Mechanical Engineering Department for their kindness and help provided during my studies at Texas A&M University, specially to Mrs. Kim Moses.

Finally I am delighted and grateful to the ANUIES-Mexico and the SUPERA program for their scholarship and financial help during three years of my doctoral program at Texas A&M University. Gratitude is extended to my alma mater the National Polytechnic Institute (IPN) in Mexico.



## TABLE OF CONTENTS

	Page
ABSTRACT.....	iii
DEDICATION.....	v
ACKNOWLEDGEMENTS.....	vi
TABLE OF CONTENTS.....	viii
LIST OF FIGURES.....	xi
LIST OF TABLES.....	xiv
NOMENCLATURE.....	xv
 CHAPTER	
I INTRODUCTION.....	1
1.1 Background.....	1
1.2 Motivation.....	7
1.3 Objectives.....	8
1.4 Dissertation Outline.....	9
II PRIOR WORK.....	11
2.1 Literature Survey.....	11
III MATHEMATICAL MODEL.....	27
3.1 Introduction.....	27
3.2 Basic Equations.....	29
3.2.1 Forced Convection.....	31
3.2.2 Free Convection or Buoyancy Induced Flow.....	33
3.2.3 Mixed Convection.....	38
IV NUMERICAL PROCEDURE.....	40
4.1 Introduction.....	40

CHAPTER	Page
4.2 The General Transport Equation.....	41
4.3 Finite Volume Discretization Technique.....	42
4.4 Fluid Flow Computation SIMPLE Algorithm.....	50
4.5 Staggered Grid.....	55
4.6 Line-by-line Tri-Diagonal Matrix Algorithm (TDMA).....	61
 V VALIDATION AND GRID INDEPENDENCE.....	 63
5.1 Introduction.....	63
5.2 Numerical Validation.....	63
5.2.1 Forced Convective Flow through a Square Horizontal Channel.....	 64
5.2.2 Mixed Convective Flow through a Rectangular Horizontal Channel.....	 68
5.2.3 Forced Convective Flow over a Three-Dimensional Horizontal Backward-Facing Step.....	 69
5.3 Grid Setup.....	75
5.4 Grid Independence Study.....	82
 VI PARALLEL IMPLEMENTATION.....	 88
6.1 Introduction.....	88
6.2 Parallel Architecture and OpenMP.....	89
6.2.1 Parallel Architecture.....	89
6.2.2 OpenMP.....	91
6.2.3 Parallel Computing Performance Measurement.....	94
6.3 Parallel Implementation.....	96
6.4 Parallel Performance.....	101
 VII RESULTS AND DISCUSSION.....	 111
7.1 Introduction.....	111
7.2 Numerical Procedure and Boundary Conditions.....	112
7.3 Convergence Criteria.....	114
7.4 Physical Parameters and Definitions.....	115
7.5 Effects of Varying the Richardson Number.....	117
7.5.1 The $x_u$ -line, Averaged Nusselt Number and Averaged Shear Stress.....	 118
7.5.2 Development of the Three-Velocity Components under Mixed Convective Flow Conditions.....	 125

CHAPTER	Page
7.5.3 Temperature Fields for the Mixed Convective and Pure Forced Convective Flow.....	137
7.6 Impact of the Backward-Facing Step Thermal Conductivity on the Mixed Convective Flow.....	142
VIII CONCLUSIONS.....	145
REFERENCES.....	148
VITA.....	156

## LIST OF FIGURES

FIGURE	Page
1.1 Three-dimensional backward-facing step.....	4
1.2 Flow over a backward facing step.....	5
3.1 Pure forced convective flow in a horizontal channel.....	31
3.2 Pure free convective flow for a quiescent fluid.....	33
3.3 Convective circulation patterns for buoyancy induced flow.....	35
4.1 Volume element surrounded by its neighbor grid points.....	44
4.2 Convection-diffusion fluxes at the faces of the control volume.....	47
4.3 Staggered grid for u-velocity component at a constant z-plane.....	57
4.4 Staggered grid for v-velocity component at a constant z-plane.....	58
4.5 Staggered grid for w-velocity component at a constant x-plane.....	59
4.6 Staggered grid in a three-dimensional geometry.....	60
5.1 Nusselt number and Fanning friction factor distributions averaged in the span-wise direction for forced convective flow through a square channel.....	66
5.2 Stream-wise velocity profile along the central plane for a forced convective flow through a square channel.....	67
5.3 Span-wise averaged Nusselt number distribution for a mixed convective flow in a rectangular channel heated from below and top at a constant temperature...70	70
5.4 Span-wise averaged Nusselt number distribution for a mixed convective flow in a rectangular channel heated from below at a constant heat flux.....	71

FIGURE	Page
5.5	Span-wise $x_u$ -line distribution adjacent to the bottom wall.....73
5.6	Span-wise u-velocity component distributions at different transverse planes for Re=343.....74
5.7	Local Nusselt number distribution for a forced convective flow over a three-dimensional backward-facing step along the stepped wall at $x/s=6.6$ plane.....76
5.8	Non-uniform grid setup for the x-direction in a constant y-plane.....79
5.9	Non-uniform grid for z-coordinate direction at a constant x-plane.....80
5.10	Non-uniform grid for y-direction at a constant z-plane.....82
6.1	Distributed memory architecture (DMA).....90
6.2	Shared memory architecture (SMA).....91
6.3	Application-programming interface for OpenMP.....93
6.4	Fork-join model execution for OpenMP.....94
6.5	Flow chart for the numerical d code.....97
6.6	Collection of planes for the three-dimensional computational domain in the stream-wise direction.....99
6.7	Distribution of i-planes for an OpenMP parallel implementation.....102
6.8	Total time for test 1 on AGAVE.....104
6.9	Speedup vs. P test 1 on AGAVE.....104
6.10	Efficiency vs. P test 1 on AGAVE.....105
6.11	Speedup for different grid size test 2 on COPPER.....106

FIGURE	Page
6.12 Efficiency for different grid size test 2 on COPPER.....	107
6.13 CPU computing time for a full run, test 3 on COPPER.....	109
7.1 $x_u$ -line distribution for different Ri and for pure forced convection.....	119
7.2 Flow structures for a forced convective flow.....	120
7.3 Flow structures for a mixed convective flow Ri=1.....	121
7.4 Flow structures for a mixed convective flow Ri=2.....	121
7.5 Flow structures for a mixed convective flow Ri=3.....	122
7.6 Averaged shear stress $\tau_{wx}$ for different Ri and pure forced convection.....	123
7.7 Averaged Nusselt number distribution.....	124
7.8 u-velocity component at central plane $z/W=0.5$ at different x-planes.....	126
7.9 u-velocity profile at the channel exit at two different $z/W$ planes Ri=3.....	129
7.10 v-velocity component for different Ri at constants x- and y-planes.....	131
7.11 w-velocity profile at different x- and y-planes.....	133
7.12 w-velocity component at a constant span-wise plane ( $z/W=0.015$ ).....	135
7.13 w-velocity component at a constant span-wise plane ( $z/W=0.93$ ).....	136
7.14 Temperature distribution for Ri=3 at different x-, y- and z-constant planes.....	138
7.15 Temperature distribution for Ri=2 at different x-, y- and z-constant planes.....	139
7.16 Temperature distribution for Ri=1 at different x-, y- and z-constant planes.....	140
7.17 Temperature distribution for Ri=0 at different x-, y- and z-constant planes.....	141
7.18 Temperature contours inside the backward-facing step for different thermal conductivities at the z-central plane.....	144

**LIST OF TABLES**

TABLE	Page
4.1	Variables for the general transport equation.....42
5.1	Validation for a forced convective flow through a square channel.....66
5.2	Grid independence study for the z-coordinate direction. Effects on $e_z$ .....84
5.3	Grid independence study for the z-coordinate direction. Effects on the $n_z$ .....85
5.4	Grid independence study for the y-coordinate direction.....85
5.5	Grid independence study for the x-coordinate direction.....86
6.1	Parallel performance, test 1 on AGAVE 5000 iterations.....103
6.2	Parallel performance, test 2 on COPPER.....106
6.3	Differences for the computed values.....108
6.4	CPU computing time and speedup, test 3 on COPPER.....109

## NOMENCLATURE

A	Area
AR	Aspect ratio
B	Buoyancy force, front node
b	front face
CV	Control volume
C <sub>p</sub>	Specific heat
D	Diffusive flux
D <sub>h</sub>	Hydraulic diameter
E	East node, efficiency
ER	Expansion ratio
e	east facec
F	Convective flux
Gr	Grashof number
Gr*	Modified Grashof number
g	gravity acceleration
k	Thermal conductivity
S	South node, speedup
s	Step height
2H	Channel height
L	Total length channel



l	Channel length
N	North node
n	north face
Nu	Nusselt number
P	Nodal point, number of processors
p	Pressure
Pr	Prandtl number
R	Gas constant, residuals
Re	Reynolds number
Ri	Richardson number
S	South node, Source
s	South face
T	Temperature, back node
t	back face
$t_p$	time parallel
$t_1$	Time single processor
u	u-velocity component
V	Volume
v	v-velocity component
W	West node
w	w-velocity component, west face
x	x-coordinate direction

y y-coordinate direction

z z-coordinate direction

***Greek letters***

$\beta$  Thermal expansion coefficient

$\nu$  Kinematic viscosity

$\phi$  Generalized variable

$\mu$  Dynamic viscosity

$\delta$  Diffusion length

$\Gamma$  Diffusion coefficient

$\rho$  Density

$\tau$  Shear stress

$\infty$  Reference value

***Subscripts***

avg average

e exit

f Fluid

s Solid

$\phi$  General variable

# CHAPTER I

## INTRODUCTION

### 1.1 Background

Besides the experimental and theoretical approaches, numerical simulation has established itself as the most practical and viable alternative to study and to understand different engineering problems. However, numerical simulations would not be possible without the recent developments and improvements in computers in terms of memory size and computing speed. Today's supercomputers have memory capacities as much as one million megabytes (*one terabyte*) and are capable of performing one trillion arithmetic operations per second ( $1 \times 10^{12}$  FLOPS). Just in the last 50 years the speed of digital computers has increased by more than a trillion times [1].

As the power of supercomputers have increased in terms of computing speed and memory capacity, the accuracy of numerical simulations for physical problems has also increased by adding more complexity to the laws governing the phenomenon or by adding more discretization points to the simulation. In this sense accurate, fast, and economical solutions for basically any scientific and engineering problem can be achieved by using numerical simulation techniques and supercomputers.

The implementation of numerical simulation avoids not only the annoying measurement in full-scale experimental setups, but also the prohibitively expensive and

---

This dissertation follows the style and format of the ASME Journal of Heat Transfer.

at times impossible construction of such devices. On the other hand, the use of theoretical tools to solve such problems is limited and cumbersome thus precludes reaching the final solution. In contrast numerical simulations are possible only after the complete mathematical description of the physical phenomenon is done and often experimental measurements are needed in order to verify the accuracy of the numerical results. In this sense some numerical followers define the numerical simulation as the modern approach, which joins the theoretical and experimental approaches for studying a physical phenomenon [2].

Currently, numerical simulation is employed in several scientific, engineering and industrial areas, e.g. analysis of stability in mechanical structures, optimization of chemical reactions and combustion processes, bonding energy and atomic collision, representations of DNA three-dimensional structures and microbiological reactions, meteorological and weather prediction, fluid flow in turbo machinery and aerodynamics in vehicles, design of engineering devices involving fluid flow and heat transfer phenomena, etc. [1]

In this research, numerical simulation is applied to study *the steady mixed convective laminar flow over a three-dimensional backward facing step* as shown in Figure 1.1.

This computational problem has become of importance through the years due to its complexity and it has become a traditional benchmark problem for testing and validating numerical codes. Even though the two-dimensional problem has been heavily studied, the three-dimensional case is a relatively new field that in the last decade has started to

be explored thanks to the development of sophisticated computational techniques and the use of powerful computers. However, the scientific community has excluded the effects of the buoyancy forces within the computational domain although it has been shown in several researches that even low buoyancy forces can drastically modify the fluid flow and heat transfer phenomena. One of the reasons why some investigations prefer to neglect the buoyant effects is associated with the requirements for using high computational resources to handle the coupled momentum and energy equations as will be discussed later. Hence the relevance of this research for providing a background for this interesting phenomenon that is present in several devices, and providing a numerical strategy for an appropriate use of the computational resources.

It can be appreciated in Figure 1.1 that the channel's geometrical dimensions are fixed in relation to the step height ( $s=0.01\text{m}$ ) such that the aspect ratio ( $AR=W/s$ ) and the expansion ratio ( $ER=2H/(2H-s)$ ) are equal to 4 and 2, respectively.

The channel total length in the stream-wise direction is 52 times the step height ( $L=52s$ ) while the longitude, upstream of the step, is 2 times the step height ( $l=2s$ ).

Even though, the geometry in question seems to be very simple, the flow through the channel is characterized for dramatically changing its inlet hydrodynamic features downstream of the step, as well as presenting complex three-dimensional flow structures. A schematic diagram for a force convective flow over the backward-facing step is presented in Figure 1.2. In order to give a comprehensive idea of the separation-reattachment phenomenon, a constant z-plane is represented in this figure.

- Step height ( $s$ )
- Aspect ratio ( $AR=W/s=4$ )
- Expansion ratio ( $ER=2H(2H-s)=2$ )
- Total length ( $L=52s$ )
- Step length ( $l=2s$ )

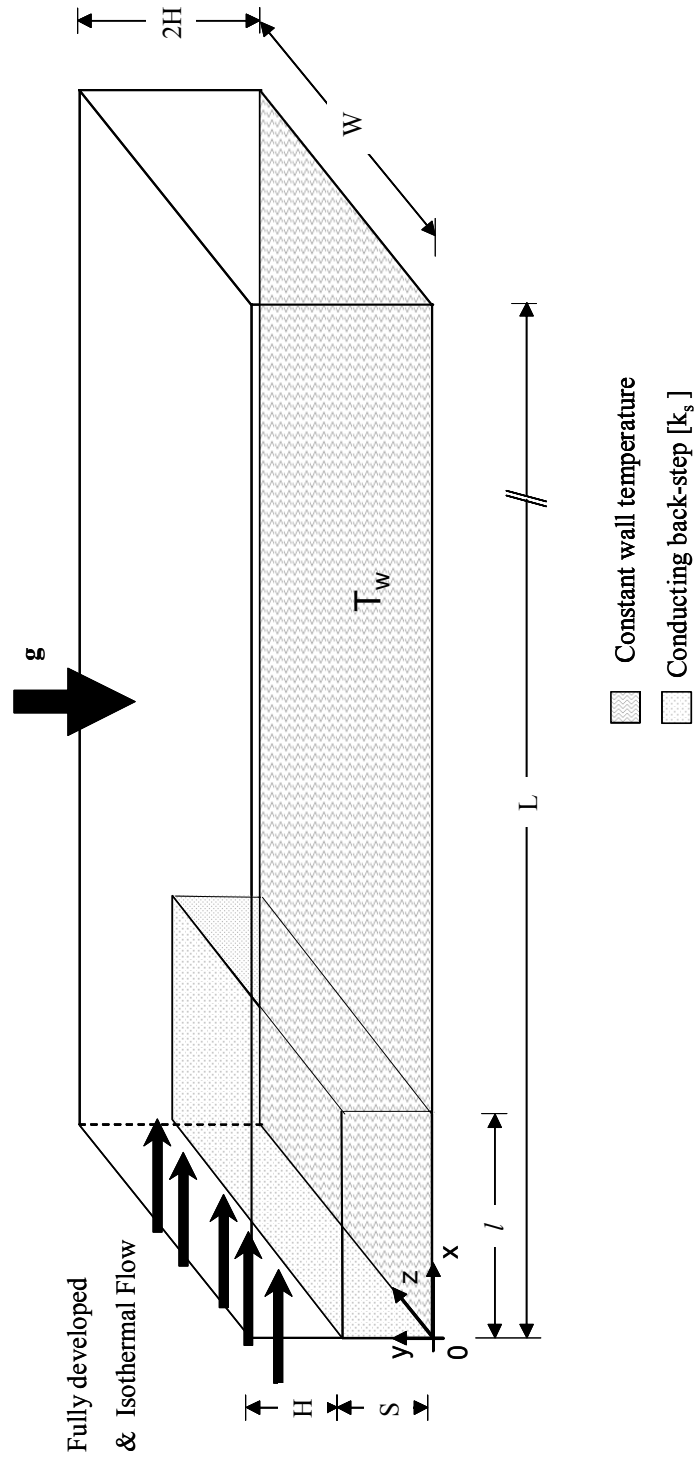


Fig. 1.1 Three-dimensional backward-facing step

Figure 1.2 shows how the boundary layer formed at the duct entrance is disturbed by the sharp turn at the step and the flow is separated. The flow structures build up a dividing stream-line, which separates the reversal flow from the downstream flowing fluid flow. Above this line, a shear layer is formed and reattached downstream of the flow at a point named the reattachment point. Following the reattachment point, a boundary layer gradually re-develops towards the channel exit.

Behind and adjacent to the step, a flow re-circulation zone is present and its limits are the dividing stream-line and the reattachment point. This zone is known as the primary re-circulation zone. Under some conditions, a region of re-circulation flow is attached to the top of the channel [3].

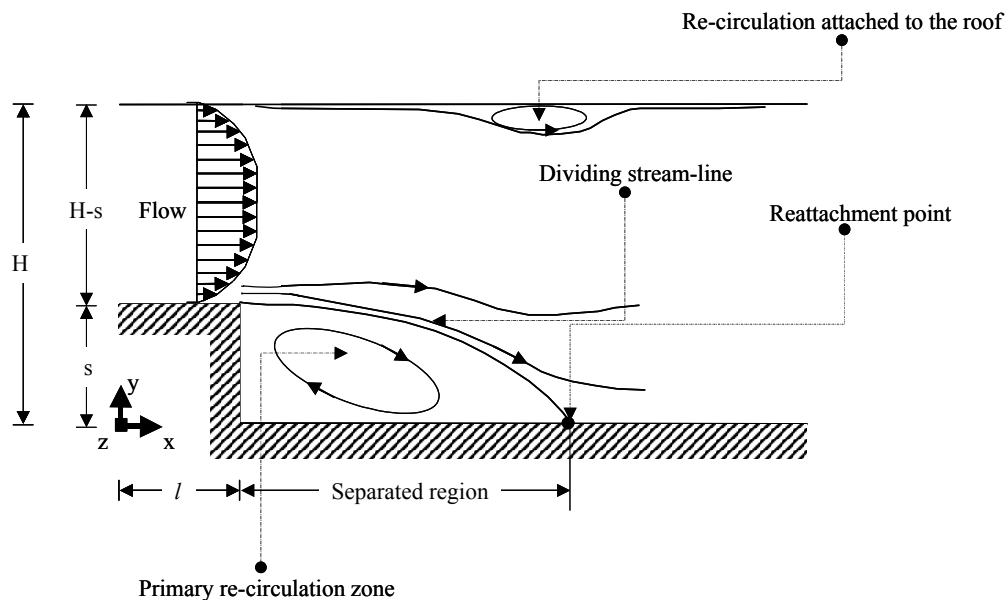


Fig. 1.2 Flow over a backward facing step

Therefore, it can be said that the flow through the channel is characterized as having a shear layer separation, a region of re-circulation flow just behind the step, and under some conditions a region of re-circulation flow (separation-reattachment) is attached to the top of the channel [4].

The importance for studying this kind of phenomena relies on the fact that separated and reattached flows occur in many heat transfer-exchanging devices, such as electronic cooling equipment, cooling of nuclear reactors, cooling of turbine blades, flow in combustion chambers and chemical process equipment, flow in channels whose area is suddenly augmented, like wide-angle diffusers or valves, sediment transport and bed formers in rivers, etc. In other cases, the separation is induced to modify the flow field and to enhance heat transfer conditions as in compact heat exchangers or it can be induced in order to establish more favorable mixing conditions as combustion on a flame holder [3-7].

As mentioned previously, the reattached and separated flow phenomenon is present in a vast variety of industrial devices. However, a complete characterization and full understanding of its behavior is not complete although an enormous quantity of experimental and numerical studies have been conducted in the past decade. The reason is that the complicated three-dimensional flow structures associated with the flow, as well as the great mixing of high and low energy flows occurring in the separation and reattachment regions, significantly impact the fluid flow and heat transfer performance of these devices.

The flow over a backward-facing step presents a simple geometry, but also has the



most important flow structures present in separated and reattached flows. Hence, the flow over a backward-facing step has become the target to obtain basic information, not only experimentally but also numerically, in order to classify the separated and reattached flow. A second consequence is the fact that the fluid flow and heat transfer problem over a backward-facing step has become a computational benchmark problem for testing and validating numerical procedures and numerical codes.

In this research, *numerical simulation of laminar mixed convective flow*, adjacent to a three-dimensional horizontal backward-facing step, is carried out for air ( $Pr=0.70$ ). The flow Reynolds number is fixed at a value of  $Re=200$  and the effects of buoyancy forces on the velocity field and temperature distribution are considered by varying the Richardson number ( $Ri$ ) from 0 to 3.

A *thermally conducting backward-facing step* is also considered for the domain discretization and its impact on the mixed convective flow is analyzed. The finite volume technique is used to discretize the momentum and energy equations and the Semi-Implicit Method for Pressure-Linked Equations (SIMPLE) algorithm was used to link the velocity and the pressure fields. In order to reduce the computational effort and to accelerate convergence, a certain level of computer parallelism applying OpenMP is done in order to speed up the numerical solutions.

## **1.2 Motivation**

The separation and reattachment phenomena occur in several industrial devices and important efforts have been done in the past decade to understand the hydrodynamics

and thermal aspects of these coupled phenomena. However, an in-depth study of these problems is not complete and there is much work left to be done in this area. Furthermore, the mixed convective problem has not been included in the thermal analysis through the years not only because of its complexity, but also for the high computational and experimental resources required for studying the problem. Basically, no information exists for the mixed convective flow over a three-dimensional horizontal backward-facing step.

The global incentive for this research is to develop a numerical study for the mixed convective flow over a *three-dimensional horizontal backward-facing step* in order to present the pertinent results and then to collaborate with accurate information dealing with the effects and the impact of buoyancy forces acting on the velocity field and temperature distribution for flow through this particular geometry. Similarly, is the fact for exploring the applicability and performance of an OpenMP parallel implementation to speed up the computing time in order to get better use of the computational resources.

### **1.3 Objectives**

The objectives of this research are:

- i. To develop a finite volume numerical code to predict the velocity, pressure, and temperature field distributions for laminar mixed convective flow over a three-dimensional horizontal backward-facing step.
- ii. To study the effects of the buoyancy forces acting on the velocity field and temperature distributions from pure force convective flow ( $Ri=0$ ) to

dominant free convective flow ( $Ri=3$ ) for air ( $Pr=0.70$ ).

- iii. To study the impact of a thermally conducting backward-facing step on the mixed convective flow.
- iv. To implement an OpenMP parallel strategy to speed up the numerical solution and make better use of the computational resources.

#### **1.4 Dissertation Outline**

This dissertation expresses the ideas generated after numerically researching the mixed convective flow over a three-dimensional horizontal backward-facing step.

In Chapter I the basic concepts, importance, actual objectives, and motivations for this research are stated, as well a concise preamble to the engineering-scientific problem to be analyzed was presented.

In Chapter II existing literature related to the fluid flow and heat transfer problem in this particular geometry; including numerical and experimental reports for two- and three-dimensional geometries as well as the forced and mixed convective flow in horizontal, inclined, and vertical ducts, are reviewed and the most relevant aspects are highlighted.

Chapter III is dedicated to emphasizing the theoretical and mathematical aspects governing the mixed convective phenomenon. The finite volume numerical implementation technique for solving the three-dimensional mixed convective flow over a horizontal backward-facing step is described in Chapter IV. This includes the description of the Semi-Implicit Method for Pressure Linked Equations (SIMPLE)

algorithm, as well as the line-by-line Tri-Diagonal Matrix Algorithm (line-by-line TDMA) for solving the linear system of equations after the domain discretization.

The next chapter is designed to present results of the validation for the numerical code. Chapter V is also dedicated to showing the grid independence study for the present code.

Chapter VI is planned to describe the parallel strategy by means of an OpenMP parallel implementation. In this chapter a basic introduction to the parallel-computer's architecture is given as well as the benefits of parallel computing and the preamble for the OpenMP parallel programming model. This chapter concludes with the description of the parallel implementation and the performance results obtained.

Chapter VII is intended to present and discuss the results obtained after the numerical simulation of the mixed convective flow over a horizontal backward-facing step. The results include the test cases for Reynolds number  $Re=200$  and Richardson number  $Ri=0, 1, 2,$  and  $3$  utilizing air as working substances. Results for impact of the backward-facing step thermal conductivity to fluid thermal conductivity ratio  $k_s/k_f=0, 10, 100, 1000,$  and, copper/air are also included in this chapter.

Finally, Chapter VIII is designed to present a summary and conclusions of the numerical analyses discussed in previous chapters in addition to the pertinent recommendations and suggestions for further work related to mixed convective flow through this geometry.

## **CHAPTER II**

### **PRIOR WORK**

#### **2.1 Literature Survey**

Studies on separated flow have been conducted extensively in past decades and the backward-facing step geometry has become the central point to obtain a better understanding of the flow separation and reattachment phenomena for both experimental and numerical investigations.

The literature review reports that the first efforts for studying the separation and reattachment flow over a backward-facing step were done in the late 1950's. All of these efforts were conducted experimentally using different flow visualization techniques and deal exclusively with turbulent or transitional regimes and supersonic flows.

One of the first investigations dealing with laminar regime and subsonic flow was presented by Goldstein et al. in 1970 [8]. They concluded, based on their experimental measurements, that in laminar regime the reattachment point is not a constant value as in turbulent regime, but depends on the boundary displacement thickness and the hydraulic Reynolds number.

Interest in studying the reattachment phenomena over the backward-facing step continued in the 1970's and in the 1980's with the development of more sophisticated visualization techniques, the engineering community produced a large quantity of publications referring to experimental results obtained for laminar flow regime. A common simplification of the problem in experimental research is the assumption of

considering the fluid flow over the backward-facing step as two-dimensional when dealing with high aspect ratio ducts ( $AR > 16$ ) and the reattachment point is monitored at the central plane of the channel in the span-wise direction. For small duct aspect ratio the span-wise component of the velocity and the sidewalls have an important influence in the flow behavior then this assumption is not valid [6].

Armaly and coworkers [9] reported Laser-Doppler measurements of velocity distributions and reattachment points for laminar flow in ducts with an aspect ratio of  $AR=36$  and Reynolds number range between 70 and 8000. In this study some numerical predictions are also presented and compared with experimental results. The comparison showed a close agreement for Reynolds number  $Re \leq 400$ , far from this point the measurements and numerical predictions start to deviate from each other. The authors justified this deviation by the inherent three dimensionality of the flow present for  $Re > 400$  in the separation region. They showed that for the two-dimensional laminar regime the reattachment point or reattachment length moves downstream of the step as the Reynolds number increases, and also the development of a secondary re-circulation zone attached to the wall opposite the stepped wall (upper wall), for large Reynolds number ( $Re \geq 400$ ).

The studies on flow over the backward-facing step were not only focused on the fluid flow problem but also on the heat transfer phenomena. Aung, in 1983, established himself as one of the first in reported experimental results on heat transfer for laminar air flow passing a backward-facing step channel heating at uniform temperature from below [10]. In his experimental study, Aung established that for laminar flow the heat transfer

increases monotonically in the stream-wise direction and quantitatively it is less than that of the flat plate value. Also, he established that the maximum heat transfer occurs downstream of the reattachment point.

Sparrow and Chuck performed the first numerical work dealing with heat transfer and fluid flow over a backward-facing step as is cited in their own publication [11]. They implemented a numerical finite difference for studying the airflow phenomenon over a two-dimensional channel heated at constant temperature for the bottom wall from the foot of the step to the end of the channel. They found that the local Nusselt number distribution begins with a low value at the step, and then increases monotonically and attains a maximum value at a position near the reattachment point. Beyond the maximum, the local Nusselt number decreases monotonically towards the fully developed value. This behavior reflects the separation, reattachment, and redevelopment experienced by the flow.

The information and data generated by studying the two-dimensional backward-facing step through the years is quite substantial. In spite of the vast quantity of information, there was no solid base for comparing the results to define an accurate methodology for solving the problem because each author dealt with different geometries, parameters, and conditions. An effort to unify criteria was done by the ASME K-12 Aerospace Heat Transfer Committee, which organized a forum at the Winter Annual Meeting of the American Society of Mechanical Engineers in 1992 [12]. The purpose was to define the two-dimensional backward-facing step as a benchmark problem for verifying the accuracy and validity of numerical software dealing with the

laminar fluid flow and heat transfer problem. A total of 12 papers were presented and different numerical approximations were implemented for solving the problem for an expansion ratio  $ER=2$  and Reynolds number equal to  $Re=800$ . A constant heat flux was imposed along the top wall while the bottom wall of the channel was heated from the step to the channel exit. The total length of the channel was 60 times the elevation of the step.

In summary, four generalized conclusions from the papers presented in the forum deserve special attention. The first one is the confirmation of the primary re-circulation zone just downstream of the backward-facing step as well as the increase in its length with increase in the Reynolds number. The second aspect refers to the presence of a secondary re-circulation zone attached to the flat plate (upper wall of the channel) for Reynolds numbers greater than 400. According to the results the separation point on the upper wall almost coincides with the reattachment length on the bottom wall.

The next point is associated with the heat transfer phenomenon and establishes that at the channel exit the Nusselt number distributions for both the top and bottom walls approaches its laminar fully developed value. However, they have an opposite behavior through the channel. For the stepped wall, the Nusselt number distribution starts with a low value and increases as the reattachment point approaches, achieving its maximum in the vicinity of this point and, then decreasing asymptotically to the fully developed value at the channel exit. For the upper wall, the Nusselt distribution starts with a high value and rapidly decreases to a minimum at the vicinity of the top channel separation point. Downstream of this point the Nusselt number asymptotically increases to reach its fully



developed value at the channel exit. On both walls the growth and behavior of the hydraulic boundary layer impacts the performance of the local heat transfer coefficient.

Finally, the most significant conclusion, arrived from this forum, which has an important relevance to this research, is the fact that the flow over the backward-facing step channel has a strong three-dimensional behavior and the inclusion of this approximation should help to provide several aspects of the separation-reattached region and also a better understanding of this phenomenon. It is important to note here that none of the papers presented at the annual meeting considered the buoyancy effects on flow and heat transfer. These effects become significantly important in the laminar flow regime where the velocity is low and the temperature difference is relatively high.

The three dimensionality of flow over the backward-facing step has been numerically and experimentally explored intensively in the last decade.

Shih and Ho in 1994 [13], published their Laser-Doppler Anemometer measurements for water flowing over a backward-facing step with an aspect ratio  $AR=3$ . The measurements of the three velocity components, inside the primary re-circulation zone, showed that the local span-wise velocity component and the local transverse velocity component are of the same order of magnitude of the local stream-wise velocity component. They also concluded that for a three-dimensional case there are a series of points along the span-wise direction where the stream-wise velocity component, adjacent to the stepped wall, is equal to zero (reattachment points/reattachment line). However, these points do not present a constant value as can be suggested by the two-dimensional case, but they present variations in distance from the step along the span-wise direction.

The shortest value occurs along the central plane of the duct and the farthest value occurs very close to the sidewalls, having values at least 20 percent larger than the values along the central plane.

In 1993 Steinthorsson and collaborators [14] presented a three-dimensional numerical study of steady laminar airflow over a backward-facing step and  $Re=389$ . Their numerical solution of the governing equations was obtained using a modified version of the TRAF3D-CODE. As declared by the authors, the purpose of their research was to study the fluid flow near the sidewalls and its influence on flow development. They used a duct aspect ratio  $AR=36$  and found that the reattachment line is constant over most of the span-wise direction but start decreasing approximately five steps away from the side walls and then increase rapidly to reach a maximum at the side wall. This behavior was attributed to an essentially two-dimensional flow behavior at the central portion of the channel that is dramatically changed to three-dimensional near the walls due to the corresponding boundary layer growth and the inability for the flow to withstand adverse pressure gradients near the side walls.

Similarly, Jiang et al. in 1993 [15] implemented a least-square finite element method based on a first order velocity-pressure-vorticity formulation to predict the fluid flow over a backward-facing step for Reynolds  $100 \leq Re \leq 800$ .

The three dimensionality of the flow was depicted by the variations in the reattachment line in the span-wise direction. This behavior is similar to the one described by Steinthorsson and co-workers [14], but the justification here is associated to the interaction of the primary re-circulation and the presence of a vortex between the

sidewall and the floor.

Attachment of a re-circulation zone to the channel's roof was also reported in this work. The results showed that as the Reynolds number increases this zone propagates from the side walls toward the channel's central plane and its length, in the stream-wise direction, increases at the sidewalls compared to the central zone.

Williams and Baker in 1997 [16], numerically solved the fluid flow problem over a three-dimensional backward-facing step ( $0 < Re < 800$ ), and implemented a modified Euler integration technique to track particles in the computational domain. The results for the reattachment length were quite close to the results described previously, but the particle tracking revealed that the interaction of an impinged wall jet, located at the step plane and the primary re-circulation region, produces spiraling three-dimensional structures in the vicinity of the side walls that spread in size in the stream-wise direction and also propagates toward the channel span-wise central plane.

The three dimensionality of the flow downstream of the backward-facing step has been probed for even large aspect ratio ducts. Measurements for three-dimensional flow over smaller duct aspect ratios were reported by Armaly and collaborators [17]. They used a Laser-Doppler velocimeter for measuring the airflow velocity distributions for a duct aspect ratio (AR) and expansion ratio (ER) equal to 8 and 2.02, respectively and in the Reynolds number range of  $98.7 < Re < 525$ . They found that the fluid flow structures behind the backward-facing step presented strong three-dimensional characteristics due to the small aspect ratio and also confirmed the span-wise variations in the reattachment line ( $x_{u-line}$ ). Their measurements corroborated the theory of the presence of an

impingement jet-like structure adjacent to the sidewalls, previously predicted by Williams and Baker as mentioned before. The existence of this jet-like structure was determined by the presence of peaks values for the stream-wise velocity component along the span-wise direction. The high momentum in this specified zone should be responsible for the minimum existing in the reattachment line. They also concluded that the size of the recirculation zone adjacent to the backward-facing step increased in size with an increase in the Reynolds number.

A complete study of the three-dimensional topology of the fluid flow over the backward-facing step was presented by Chiang and coworkers [4]. Their objective was to get a deeper and more realistic interpretation of the flow physics behind the backward-facing step by utilizing a rigorous mathematical foundation to find saddle points, nodal points, and other characteristic nodes for separation and reattachment. This study revealed that regardless of the Reynolds number, a re-circulation zone is attached to the channel's ceiling but it is confined only to the sidewalls. The upper re-circulation zone growth in length, width, and depth is dependant on the Reynolds number.

Two- and three-dimensional forced convective flows over backward-facing steps subjected to a constant heat flux were numerically simulated by Carrington and Pepper [18]. They implemented a finite element technique to simulate airflow for Reynolds  $Re=400, 800, \text{ and } 1200$  over a backward-facing step geometry such that the aspect and expansion ratios were fixed as 12 and 2, respectively. A tendency for the three-dimensional approximations for matching more precisely with the experimental data was one of their conclusions. Bulk Nusselt number distributions for the bottom and top walls

were plotted as a function of the stream-wise distance downstream of the step. Inside the primary re-circulation zone, the Nusselt number had a maximum value for the bottom surface while the Nusselt number for the top surface reached a minimum at the same axial position. At the channel exit both distributions achieved their asymptotically fully developed value.

Laminar forced convective flow for this configuration has been extensively studied both numerically and experimentally by Armaly and his research group [5,17,19-20]. In these publications results for a duct aspect ratio equal to 8 and an expansion ratio equal to 2 were considered. The convective heat flow is due to a constant heat flux applied to the bottom wall and for Reynolds number range of  $100 < \text{Re} < 600$ . They found that the complex three-dimensional flow structures developed downstream of the backward-facing step augment their intensity as the Reynolds number increases. The size and shape of the primary re-circulation zone is greatly influenced by the Reynolds number. They noted that the flow structures within the separation shear layer develops a “jet-like” structure adjacent to the side walls and its impact on the stepped wall is responsible for the minimum in the so called  $x_u$ -line, the maximum in the local Nusselt number, as well as the minimum in the wall’s shear stress. In some regions, adjacent to the bottom wall, the three velocity components are of the same order of magnitude and thus, their influence on the wall shear stress and the flow structures. The velocity components also showed that the wall shear stress is equal to zero just in two points (symmetric with respect to the span-wise direction) along the bottom wall and their locations are shifted downstream as the Reynolds number increases. The maximum local Nusselt number always occurs

downstream of the location of minimum shear stress.

Mixed convective flow over a backward-facing step has been the central point for several experimental and numerical researchers in the past several decades. Besides the interest in the study of the mixed convective flow in this geometry, the effects of the duct inclination angle was measured and numerically simulated by several authors.

Lin and co-workers [21] simulated two-dimensional laminar mixed assisting convective flow over a backward-facing step by submitting the stepped wall to a constant temperature. This work focused on the effects of duct inclination angle and its impact in the developing flow through the channel. Their most relevant remark is the fact that an increase in the duct inclination angle implies an increase in the reattachment length. In other words, larger reattachment lengths occur if the forced flow and the buoyant forces are perpendicular to each other rather than if buoyancy is assisting the forced flow. The location where the local Nusselt number reaches its peak value is moved downstream of the step as the duct inclination angle changes from  $0^\circ$  to an inclined position.

Hong et al. [22] developed a study similar to the above-mentioned research, but here the bottom wall was submitted to a uniform heat flux. In addition a  $360^\circ$  duct rotation and also the effects of varying the Prandtl number were considered. Their results reinforced the theory that if the buoyancy is assisting the forced flow ( $0^\circ$ ) the reattachment length has a minimum value, while if the buoyancy is opposing the forced flow ( $180^\circ$ ), then the reattachment length has a maximum value. Here a duct inclination of  $90^\circ$  refers to the case where the buoyant forces and the forced flow are perpendicular

to each other. According to their results and their geometry, the increase in the duct inclination angle from  $0^\circ$ - $180^\circ$  produces farther reattachment points from the backward-facing step, as well as farther locations from the backward-facing step for the peak Nusselt number. The opposite behavior was found when the duct rotated from  $180^\circ$  to  $360^\circ$ . They also noted that increasing the Prandtl number moved the reattachment point farther downstream and, increased the Nusselt number but decreased the friction coefficient. The justification to this behavior is that fluids with a lower Prandtl number are more sensitive to changes in the buoyancy effects and will reach the fully developed condition at closer downstream location.

Laminar mixed convection over a two-dimensional horizontal backward-facing step with heating from below at a constant temperature, was measured by Abu-Mulaweh et al. [23]. Measurements using a Laser-Doppler velocimeter and cold wire anemometer for velocity and temperature distributions revealed that the effect of buoyancy forces acting on a horizontal backward-facing step does not drastically modify the behavior of the stream-wise velocity component, but drastically influences the onset of vortex instability. However, this report does not present any information on the interaction of the buoyancy forces and the transverse velocity component. It is evident that this component must be strongly affected as it is parallel to the buoyancy components. Also it is important to mention that in these measurements a small temperature gradient between the wall and the flow stream was considered ( $0 < \Delta T < 30$ ).

Flow visualization experiments to study the vortex instability phenomenon of a horizontal laminar forced convection in the separation region adjacent to a backward-

facing step were conducted by Cheng and Kimura [24]. They heated the bottom wall at a constant temperature such that the temperature gradient ranged from 0 to 30 and the Reynolds parameter varied from 80 to 370. Their results showed that the buoyancy effects have an important impact on the flow structures even at low free stream velocity or low Reynolds numbers regimes. Highly complicated three-dimensional flow patterns existed inside the separation region even for small temperature gradients. Cross sectional views (planes normal to the stream-wise direction) revealed that the onset of longitudinal vortices appears in the vicinity of the backward-facing step and its intensity, shape and, size depends on the downstream distance from the backward-facing step. Similarly, top cross sectional views of the channel flow showed the formation of a pair of counter-rotary vortex rolls along the channel. However, the axes of the vortex rolls are not parallel to the stream-wise axis. They also noted that high temperature gradients produce more intense vortex rolls while high Reynolds numbers restrain the formation of such vortices inside the primary re-circulation zone.

Mixed convection on a two-dimensional vertical backward-facing step subjected to a constant wall temperature was numerically studied by Lin et al. [25]. They presented results for a duct expansion ratio equal to 2 and a Reynolds number of 50. The temperature gradients ( $\Delta T$ ) responsible for the buoyancy effects was varied from 0 to 75. The results showed that the locations for the peak Nusselt number and the reattachment point moved upstream as the value of the buoyancy parameter increased. Furthermore, for  $Re=50$  and  $\Delta T > 50$  there was no reattachment to the step wall.

Several authors studied mixed convective flow over a vertical backward-facing step



and it was the central point for the HTD ASME Winter Annual Meeting of 1993 [26]. The benchmark problem was to solve the steady state two-dimensional mixed convective flow in a vertical backward-facing step submitting the stepped wall to a high constant temperature while the opposite wall (plane wall) was uniformly kept at the same temperature of the fluid at the channel inlet and the backward-facing step was considered as adiabatic. A total of 11 papers were presented to solve the problem using different numerical approaches. The general remarks are that the primary re-circulation zone is considerably reduced when buoyancy forces were taken into account and the formation of a secondary re-circulation zone adjacent to the corner of the step and the heated wall. For mixed convection, the flow accelerates near the heated wall, increasing the wall friction coefficient and pulling the velocity profile toward this wall. As a result, pronounced asymmetric velocity profiles existed at the channel exit thus precluding the attainment of a fully developed condition.

The effects of buoyancy forces on mixed convective flow over a three-dimensional backward-facing step is a topic that is not commonly found in literature. In this area Armali, Nie and collaborators have made the most representative effort to study this phenomenon; however their interest has been focused on vertical ducts where the buoyancy force, the gravity, and the main flow stream are parallel [27-29]. In these publications numerical simulation utilizing the commercial CFD code FLUENT 5.0 for assisted buoyancy flow through a duct with an aspect ratio equal to 8 and an expansion ratio equal to 2, was presented. They imposed the hydrodynamic inlet condition for airflow such that the Reynolds number was fixed to 200 and the Grashof number ( $Gr$ )

was varied from 0 to 4000. The buoyancy forces were due to a constant heating flux applied to the stepped wall. The results showed that as the Grashof number increases, the size of the primary re-circulation zone decreases. The reverse tendency was observed for the secondary re-circulation zone adjacent to the bottom corner of the step. This behavior continues until the buoyancy forces are strong enough to lift the primary re-circulation zone away from the heated wall (stepped wall) and connected it with the mainstream flow. At this point the primary re-circulation zone is detached from the heated wall but remains attached to the backward-facing step. The locations where the local Nusselt number reaches its maximum value and the location where the friction coefficient reaches its minimum value shifted upstream toward the backward-facing step and closer to the wall as the Grashof number was increased. The ratio between the buoyancy forces and the inertial forces considered in these studies was no larger than 0.1 ( $0 < Gr/Re^2 < 0.1$ ).

A finite difference implementation to numerically simulate the three-dimensional mixed convective flow over a backward-facing step, including a study of the duct inclination angle, was carried out by Iwai et al. [30-31]. They applied a line-by-line method combined with the ADI scheme to solve the system of algebraic equations after the domain discretization. A fifth order upwind scheme and a fourth order central difference scheme were adopted to discretize the convection and diffusion terms of the governing equations. The SIMPLE algorithm was used to compute pressure corrections at each iteration. The duct aspect ratio (AR) and expansion ratio (ER) were 16 and 2, respectively. The heated wall downstream of the step was maintained at a uniform

constant heat flux, while any other wall was considered thermally adiabatic. The simulation was carried out for air ( $Pr=0.71$ ) at  $Re=125$ . The Boussinesq approximation was applied to account for the buoyancy term. The comments and conclusions achieved by these two works coincide with others, explained earlier, for the case of a vertical backward-facing step where the buoyancy forces and the mainstream flow are parallel. However, the conclusion achieved for the case where the buoyancy forces and the main flow are perpendicular (horizontal backward-facing step) is that the level of buoyancy forces imposed was not large enough to considerably modify the velocity distribution ( $Ri^*=0.03$ ). As a consequence, the impact of the buoyancy forces on flow over a horizontal backward-facing step cannot be inferred by Iwai and coworkers. Furthermore they judged their flow to be in a pure forced convective regime.

A general review of the recent literature on laminar mixed convective flow over a backward-facing step including two- and three-dimensional studies, vertical, horizontal, and inclined ducts orientation was reported by Abu-Mulaweh in 2003 [32]. According to this publication several numerical and experimental studies have been conducted to analyze the effects of the buoyancy forces on the velocity field and on the physical parameters defining the flow over the backward-facing step. However, a very limited number of studies have been conducted to analyze the three-dimensional mixed convective flow over a backward-facing step, and even fewer studies have been conducted to analyze the horizontal case where the buoyancy forces and the mainstream flow are perpendicular to each other. In this publication just four studies dealing with the horizontal case are reported and just one of them includes the three dimensionality of the

flow. All of these studies have been previously reviewed in this chapter.

A global review indicates that even though a large quantity of publications dedicated to study the fluid flow and heat transfer phenomena over a backward-facing step, this problem is not completely understood due to its complexity and the strong three-dimensional flow behavior. It is also important to remark here that the literature review has shown that indeed numerous publications have been dedicated to the study of heat transfer and fluid flow over a backward-facing step. However, a horizontal backward-facing step analysis of mixed convection has received limited attention.

Therefore, this investigation is conducted in the way to contribute accurate numerical data for the characterization and study of laminar mixed convective flow over a three-dimensional horizontal backward-facing step. As the literature review showed this problem has not been extensively studied and the information obtained in this dissertation could be taken as a starting point for a new researching field in the future.

## CHAPTER III

### MATHEMATICAL MODEL

#### 3.1 Introduction

The term convection is usually referred to as the transport of energy and mass by potential gradients and fluid motion [33]. In this study, the effects of mass transport (mass dissipation, chemical reaction, change of phase, transpiration, etc.) are neglected and the transport of energy by temperature differences or convective heat transfer (*heat convection*) is solely of relevant importance.

Engineering applications of convective heat transfer are extremely varied and occur in the presence of temperature gradients between a fluid in motion and a bounding solid surface. The essential feature of a convective heat transfer process is the transport of energy by molecular motion (*diffusion*) and by the bulk macroscopic motion of the fluid (*advection*) [34].

The convective heat transfer phenomenon is closely related to fluid motion, in this sense the necessity for describing how the velocity field impacts the temperature distributions is the main point for analyzing some heat convection problems. However, in some other cases the buoyancy forces in addition to the temperature distribution are the ones that play the dominant role in the heat convective phenomenon, setting up the fluid motion and impacting the velocity field. If an external agent as a pump, impeller, fan, blower, etc. induces the fluid motion involved in the heat convective process, then the process is referred to as forced convection. But, if the driving mechanism for the

fluid motion is due to the presence of buoyancy and body forces, acting due to density variations induced by temperature gradients, the phenomenon is called free convection (*natural convection*) or buoyancy induced flow [35,36]. Thus the transport of thermal energy in a heat convective process is featured and classified according to the main driving mechanisms for the fluid motion.

A special convective transport phenomena presented in several engineering applications such as, the design of compact heat exchangers, flat plate solar collectors, cooling of electronic components and circuitry, meteorology phenomena, etc., [37] is the *mixed convection* that is the result of the influence of body forces and buoyancy effects on the forced convection phenomenon. The major effect of buoyancy forces is to modify the velocity and temperature distributions as well as some other physical parameters from their values for the pure forced convective flow. Therefore, heat transfer by mixed convection has features and properties that are completely different from its values for pure forced convective flow or for pure free convective flow.

As can be suggested, the mixed convection will be present in processes when both the forced convection and buoyancy effects are of significant importance for the phenomenon and is exclusively of laminar and transitional flow regimens and moderate to large temperature gradients [33].

The mathematical equations governing the mixed convective flow are presented in the following section.

### 3.2 Basic Equations

This study deals exclusively with laminar flow and only takes into consideration Newtonian fluids, which behaves as a continuum.

The following assumptions are imposed for the mathematical model;

- i. Steady state
- ii. Incompressible flow
- iii. Body forces acting only in the direction normal to the main flow
- iv. Viscous dissipation term neglected
- v. Constant properties
- vi. No internal heat generation

Based on these assumptions, the momentum and energy equations governing the fluid motion and the energy transport expressed in the Cartesian tensor notation are reduced to the following expressions [38,39].

Mass conservation equation:

$$\frac{\partial}{\partial x_i}(\rho u_i) = 0 \quad (3.1)$$

Momentum equation:

$$\frac{\partial}{\partial x_j}(u_i u_j) = -\frac{\partial p}{\partial x_i} + \frac{\partial}{\partial x_j} \tau_{ij} + \rho g_i \quad (3.2)$$

and

$$\tau_{ij} = \mu \left( \frac{\partial u_i}{\partial x_j} + \frac{\partial u_j}{\partial x_i} - \frac{2}{3} \delta_{ij} \frac{\partial u_l}{\partial x_l} \right) \quad (3.3)$$

Energy equation

$$\frac{\partial}{\partial x_j}(\rho C_p u_j T) = \frac{\partial}{\partial x_j} \left( k \frac{\partial T}{\partial x_j} \right) \quad (3.4)$$

Here the coordinate direction is referred as  $x_i$  ( $x_i = x, y, z$ ), and the velocity component in such direction is represented by  $u_i$  ( $u_i = u, v, w$ ).

Equation (3.2) is also known as the Navier-Stokes momentum equation and besides the mass conservation equation Eq. (3.1) they are the fundamental equations for solving any fluid flow problem. If the fluid motion involves a heat transfer process, then in addition to the above mentioned equations the energy equation, Eq. (3.4) must be considered to solve the fluid flow and heat transfer problem.

Some authors define the mass conservation equation, the Navier-Stokes momentum equation and the energy equation as the basic equations for any convective engineering problem [38]. The unknowns or variables involved in these equations are the velocity and its three components in each coordinate direction  $u, v$ , and  $w$ , the thermodynamic pressure  $p$  and the absolute temperature  $T$ . The  $k$  (thermal conductivity) and the  $\mu$  (dynamic viscosity) are considered as the transport properties for momentum and thermal energy.

Following, the pure forced convective flow as well as some important aspects of the pure free convective flow will be considered and then the governing equations for the mixed convective flow will be detailed.



### 3.2.1 Forced Convection

Considering the channel as shown in Figure 3.1 as a representation of a pure forced convective flow through a rectangular channel with smooth and impermeable walls; heated from below at a constant temperature  $T_1$ . The upper wall is maintained at a constant temperature  $T_2$  and the sidewalls are considered as adiabatic ones.

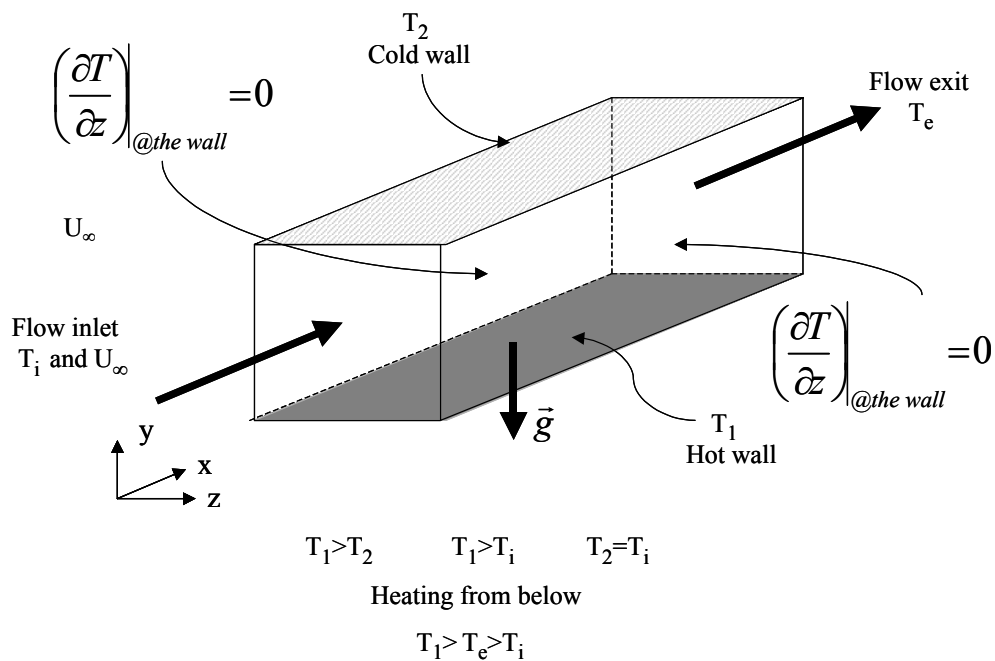


Fig. 3.1 Pure forced convective flow in a horizontal channel

At the channel inlet the flow is considered to be uniform with a velocity  $U_\infty$  and isothermal with a constant temperature  $T_i$ . For a pure forced convective flow, as soon as the fluid enters the channel a velocity boundary layer is developing along the plane

surfaces or walls and in the downstream direction and far from the inlet, the boundary layer will fill the entire duct. Similarly, a thermal boundary layer will be developing along the heated (*or cooled*) walls. Farther downstream of the channel inlet, a constant velocity profile and a constant temperature profile are found and it is in this point that the flow is considered as a hydro-dynamically and thermally fully developed flow. At the channel exit the temperature of the fluid will be higher than at the inlet for a heating process and it will be lower for a cooling process.

The fluid motion and the thermal energy transport for a pure forced convection process are the mass conservation Eq. (3.1), the momentum equation Eq. (3.2), and the energy equation Eq. (3.4). If the effects of the gravitational field in the fluid are neglected, then the term  $(\rho g_i)$  in the right hand side of the Eq. (3.2) is zero.

The engineering applications of pure forced convective flow are mainly concerned with the pressure drop and the drag force within the flow, here is the relevance for including the first term of the right hand side in the momentum equation, Eq. (3.2).

As can be seen from Eq. (3.2), the momentum equation present non-linear quantities on their left hand side (*advection term*) and are coupled not only among them but also with the mass conservation equation, Eq. (3.1), because all of them have the three velocity components. However, the mass conservation equation and the momentum equation are independent of the energy equation, Eq. (3.4), and they can be solved independently of the energy equation.

It is not the same case for the energy equation, Eq. (3.4), because the three velocity components are present on the left hand side of the equation (*advection term*). Then the

temperature distribution and the heat transfer problem cannot be solved unless the three velocity components are previously known.

Based on the above discussion, it can be inferred that the solution of a three dimensional pure forced convective flow is not an easy task and for several applications the numerical approximation is the only way to reach a final solution.

### 3.2.2 Free Convection or Buoyancy Induced Flow

Figure 3.2 shows a quiescent fluid (atmospheric conditions and  $\vec{V} \approx 0$ ) in a rectangular channel heated from below at constant temperature. For simplicity, a constant plane in the z-direction is exemplified. The bottom wall is at a constant temperature ( $T_1$ ) and is higher than the upper wall temperature ( $T_2$ ).

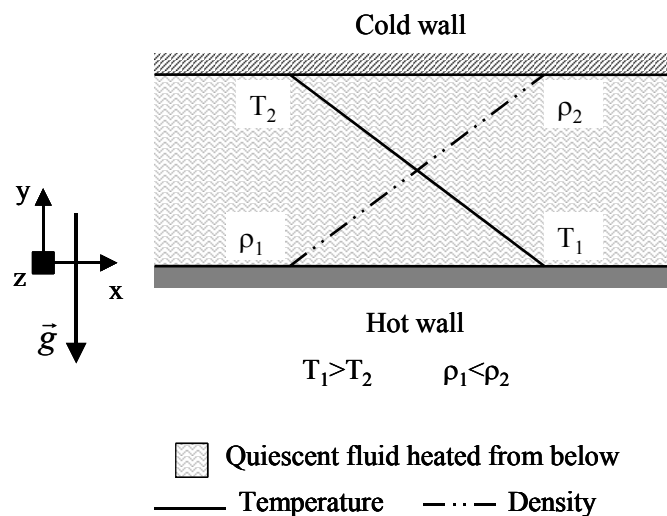


Fig. 3.2 Pure free convective flow for a quiescent fluid

Under this condition a temperature gradient in the vertical direction is established inside the quiescent fluid. The consequence is that a fluid layer with low density and high temperature will be formed at the vicinity of the bottom wall. In the same way, a fluid layer of high density will be produced along the upper wall [40].

If the temperature difference is increased farther than a critical value the viscous forces within the fluid can no longer maintain the buoyancy forces associated with the density variations and the temperature gradients, then a convective motion is set up giving rise to circulation patterns as is suggested in Figure 3.3. In this case the low-density fluid, by the action of the buoyancy forces on the gravity field, tends to float and rise to the top of the channel, while the high-density fluid tends to displace towards the bottom wall. Then the fluid motion is caused by the non-uniformity of the local density ( $\rho_l$ ) along the fluid region. Under these conditions a pure free convective flow or a buoyancy induced flow is set up.

In buoyancy induced flows it is assumed that the pressure gradient term on the Y momentum equation (vertical coordinate direction) is due to the hydrostatic pressure variation and it is considered to be the product of the gravity and the reference density:

$$-\frac{\partial p}{\partial y} = (g_y \rho_\infty) \quad (3.5)$$

If the pressure gradient is combined with the body forces acting on the gravitational field, what is obtained is the buoyancy force  $\vec{B}$ , as it is shown in Eq. (3.6). In this equation, the variations on the density in the fluid motion are mathematically expressed as the product of the difference between the reference density and the local density

$(\rho_\infty - \rho_l)$  and the acceleration due to gravity [36].

$$\vec{B} = \vec{g}_y (\rho_\infty - \rho_l) \quad (3.6)$$

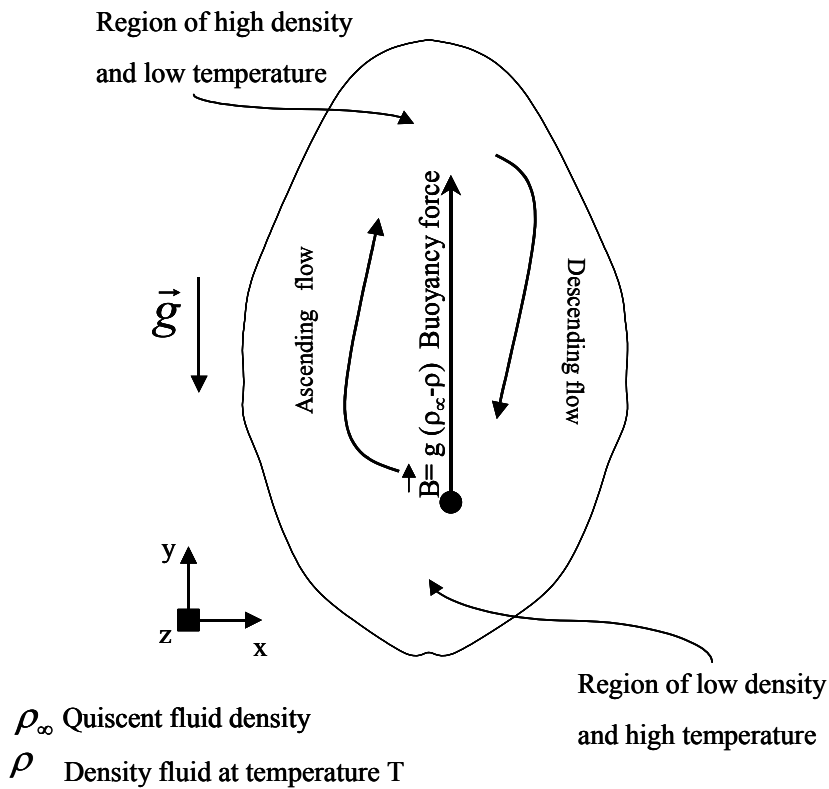


Fig. 3.3 Convective circulation patterns for buoyancy induced flow

According to Eq. (3.6) if the local density  $\rho_l$  is smaller than the reference density  $\rho_\infty$  ( $\rho_\infty > \rho_l$ ) then the buoyancy force  $\vec{B}$  has a positive value which means that the “local fluid element” is moving in the y positive coordinate (*ascending*).

The momentum equation in the y-direction for the pure free convection process must include the buoyancy force. Then, introducing Eq. (3.6) in the momentum equation, Eq. (3.2), then the final expression for the Y-momentum equation in its expanded form for a pure free convective flow is presented in Eq. (3.7).

$$\frac{\partial}{\partial x_j}(u_i u_j) = \frac{\partial}{\partial x_j} \tau_{ij} + (\rho_\infty - \rho_l) g_i \quad (3.7)$$

The other equations governing the fluid motion and the energy transport for the pure free convection are the mass conservation Eq. (3.1), the X- and Z-momentum equations, and the energy equation, Eq. (3.4)

An inevitable fact for solving buoyancy induced flows is that the density and the temperature have a linear relation and then for solving the free convection problem there are five coupled governing equations for the flow variables pressure, temperature, and the three velocity components, in addition to the variable flow density as well as the diffusion properties for flow and heat transfer.

As can be appreciated, the solution of the pure free convection problem is of considerable complexity. However, several theoretical approximations have been developed in order to alleviate the difficulties associated with the solution of pure free convective flow problems. Among them, the Boussinesq approximation has been widely considered in order to simplify the complexity of the equations for the buoyancy-induced flows.

The Boussinesq approximation has its basis in the following two assumptions [33,35,41].

- i. It neglects all variable-property effects in the mass conservation equation, the X- and Z-momentum equations, and the energy equation, and the variations in density are restricted to the vertical Y- momentum equation
- ii. The density variation can be approached with a simplified equation of state as follows:

$$\rho \cong \rho_{\infty} [1 - \beta(T - T_{\infty})] \quad (3.8)$$

Therefore, the density is considered to be an exclusive function of the temperature  $\rho = \rho(T)$ . In Eq. (3.8), the parameter  $\beta$  represents the volumetric thermal expansion coefficient defined as:

$$\beta = -\frac{1}{\rho} \left( \frac{\partial \rho}{\partial T} \right)_p \quad (3.9)$$

The ideal gas equation of state is defined as [42].

$$p = \rho RT \Rightarrow \rho = \frac{p}{RT} \quad (3.10)$$

Introducing Eq. (3.10) in Eq. (3.9) the  $\beta$  coefficient for an ideal gas is reduced to the following expression.

$$\beta = \frac{1}{T} \quad (3.11)$$

Finally, the Y-momentum equation can be reduced to the following equation.

$$\frac{\partial}{\partial x_j} (u_i u_j) = \frac{\partial}{\partial x_j} \tau_{ij} + \rho_{\infty} g_i \beta (T - T_{\infty}) \quad (3.12)$$

The buoyancy forces are represented in the second term of the right hand side of Eq. (3.12). In this term the density variations due to the buoyancy force is accounted via the

volumetric thermal expansion coefficient according to the Boussinesq approximation.

The validity of the Boussinesq approximation is limited to low and moderate temperature gradients and is applicable only if  $\beta(T - T_\infty) \ll 1$  [35]. Far from this limit the simplifications of the Boussinesq approximations give erroneous velocity and temperature distributions.

Once the equation for pure forced convection and pure free convection has been established, the next step is the mathematical derivation for the mixed convection problem.

### 3.2.3 Mixed Convection

As considered before, the mixed convection is a combination of two mechanisms, namely the forced convection and the free convection. Even small buoyancy effects can play an important role and considerably modify the flow characteristics of a pure forced convective flow or vice versa.

The governing equation for mixed convection should consider the effects of the buoyancy forces on the pure forced convective flow. Based on the Boussinesq approximation the buoyancy effects are confined to the Y-momentum equation and the resulting equation is:

$$\frac{\partial}{\partial x_j} (u_i u_j) = -\frac{\partial p}{\partial x_i} + \frac{\partial}{\partial x_j} \tau_{ij} + g_i (\rho_\infty - \rho_l) \quad (3.13)$$

For buoyancy induced flows the gradient  $\left( \frac{\partial p}{\partial x_i} \right)$  is negligible, but for mixed convective flows the gradient in the pressure could be of considerable magnitude.



According to the second assumption of the Boussinesq approximation, the density variation can be accounted for via the volumetric thermal expansion coefficient  $\beta$ . Finally, under this assumption the Y-momentum equation for mixed convective flow can be expressed as follows:

$$\frac{\partial}{\partial x_j} (u_i u_j) = -\frac{\partial p}{\partial x_i} + \frac{\partial}{\partial x_j} \tau_{ij} + \rho_\infty g_i \beta (T - T_\infty) \quad (3.14)$$

The mass conservation equation, the momentum equations in X- and Z- directions as well as the energy equation remain in the same form as presented in Eqs. (3.1), (3.2), and (3.4).

In order to determine the importance or contribution of each mechanism in the mixed convection process a dimensionless parameter, that is the ratio of buoyancy forces to inertial forces, has been defined as follows [41]:

$$Ri = \frac{Gr}{Re^2} = \frac{\frac{g\beta L^3 \Delta T}{\nu^2}}{\left(\frac{VD_h}{\nu}\right)^2} \quad (3.15)$$

If  $Ri$  (*Richardson number*) has a magnitude order of unity, then both free convection and forced convection are equally important for the process. On the other hand, if  $Ri$  is small then the forced convection is the predominant effect in the mixed convection, whereas for large  $Ri$  values the free convection is the principal and dominant effect in the mixed convective process.

## CHAPTER IV

### NUMERICAL PROCEDURE

#### 4.1 Introduction

In general the mathematical formulation of a physical problem involves a set of partial or differential equations that need to be solved in order to find an answer to the problem in question. However, the solution of these equations could be very complex, as in the case of a mixed convective flow described in Chapter III. In such cases the only way for finding an appropriate solution is via a numerical approach.

Consequently to solve any problem by a numerical approach the mathematical formulation must be transformed by means of a discretization process to an easy format for the numeric process. This means that the mathematical equations that are valid in the specific space and time or computational domain should be simplified to their equivalent forms in terms of an algebraic linear system of equations and then solved by approximations at definite points (*discrete points*) inside the computational domain. The greater the number of discrete points are added to the discretization of the domain, the numerical solution will approach the exact solution of the differential equations. However, to indiscriminately augment the number of discrete points would increase the round-off error.

Among the most frequent discretizing techniques used for fluid flow and heat transfer problems are the finite difference (FD), the finite element (FE), *the finite volume* (FV), and the spectral methods (SM).

The finite volume technique (FV) presents considerable advantages due to its simplicity and easy numerical implementation as well as its applicability for dealing with complex geometries. But the most significant characteristic is that the FV technique is conservative by construction; which means that for each finite size cell (control volume) inside the domain the resulting discretized approximations for each property express an exact balance between the control volume and its neighbors [43]. In this research, the numerical discretization technique applied for solving the Navier-Stokes and the energy equations is the finite volume (FV).

#### 4.2 The General Transport Equation

The conservation laws governing the fluid flow and heat transfer expressed in terms of differential equations imply that there must exist a balance between a dependent variable ( $\phi$ ) and all the different factors that have an influence on this variable. The statement before is expressed mathematically by the steady state transport equation for the variable  $\phi$  [44].

$$\frac{\partial}{\partial x_i}(\rho\phi u_i) = \frac{\partial}{\partial x_i} \left( \Gamma_\phi \frac{\partial}{\partial x_i} \phi \right) + S_\phi \quad (4.1)$$

The convective (*advection*) term is on the left hand side, while the diffusive term and the source term are the first and second terms on the right hand side, respectively. The quantities  $\Gamma_\phi$  (*diffusion coefficient*) and  $S_\phi$  (*source term*) have a specific meaning according to the dependent variable and the physical phenomena.

Equation (4.1) can take several forms depending on which is the dependent variable

$\phi$  in question. If  $\phi$  takes the value of 1, u, v, w, or T, then the transport equation can be identified as the mass conservation, the X-momentum equation, the Y-momentum equation, the Z-momentum equation or the energy equation, respectively in Cartesian coordinate system. The values for the variables, the diffusion coefficients and the source terms are summarized in Table 4.1.

Table 4.1 Variables for the general transport equation

Transport variable $\phi$	Index	Diffusion coefficient $\Gamma_\phi$	Source term $S_\phi$	Equation
1	$i, j, k$	0	0	Mass conservation
u	$i$	$\mu$	$\partial_i p$	X-momentum
v	$j$	$\mu$	$\partial_j p + \rho g_j \beta \Delta T$	Y-momentum
w	$k$	$\mu$	$\partial_k p$	Z-momentum
T	$i, j, k$	$\frac{k}{\rho C_p}$	0	Energy

### 4.3 Finite Volume Discretization Technique

The numerical solution using the FV discretization technique for fluid flow, heat transfer, and other related processes starts when the computation domain is divided into

a number of non-overlapping control volumes (*small parallelepipeds*) such that there is one control volume surrounding each grid point (*nodal point*). This process is known as the geometrical discretization of the domain or the grid generation for the domain [43]. Figure 4.1 presents a schematic diagram for an element of fluid flow in the space with longitudinal dimensions  $\Delta x$ ,  $\Delta y$ , and  $\Delta z$ .

In Figure 4.1, the  $P$  is the nodal point and the N, S, W, E, T, and B represent the neighboring nodal points in each coordinate direction; while the n, s, w, e, t, and b represent the face of the control volume at each coordinate direction. The distance between nodal points (diffusion length) is represented by  $\delta x$ ,  $\delta y$ , and  $\delta z$  according to the coordinate direction.

The numerical discretization implies that the transport equation for the variable  $\phi$  would be expressed as an algebraic relation for each control volume inside the domain that involves the values of the physical quantity at the control volume and its neighbors. In the FV technique the procedure is approximated by an integration of the transport equation for each control volume in the computational domain, as shown in the equation below.

$$\int_{CV} \frac{\partial}{\partial x_i} (\rho \phi u_i) dV = \int_{CV} \frac{\partial}{\partial x_i} (\Gamma_\phi \partial_i \phi) dV + \int_{CV} S_\phi dV \quad (4.2)$$

According to the Divergence Theorem of Gauss any volume integral can be transformed into a surface integral over the boundary-limiting surface in the region [45]. Under this assumption Eq. (4.2) can be transformed into a surface integral as expressed in Eq. (4.3).

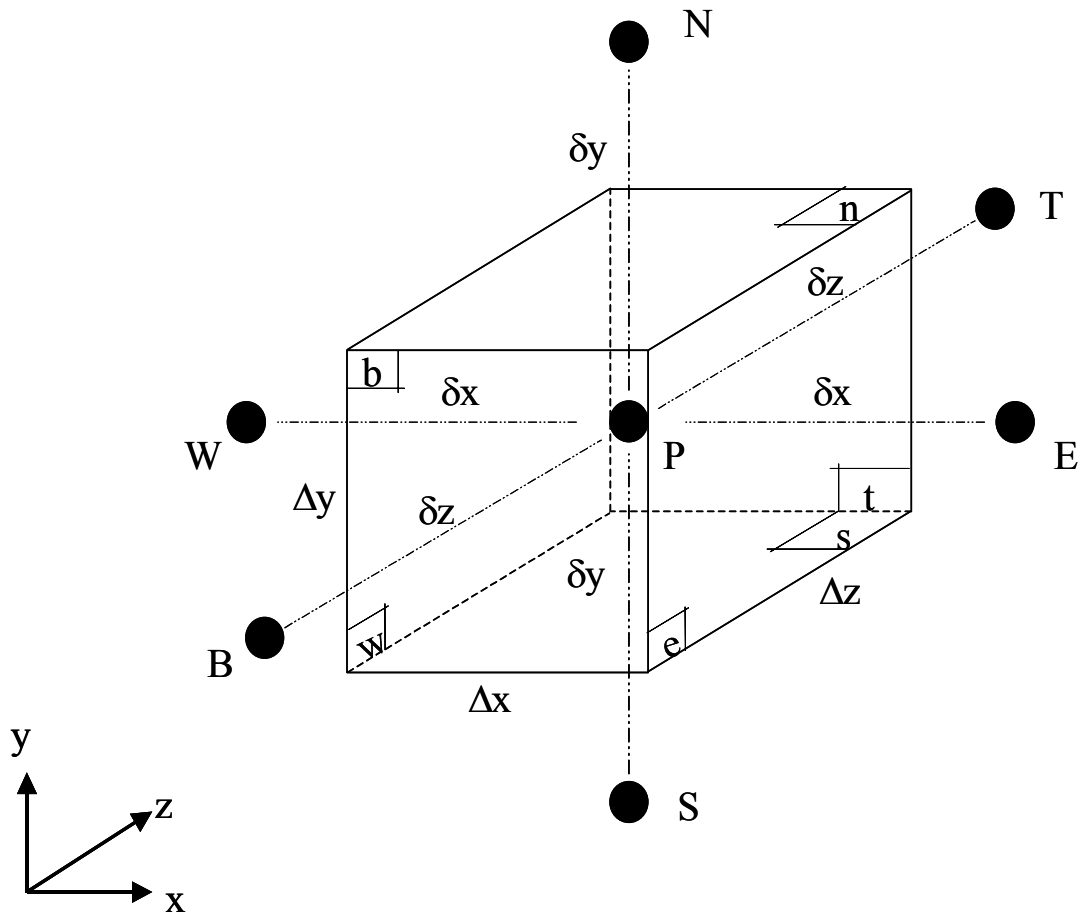


Fig. 4.1 Volume element surrounded by its neighbor grid points

$$\int_A \mathbf{n} \cdot (\rho \phi \bar{\mathbf{u}}) dA = \int_A \mathbf{n} \cdot (\Gamma \text{grad} \phi) dA + \int_{CV} S_\phi dV \quad (4.3)$$

The dot product  $\mathbf{n} \cdot (\rho \phi \bar{\mathbf{u}})$  and  $\mathbf{n} \cdot (\Gamma \text{grad} \phi)$  should be interpreted as the components normal to the element surface  $dA$ .

The first term on the left hand side of Eq. (4.3) is associated with the flux component of the property  $\phi$  due to the fluid flow across the area and along the outward normal vector  $\mathbf{n}$ . It means the net rate of change of the fluid property  $\phi$  in the fluid element is due to convection. The first term on the right hand side of Eq. (4.3) represents the net rate of change of the fluid property  $\phi$  in the fluid element due to diffusion. The second term in the right hand side of Eq. (4.3) is associated with the rate of change of the property  $\phi$  as a result of sources inside the fluid element.

The results of the integration in Eq. (4.3) applied to the control volume in Figure 4.1 would represent the variation of the property  $\phi$  in the control volume due to the interaction with its neighboring nodal points and the convective and diffusive flux across the control volume faces as well as the increase or decrease of the property  $\phi$  due to the source term. The result is expressed in Eq. (4.4).

$$\begin{aligned} & \left[ \rho u \phi - \Gamma_\phi \frac{\partial \phi}{\partial x} \right]_e dzdy - \left[ \rho u \phi - \Gamma_\phi \frac{\partial \phi}{\partial x} \right]_w dzdy + \\ & \left[ \rho v \phi - \Gamma_\phi \frac{\partial \phi}{\partial x} \right]_s dx dz - \left[ \rho v \phi - \Gamma_\phi \frac{\partial \phi}{\partial x} \right]_n dx dz + \\ & \left[ \rho w \phi - \Gamma_\phi \frac{\partial \phi}{\partial x} \right]_t dx dy - \left[ \rho w \phi - \Gamma_\phi \frac{\partial \phi}{\partial x} \right]_b dx dy = (\bar{S}_\phi) dx dy dz \end{aligned} \quad (4.4)$$

According to Eq. (4.4), there is a combined convective and diffusive flux at the face of the control volume. This concept was introduced by Patankar and is defined in Eq.

(4.5) and illustrated in Figure 4.2 [46].

$$J_i \equiv \rho u_i \phi - \Gamma_\phi \partial_i \phi \Rightarrow J_i \equiv F_i + D_i \quad (4.5)$$

Introducing Eq. (4.5) into Eq. (4.4):

$$J_e - J_w + J_n - J_s + J_b - J_t = \bar{S}_\phi dx dy dz \quad (4.6)$$

At this point it is important to note that the fluxes in Eq. (4.4) and Eq. (4.6) are defined at the control volume surfaces of the control volume in each direction. However, they need to be expressed according to the value of the neighboring nodal points. The evaluation of the transport property  $\phi$  by means of convection and diffusion at the face of each control volume is the principal and crucial point in the FV discretization technique. Several methods have been developed through the years in order to find an appropriate approximation to evaluate the convection-diffusion flux at the face of the control volume. In this sense, Patankar developed the so-called Power Law scheme [46], which is an approximation of the exact solution of the one-dimensional convection diffusion equation for the property  $\phi$ , and presents an excellent behavior in order to describe the convection-diffusion flux for the transport property at the face of the control volume.

The Power Law scheme is represented by the equation below;

$$A(P_i) = \max \left[ 0, \left( 1 - 0.1 * \left| \frac{F_i}{D_i} \right| \right)^5 \right] = \left[ \left[ 0, \left( 1 - 0.1 * \left| \frac{F_i}{D_i} \right| \right)^5 \right] \right] \quad (4.7)$$

The operator  $\llbracket a, b \rrbracket$  in Eq. 4.7 is used to choose the larger of the two numbers in the set, and the relation  $F_i / D_i$  is known as the cell Peclet number.



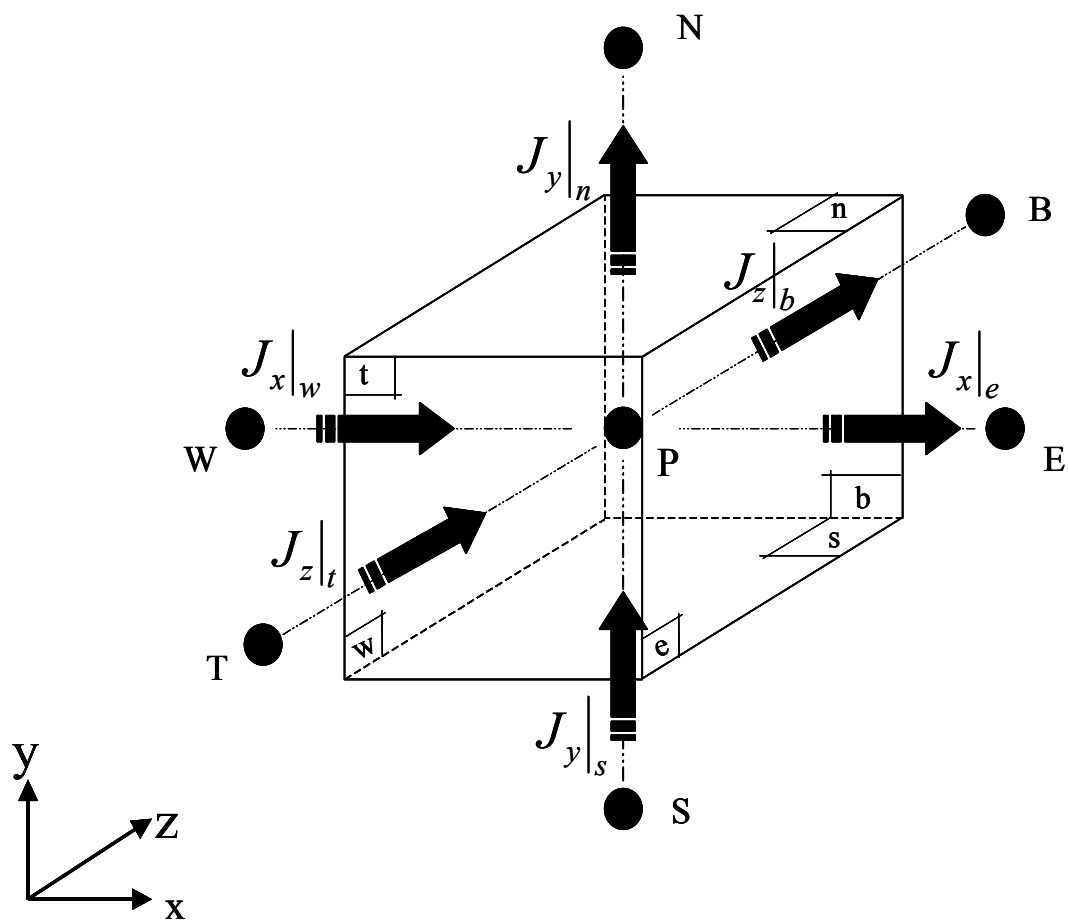


Fig. 4.2 Convection-diffusion fluxes at the faces of the control volume

$$Pc_i \equiv \frac{F_i}{D_i} \quad (4.8)$$

and

$$F_i = (\rho u_i) \Delta A \quad (4.9)$$

$$D_i = \left( \frac{\Gamma_\phi}{\delta x_i} \right) \Delta A \quad (4.10)$$

If  $Pc_i=0$ , the phenomenon is considered as pure diffusion and no convection is present. In this case the property  $\phi$  will be spread equally in all directions. But if  $Pc_i=\infty$ , then the phenomenon is pure convective and no diffusion is present. Here the influence in the property  $\phi$  becomes predominant in the upstream flow direction. Specific details in the derivation of the Power Law scheme can be found in the publications of Patankar and Versteeg and Malalasekera [44,46].

Finally, the discretized general transport equation, Eq. (4.1), in three-dimensions is given below.

$$a_p \phi_p = \sum_{i=1}^n a_i \phi_i + \bar{S}_\phi \Delta x \Delta y \Delta z \quad (4.11)$$

In Eq. (4.11) the sub index “ $P$ ” refers to the nodal point and the “ $n$ ” should be interpreted as the number of neighbors surrounding the nodal point (6 for a three-dimensional problem, 4 for a two-dimensional problem, and 2 for a one-dimensional problem) for a two-node formulation. The coefficients in the right hand side take the following form:

$$a_i = D_i A (Pc_i) + [\pm F_i, 0] \quad (4.12)$$

The sign in front of the convective term ( $F_i$ ) will depend on the direction of the flow and the operator  $[\ ]$  will return the larger of the two numbers in the set.

The  $a$ 's coefficients for each direction are defined as follows.

$$a_E = D_e A(|Pc_e|) + [-F_e, 0] \quad (4.13)$$

$$a_W = D_w A(|Pc_w|) + [F_w, 0] \quad (4.14)$$

$$a_N = D_n A(|Pc_n|) + [-F_n, 0] \quad (4.15)$$

$$a_S = D_s A(|Pc_s|) + [F_s, 0] \quad (4.16)$$

$$a_T = D_t A(|Pc_t|) + [-F_t, 0] \quad (4.17)$$

$$a_B = D_b A(|Pc_b|) + [F_b, 0] \quad (4.18)$$

And the coefficient for the nodal point  $a_P$  is computed by the following relation:

$$a_P = a_E + a_W + a_N + a_S + a_T + a_B \quad (4.19)$$

The last point to discuss in the discretization process is the treatment of the source term. The source term  $\bar{S}_\phi$  could be a function of the variable  $\phi$ . If such is the case this dependence could result in numerical instabilities, which precludes reaching a convergent solution. In FV discretization technique the source term is transformed by means of a linearization as shown below [46].

$$\bar{S}_\phi = S_c + S_p \phi_P \quad (4.20)$$

Only negative values of  $S_p$  are allowed to facilitate a diagonal dominance condition that ensures at least one solution to the linear system of equations [47].

Considering the source term linearization, the discretized general transport equation in three-dimensions is given below.

$$(a_p - S_p \Delta x \Delta y \Delta z) \phi_p = \sum_{i=1}^n a_i \phi_i + S_c \Delta x \Delta y \Delta z \quad (4.21)$$

The most common form for this equation in the literature accommodates the linearization term inside the  $a_p$  as shown in the equation below.

$$a_p \phi_p = \sum_{i=1}^n a_i \phi_i + b \quad (4.22)$$

and,

$$a_p = a_E + a_W + a_N + a_S + a_T + a_B - S_p \Delta x \Delta y \Delta z \quad (4.23)$$

$$b = S_c \Delta x \Delta y \Delta z \quad (4.24)$$

The second term on the left hand side of Eq. (4.22) takes the same forms as shown before in Eqs. (4.13)-(4.18). Now that the final form for the general transport equation has been defined, the next step is to develop the procedure for numerically computing the fluid flow.

#### 4.4 Fluid Flow Computation SIMPLE Algorithm

As has been stated previously the convection-diffusion equation can take any form of the mass conservation equation, momentum equations for X, Y, and Z as well as the energy equation, just by selecting the appropriate values of the variable  $\phi$  and the corresponding values of the diffusion coefficients.

At first sight it can be said that the procedure previously described for the general

transport equation is also the procedure for solving the momentum equations. However the real difficulty of the computation of the velocity field flow lies in the presence of the pressure gradients in the momentum equations. The pressure gradients are the physical driven potential momentum source for fluid flow. Hence, for a realistic problem the computation of the fluid velocity flow is coupled with the computation of the pressure field for the entire domain.

The solution of the momentum equation presents the following problems:

- i. The convective terms in the momentum equation contain non-linear quantities,
- ii. The equations are internally coupled because velocity components are presented in each momentum equation, and
- iii. The pressure field becomes important due to physical implication for the momentum equation but there is no separate transport equation to compute it.

The first two points can be handled by solving the velocity field iteratively. The problem with the pressure field exposed in the third point needs special treatment.

If the pressure field is known the problem for the field velocity flow can be handled by treating the velocity component for each direction as the dependent variable  $\phi$  as has been explained in the previous section.

For a compressible flow the mass conservation equation is used for computing the density distribution and in addition the energy equation is solved for the temperature distribution. Then, the pressure field can be computed by means of an equation of state once the density  $\rho$  and the temperature  $T$  are known. This implies that  $p = p(\rho, T)$ .

If the fluid is incompressible the density is constant and not linked to the pressure

via a state equation. In this case the solution of the velocity field and the pressure distribution are coupled. The consequence is the following constraint:

*If the proper pressure distribution is used in the momentum equations, then the resulting velocity field must satisfy the Mass conservation equation.*

The implication is that the pressure field is indirectly specified via the mass conservation equation [44].

Adopting a numerical strategy known as the SIMPLE algorithm proposed by Patankar and Spalding in 1972 the pressure-velocity connection is solved. The *SIMPLE* algorithm for the computation of the flow field stands for Semi-Implicit Method For Pressure-Linked Equations [46].

In general for this algorithm, the discretization of the momentum equation for the whole domain under the assumption of a known pressure distribution is made and then the velocity field for  $u$ ,  $v$ , and  $w$  is computed. If the velocity distribution satisfies the continuity equation then the solution is found; otherwise a new pressure distribution should be proposed and so forth until convergence. Successive approximations or successive iterations for the momentum equations and appropriate corrections for the pressure field can be used in order to achieve this goal.

The sequence of the SIMPLE algorithm is given below. The derivation of the equations as well as specific details of the procedure can be found in Patankar's book [46].

1. Guess the pressure field  $p^*$  for the whole domain

A reasonable pressure distribution ( $p^*$ ) is guessed for the entire

computational domain. This pressure distribution will serve as an approximation for the correct pressure distribution that will be obtained after several iterations.

2. Solve the momentum equations to obtain  $u^*$ ,  $v^*$  and  $w^*$

The momentum equations are solved based on the guessed pressure distribution in step 1. The velocity distributions, after solving the momentum equations, also are defined by  $u^*$ ,  $v^*$ , and  $w^*$  because they are computed based on the guessed pressure distribution. This velocity distribution will provide an approximation to the correct velocity field.

3. Find the pressure correction  $p'$  for the whole domain

A temporal variable defined as  $p'$  (*p-prime*) will be computed. This  $p'$  is computed via a set of a linear algebraic system of equations for the entire domain. The coefficients for the linear system of equations are obtained via an integration of the mass conservation equation for each control volume using the velocity values computed in step 2.

The main attribute of this temporal pressure is that if the right pressure and the correct velocity field are used, then the  $p'$  distribution is equal to zero in the whole domain and no further pressure correction is needed.

4. Update the pressure field ( $p$ )

The pressure distribution  $p$  is updated by the addition of the guessed pressure  $p^*$  and the pressure correction  $p'$ , as indicated in Eq. (4.25).

$$p = p' + p^* \quad (4.25)$$

As has been stated before,  $p'$  is equal to zero only if the guessed pressure distribution imposed in step 1 satisfies the mass conservation equation. Under this assumption  $p = p^*$  and no more corrections are needed.

5. Update  $u$ ,  $v$ , and  $w$  from their guessed values using the velocity correction formula:

$$u_i = u_i^* + \frac{Area}{a_p} (\Delta p') \quad (4.26)$$

$\Delta p'$  represents the net pressure (computed in step 3) acting over each velocity component and  $a_p$  is the nodal point coefficient computed according to Eq. (4.23).

As can be deduced from Eq. (4.26) the corrected velocity field is the addition of the started velocity field (step 2) and a coefficient that represents the driving potential for fluid motion (second term on the right hand side).

6. Solve for any other  $\phi$  variables

Once the velocity field has been computed, any other scalar variable such as temperature, concentration, etc. involved in the problem could be computed.

7. Check to see if the flow field solution satisfies the mass conservation equation

In this step the pressure distribution and the velocity field are tested for satisfying the mass conservation and for satisfying convergence. If none of them are satisfied then the procedure is repeated again and in step 1 the corrected pressure ( $p$ ) is treated as the new guessed pressure distribution  $p^*$



and the steps are repeated until convergence.

When solving the momentum equation it is important to specify the nodal location for all the variables in question. Even though this step seems to be irrelevant there are some interesting aspects that will be discussed thoroughly in the following section.

#### 4.5 Staggered Grid

The simplest and obvious strategy when allocating the nodal points for all variables in the computing process is to choose the same nodal location points and use the same set of control volumes for all variables in question. Such a grid is called a *collocated grid*. This implementation has the advantage of an easy implementation even for complex geometries and, the use of low memory resources for storing the needed information for the computational process. However, the use of this implementation can produce unrealistic wavy velocity and pressure distributions without any real physical meaning for the problem [44,46].

In order to avoid this kind of problem, the idea of using different grids for the velocity components was first proposed by Harlow and Welch in 1965 [48] and has become a standard implementation for the fluid flow numerical simulation.

In this arrangement the nodal points for the velocity components  $u$ ,  $v$ , and  $w$  are displaced with respect to the main grid point or node where the pressure and any other scalar quantity of computation interest in the domain are stored. This arrangement is called the *staggered grid* and is implemented such that the nodal location for the velocity components lies on the face of the main grid control volume. The main grid control

volume serves for allocating the pressure nodal points and also for allocating any other scalar variable such as temperature, density, viscosity, etc.

Figures 4.3 to 4.5 can be used to illustrate the concept of staggered grid for each  $u$ ,  $v$ , and  $w$  velocity component in a three-dimensional geometry.

Among the advantages of using the staggered grid is that any wavy or unrealistic velocity distributions that satisfy the mass conservation equation are avoided. The second important advantage is that the natural driving force for any velocity component is the result of pressure difference between two adjacent grid points [46]. The staggered grid generates the velocity components at the exact point where they are required for the computation of the transport of the convection-diffusion and no extra interpolation is needed [44]. Finally, the staggered grid is constructed such that the domain peripheral boundary coincides with the staggered lines and there is no need for fictitious cells located beyond the domain [49].

The main disadvantage of using a staggered grid is the increase of the memory resources to store all of the variables involved in the numerical procedure.

A scheme for a staggered grid in a three-dimensional geometry is presented in Figure 4.6.

Once the procedure to discretize the momentum equations and the energy equation using a finite volume technique, and the steps for the SIMPLE algorithm for linking the velocity and pressure fields has been discussed, the next step is to describe a numerical technique in order to solve the linear system of equations obtained after the nodal discretization. This procedure is described in the following section.

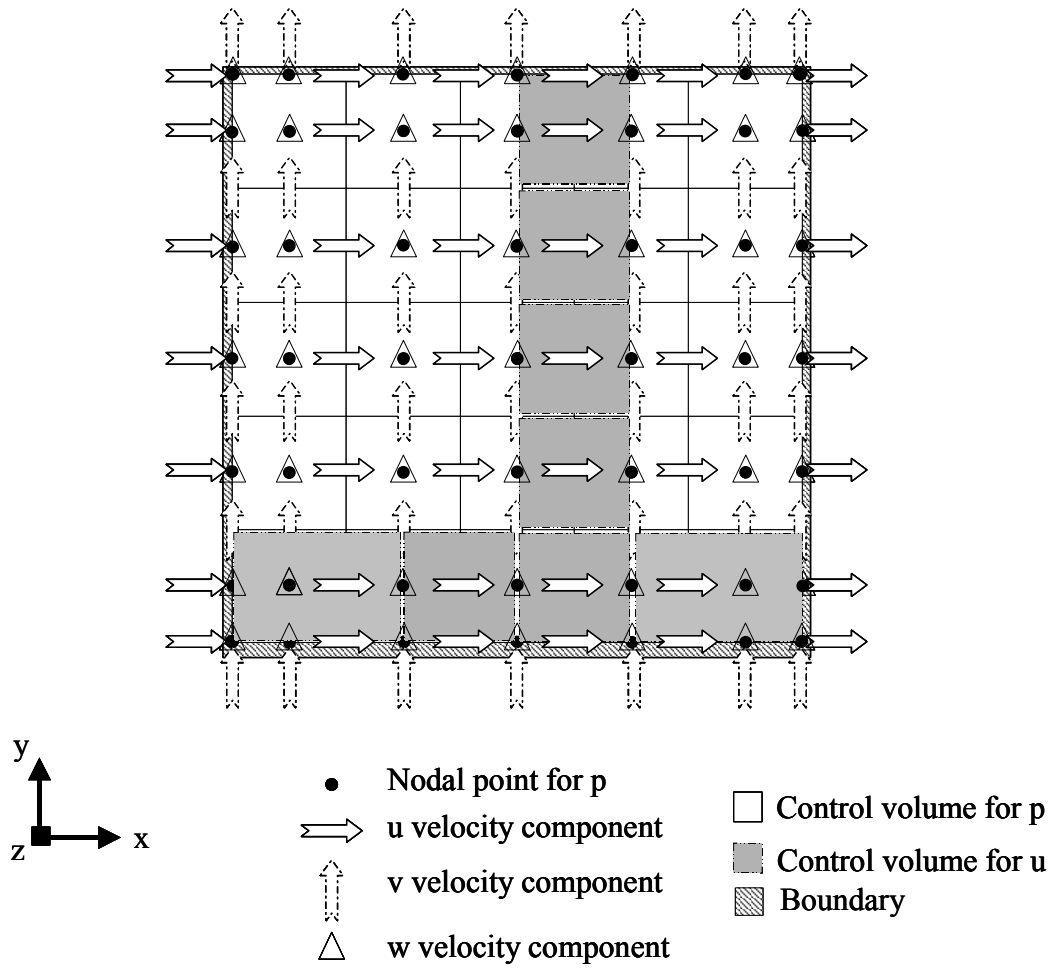


Fig. 4.3 Staggered grid for  $u$ -velocity component at a constant  $z$ -plane

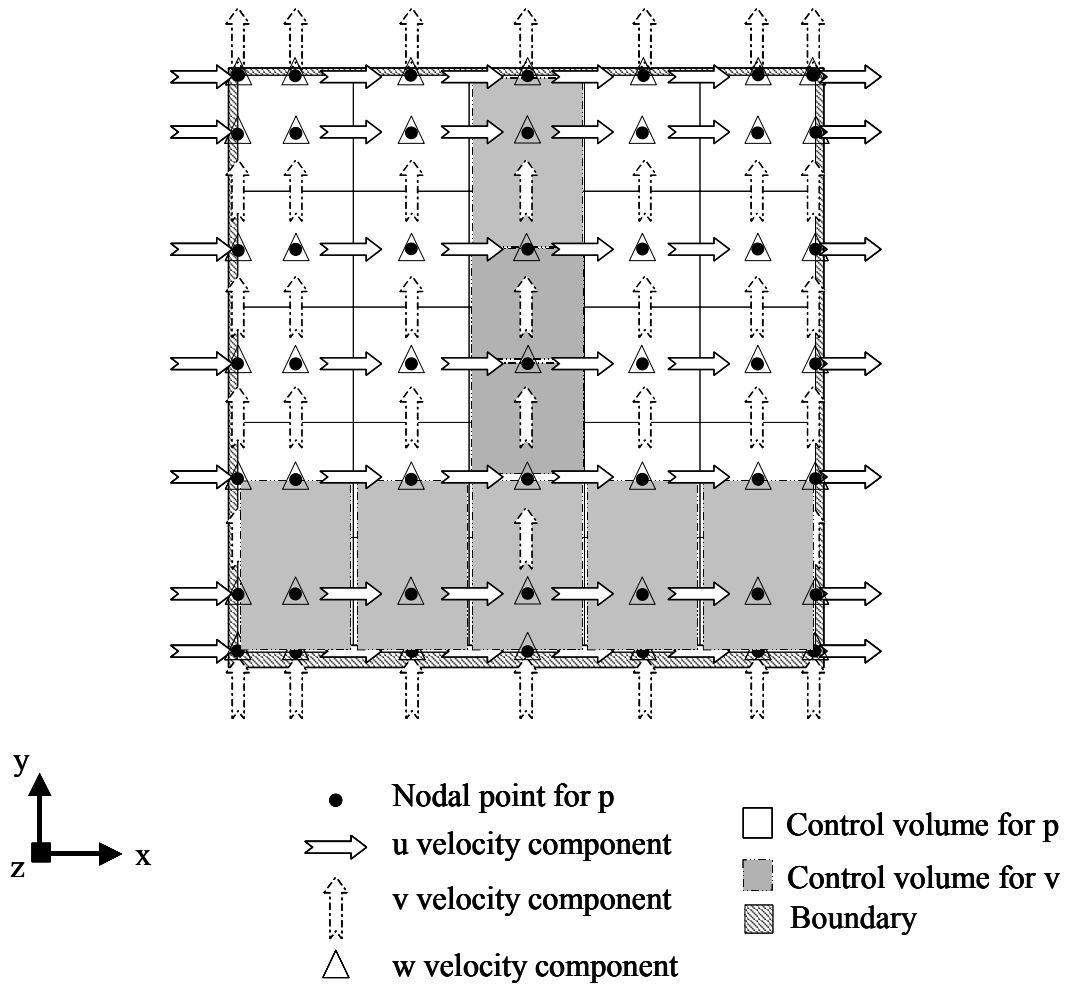


Fig. 4.4 Staggered grid for  $v$ -velocity component at a constant  $z$ -plane

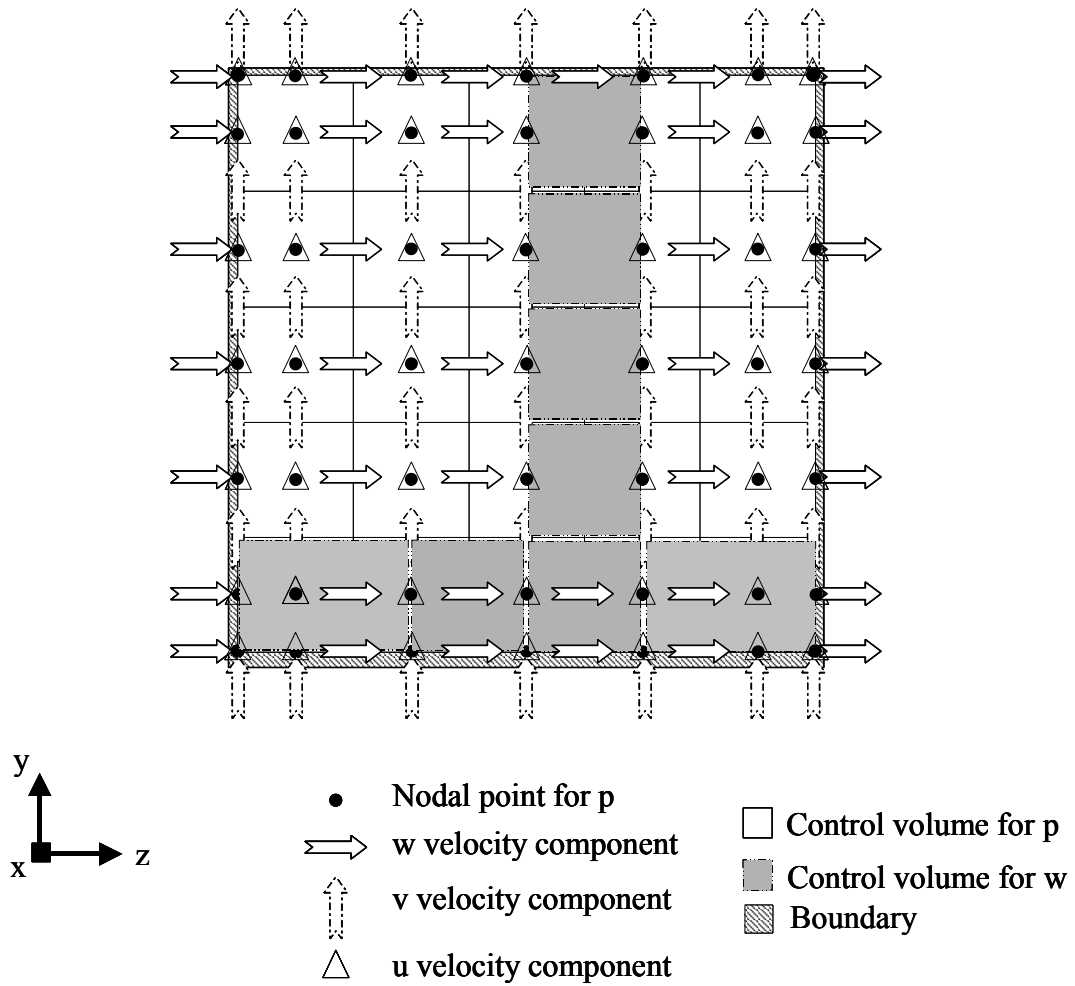


Fig. 4.5 Staggered grid for  $w$ -velocity component at a constant  $x$ -plane

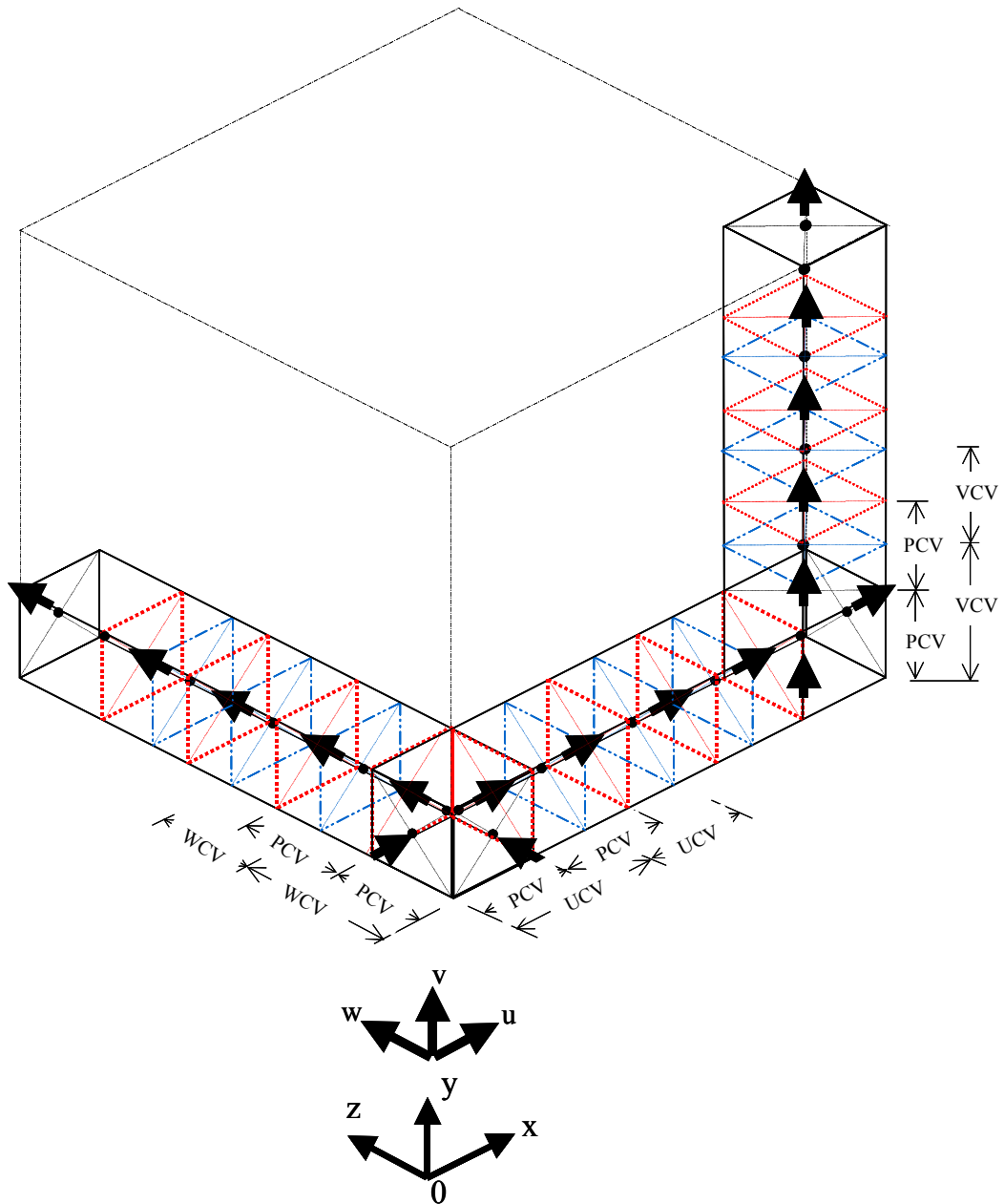


Fig. 4.6 Staggered grid in a three-dimensional geometry

#### 4.6 Line-by-line Tri-Diagonal Matrix Algorithm (TDMA)

Until now the method to numerically discretize the fluid flow and heat transfer governing equations has been discussed and this process results in a linear system of algebraic equations.

There are several numerical techniques for handling the solution of the algebraic system of equations and there is no any condition to choose one specific technique depending on the discretization technique. Although the huge quantity of numerical techniques for solving the linear algebraic system of equations, these methods have been classified in *direct* and *indirect methods*. Between the direct methods are Cramer's rule, the Matrix Inversion, and the Gaussian elimination. All of these methods become prohibitive as the number of unknowns increase because of the memory storage and the computation itself.

The alternative is the implementation of *iterative methods*. The term iterative method refers to a large range of techniques that use successive approximations to obtain accurate solutions to the linear system at each step. The iterative methods are divided into *stationary methods* and *non-stationary methods* [50].

The term non-stationary iterative method refers to a wide range of techniques that use successive approximations to obtain the solution of the linear system via the construction of orthogonal vectors; and the most representative methods are those belonging to the family of the Conjugate Gradients (CGs methods). The stationary methods are widely applied in CFD and some well known examples are the Jacobi, the Gauss-Seidel point by point, the Successive Over Relaxation (SOR), etc.

The previously mentioned stationary techniques are of easy numerical implementation but present slow convergence when dealing with a large system of equations, or a large number of grid points is involved as generally happens with numerical simulations for two- and three-dimensional geometries.

On the other hand, the numerical discretization for one-dimensional problems gives, as a result, a tri-diagonal matrix that needs to be solved. The Tri-Diagonal Matrix Algorithm (TDMA) or Thomas Algorithm [51] is a numerical technique to solve such problems and due to its simple and economical implementation it has become of wide spread use in CFD [44].

As previously mentioned any tri-dimensional or two-dimensional geometry can be approximated as a group of nodes aligned in such a way that the geometry is composed of several one-dimensional geometries or lines. Thus a combination of a line-by-line fashion and a TDMA algorithm can be applied for solving multi-dimensional problems.

The procedure is to choose a grid line and assume that the neighboring lines are known from the previous iteration, then the unknowns for this line are computed by the TDMA algorithm. This procedure is repeated for all of the lines in one direction and it can be alternately used on different directions.

In order to improve the convergence ratio the more recent values of the unknowns is used and in this case a combination of a Gauss-Seidel-line-by-line is adopted.

In the case of three-dimensional geometries this procedure can be implemented for each plane in the coordinate directions. In this sense a Gauss-Seidel-line-by-line method is applied plane-by-plane.



## CHAPTER V

### VALIDATION AND GRID INDEPENDENCE

#### 5.1 Introduction

One of the main objectives for this research is to develop a FORTRAN code to numerically simulate the *mixed convective flow over a three-dimensional horizontal backward-facing step*.

In order to establish that the numerical code is validated and ready to make parametric runs it is necessary to demonstrate that the code is able to reproduce results for benchmark problems. This process is known as *code validation* and it is important not only for testing the precision and accuracy of the numerical code but also for exploring its capabilities and limitations.

The first part of this chapter deals with the validation process and the second part with the grid independence study.

#### 5.2 Numerical Validation

The process of numerical validation consists of running the numerical code under specific conditions for benchmark problems and then comparing the obtained results with the experimental or theoretical data published in the literature. However, as it was established in Chapter II, the lack of previous experimental or numerical data in the literature for the mixed convective flow over a three-dimensional horizontal backward-facing step precludes the direct numerical validation of the numerical code developed for

this research.

In order to validate this numerical code, three problems closely related to the mixed convective flow over the three-dimensional horizontal backward-facing step were considered. In each case some specific hydrodynamic and thermal flow features were compared with the solutions for benchmark problems published in the literature, as described in the next sections.

### ***5.2.1 Forced Convective Flow through a Square Horizontal Channel***

The first test case was that for simulating a pure forced convective flow through a three-dimensional horizontal square duct heated from below at a constant temperature. The flow at the channel inlet was considered to have a uniform velocity and a constant temperature. The Reynolds and Prandtl numbers were set as  $Re=100$  and  $Pr=0.72$ , respectively.

The channel's total length was fixed to be 40 times the hydraulic diameter to ensure fully developed flow conditions at the channel exit, while the channel walls were considered as adiabatic except the bottom wall, which was subjected to a constant temperature. The grid chosen for this experiment was uniform and a total of  $3.2 \times 10^5$  nodes were distributed along the entire geometry so that the stream-wise direction had a total of 200 control volumes and a total of 40 control volumes were allocated for each of the other coordinates. This grid size was set following the studies by Ravi Sankar et al., [52] for a forced and mixed convective flow through a square channel. In this publication [52] a total of 31 by 31 control volumes and a control volume's length of

$5 \times 10^{-4}$  m in the main flow direction were enough to establish grid independence. For the validation test in this research, almost 10 nodal points were added to the transverse and span-wise directions, while the increments in the axial direction were of the same order of magnitude as expressed before.

Even though the test case seems to have no relation with the problem in question, the relevance for testing the code under these conditions was to exhibit that the numerical code is capable of simulating flows in a three-dimensional geometry.

The average Nusselt number distribution, the average Fanning friction factor distribution, as well as the velocity profile for the stream-wise velocity component along the span-wise center plane were monitored through the channel. The results are plotted in Figures 5.1 and 5.2.

As can be appreciated in the above referenced figures, at the channel inlet both the average Nusselt number and the Fanning friction factor start with a high value and asymptotically decrease to reach the fully developed values at the channel exit. At the channel exit, conditions of fully developed flow are achieved as shown in the development of the velocity profile in Figure 5.2.

The numerical predictions at the channel exit for the average Nusselt number, the Fanning friction factor, and the maximum value of the stream-wise velocity component at the channel exit were compared against the established results for a fully developed flow in a square channel as published by Shah and London [53]. The comparison is summarized in Table 5.1.

Table 5.1 Validation for a forced convective flow through a square channel

	Nu	fRe	$u_{\max}/u_o$ (span-wise center plane)
Shah and London, 1978	2.4370	14.2270	2.0962
Present	2.4110	14.1930	2.0902
Difference	1.06%	0.24%	0.28%

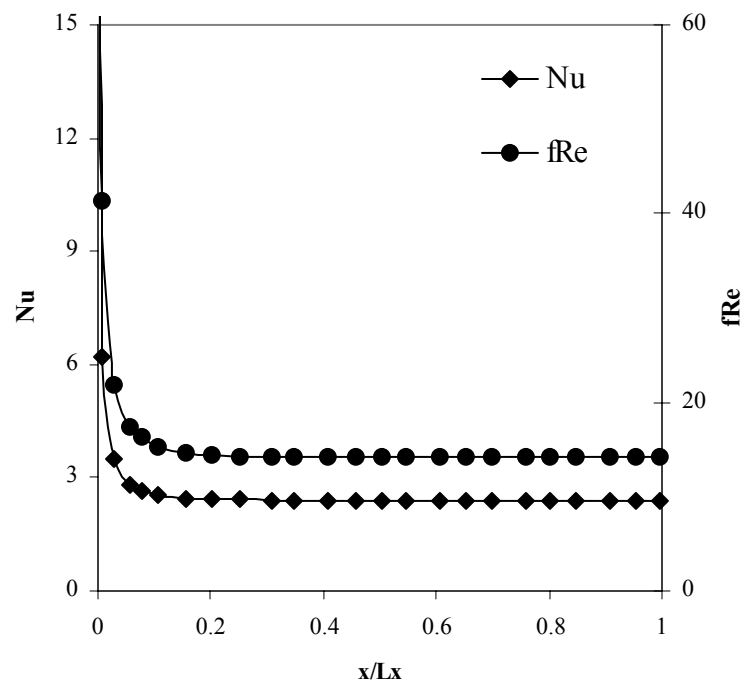


Fig. 5.1 Nusselt number and Fanning friction factor distributions averaged in the span-wise direction for forced convective flow through a square channel.  $Re=100$  and  $Pr=0.72$

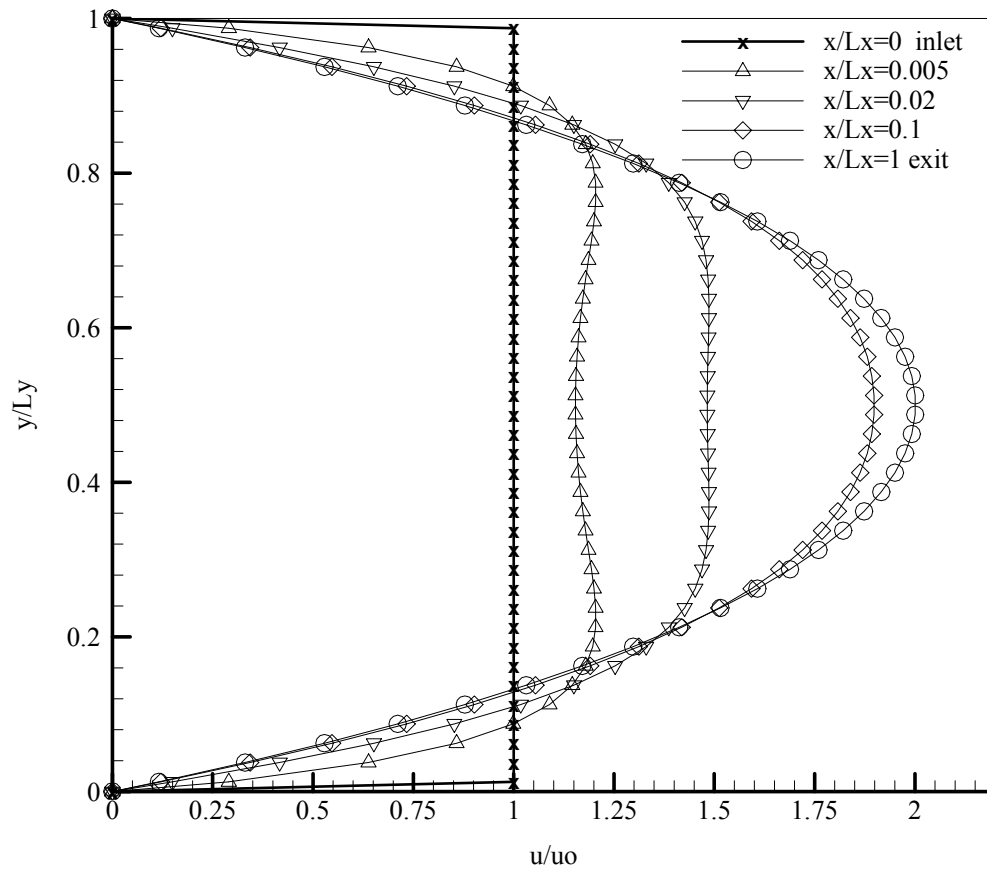


Fig. 5.2 Stream-wise velocity profiles along the central plane for a forced convective flow through a square channel.  $Re=100$  and  $Pr=0.72$

It is evident from Table 5.1 that the discrepancy is minimal between the present numerical predictions and the theoretical values from Shah and London [53]. Hence the

numerical code is a trusted tool for predicting the forced convective flow in a three-dimensional horizontal channel.

### ***5.2.2 Mixed Convective Flow through a Rectangular Horizontal Channel***

The second test case was that of simulating a mixed convective flow in a straight horizontal channel heated from below. The numerical predictions were compared with the results published by Incropera and Schutt in 1985 [54] for a horizontal rectangular channel with a width-to-height ratio equal to 2. In this publication the effects of a combined entry region for low and high Prandtl numbers as well as different boundary conditions for the heating process were considered. At the channel inlet the flow was treated to be uniform with a constant velocity ( $U_0=\text{constant}$ ) and isothermal ( $T_0=296\text{ K}$ ).

Two different heating conditions were considered for the validation test. For the first case, the temperature of the bottom and top walls were maintained at a high constant value while the sidewalls were kept as adiabatic. The working fluid in this example was water ( $Pr=6.5$ ) and the velocity profile at the inlet was fixed to be uniform for the combined entry region flow so that the Reynolds number ( $Re$ ) is equal to 500. The buoyancy driven potential was fixed such that the Grashof number ( $Gr$ ) is equal to  $1.55 \times 10^5$ .

The second study case was for the same channel geometry, but the mixed convective flow was simulated by subjecting the bottom wall to a constant heat flux condition. The top and side walls in this study case were considered to be adiabatic and the working fluid was air with  $Pr=0.71$ . Under these conditions, the modified Grashof

number ( $Gr^*$ ) defining the buoyancy driven potential flow had a constant value equal to  $11.40 \times 10^6$ . The domain discretization was done on a uniform grid and a total of  $3.2 \times 10^5$  nodal points were allocated along the three-dimensional channel. In their study Incropera and Schutt used a 26 by 26 grid size for the transverse and span-wise directions and the space between nodal points in the stream-wise direction was equal to  $1 \times 10^{-3} \text{m}$  [54]. In the present approximation a total of 400, 20, and 40 grid points were allocated in the stream-wise, transverse, and span-wise directions, respectively, while the distance between nodal points in the stream-wise direction was  $4.5 \times 10^{-3} \text{m}$ .

The comparison between the predicted values and those published for test case 1 and case 2 are presented in Figures 5.3 and 5.4, respectively. It is evident from these figures that the discrepancies between the present numerical predictions and the published results in both cases are minimal and thus the numerical code is able to simulate the mixed convective flow through a rectangular channel subjected to constant wall temperature or constant heat flux heating boundary conditions.

### ***5.2.3 Forced Convective Flow over a Three-Dimensional Horizontal Backward-Facing Step***

The third validation test was that for simulating a pure forced convective flow over a three-dimensional horizontal backward-facing step subjected to a constant heat flux along the bottom wall. The heating zone stretched from the end of the step to the channel exit.

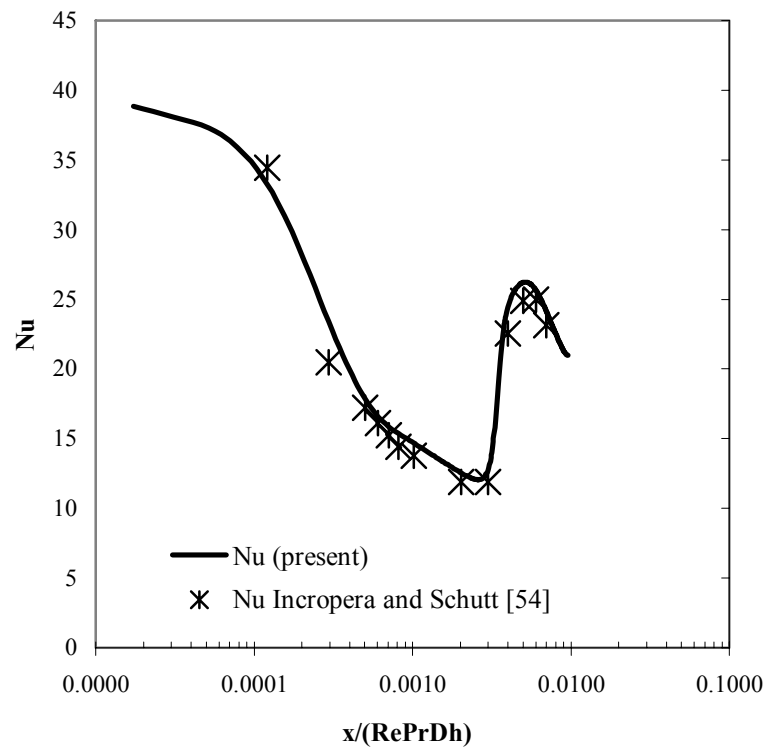


Fig. 5.3 Span-wise averaged Nusselt number distribution for a mixed convective flow in a rectangular channel heated from below and top at a constant temperature.  $Re=500$ ,  $Pr=6.5$ , and  $Gr=1.55 \times 10^5$



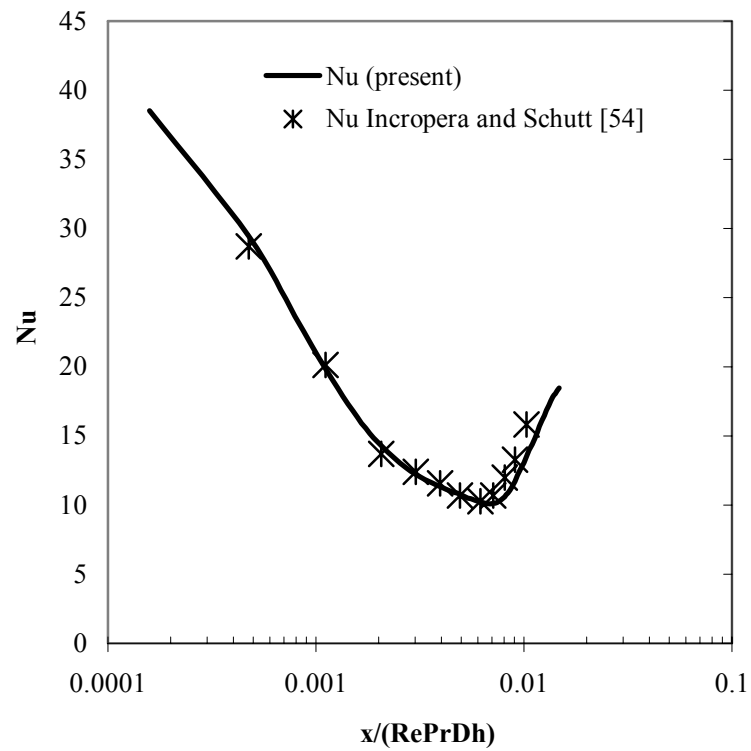


Fig. 5.4 Span-wise averaged Nusselt number distribution for a mixed convective flow in a rectangular channel heated from below at a constant heat flux.  $Re=500$ ,  $Pr=6.5$  and  $Gr^*=11.40 \times 10^6$

This validation test was divided into two parts. The first one deals exclusively with the fluid flow problem over a backward-facing step with a duct aspect ratio  $AR=8$ , an expansion ratio  $ER=2.02$ , and a step length equal to two times the step height. The numerical predictions using the present code were compared against the measurements published in 2003 for the same geometry by Armaly et al., [17]. The so-called  $x_u$ -line along the span-wise direction and the velocity profile for the stream-wise velocity component at specific axial (direction of the main flow) planes were used for validating the code. These distributions are presented in Figures 5.5 and 5.6 for  $Re=343$  and 512.

The uniform grid used for this simulation was similar to the one used by Nie and Armaly in their numerical solution for this problem [19]. In the present numerical simulation a total of  $3.36 \times 10^5$  nodal points distributed in  $140 \times 40 \times 60$  control volumes along the stream-wise, transverse, and span-wise directions, respectively.

The second part of the validation for the flow over a three-dimensional backward-facing step deals with the heat transfer problem. The three-dimensional geometry defined previously for the fluid flow problem was also used for the forced convective flow problem. In this case the bottom wall was submitted to a constant heat flux while all the others walls including the step were considered as non-conductive and adiabatic.

Flow at the inlet was considered to be fully developed and isothermal. The Reynolds number was defined based on the channel height and the bulk velocity at the channel inlet and was fixed at 400.

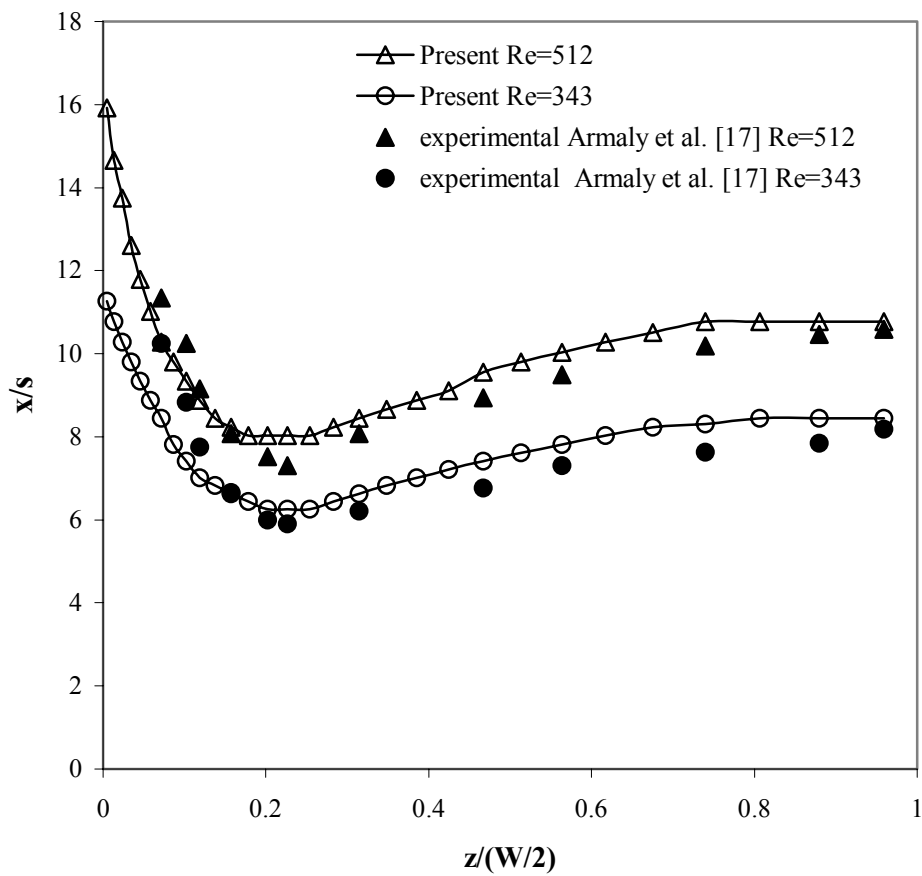


Fig. 5.5 Span-wise  $x_u$ -line distribution adjacent to the bottom wall.  $z/(W/2)=0$  side wall and  $z/(W/2)=1$  span-wise central plane

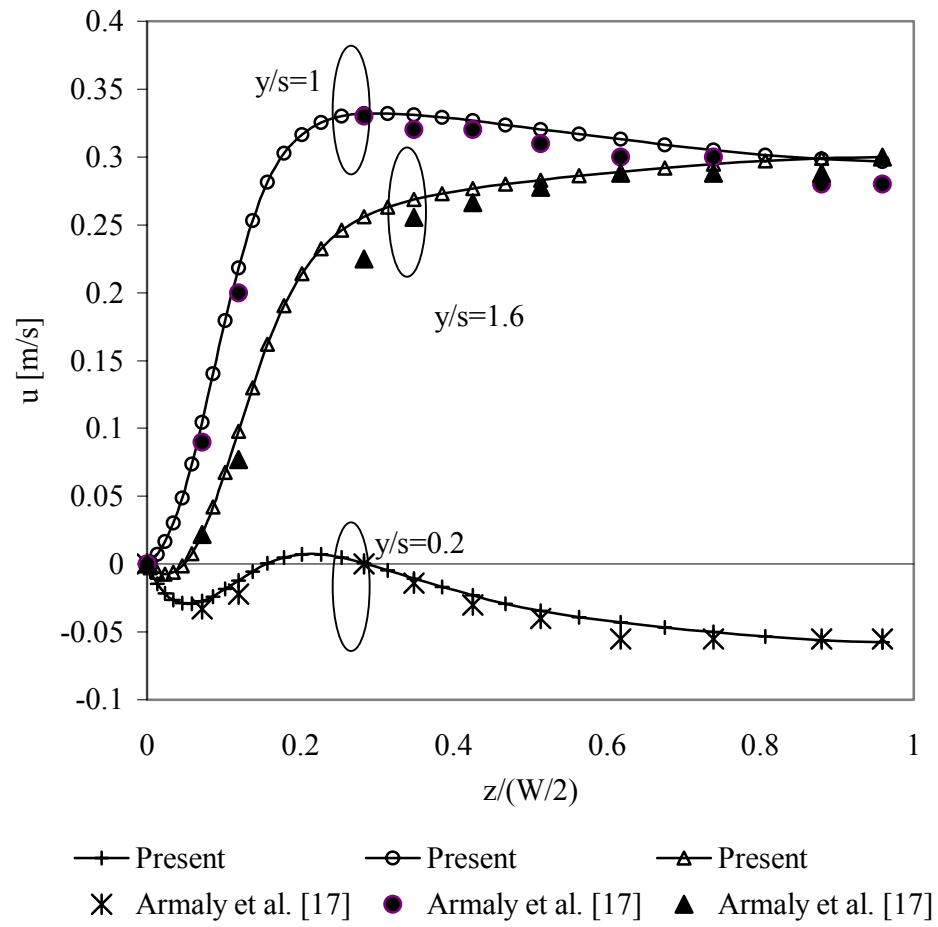


Fig. 5.6 Span-wise  $u$ -velocity component distributions at different transverse planes for  $Re=343$ .  $z/(W/2)=0$  wall and  $z/(W/2)=1$  (span-wise central plane)

The validation test was completed by comparison of the local Nusselt number distribution evaluated along the heating wall and at the constant plane  $x/s=6.6$ . Where  $x$  represents the stream-wise direction and  $s$  is the step height. The results are plotted in Figure 5.7.

As has been demonstrated in this chapter, the numerical predictions obtained with the developed numerical code, present an excellent agreement with the published data in the specialized literature [52-54, 17]. Thus it can be concluded that the developed numerical code is an accurate and extremely versatile numerical tool to study heat transfer and fluid flow over a three-dimensional backward-facing step. The next step is to select a grid size, which yields grid independence solutions.

### 5.3 Grid Setup

The grid generation process in a three-dimensional geometry consists of subdividing the computational domain into small parallelepipeds called control volumes.

The geometry considered in this study is shown in Figure 1.1. The backward-facing step (*solid region*) and the fluid flow region (*working fluid*) have different thermo-physical properties, hence the computational domain presents discontinuities. In order to handle these discontinuities the computational domain is divided such that the control volume faces coincide with the location of the discontinuities as well as the physical boundaries. At the center of each control volume a grid point or nodal point is deployed. This adopted practice is commonly found in the finite volume discretization and is known as the “*practice B*” [46].

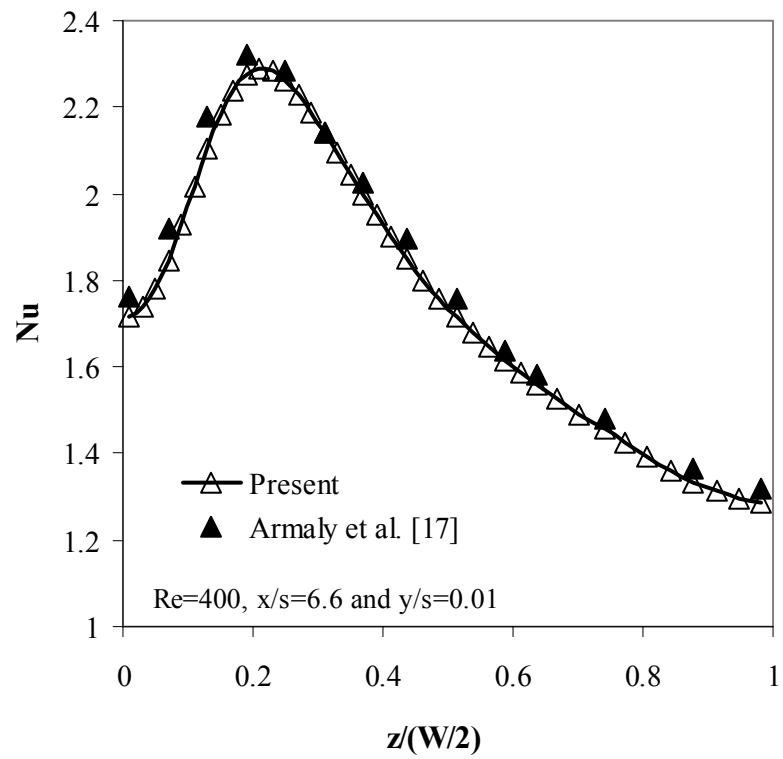


Fig. 5.7 Local Nusselt number distribution for a forced convective flow over a three-dimensional backward-facing step along the stepped wall at  $x/s=6.6$  plane.  $z/(W/2)=0$  side wall and  $z/(W/2)=1$  span-wise central plane

There is no restriction for specifying the length or size of the control volumes in the grid generation process. This grid could be either uniform or non-uniform. Some authors recommend the use of smaller control volumes in the region of strong variations or gradients and the use of larger control volumes in the region where gradients are not steep [55]. In this sense a fine grid is adopted in the region of strong gradients and a coarse grid is implemented in the region of small variations. Thus optimizing computational resources.

The concept for constructing a non-uniform grid by means of a geometrical progression is described by Patankar [56]. This idea is adopted in this numerical research; however, the mathematical relations considered here for deploying the non-uniform grid in the three-dimensional computational domain are quite different for those presented in the literature cited above. The mathematical relation used for setting up the grid in the preset research is the following:

$$\delta_i(n) = \frac{L_i(e^n - 1)}{(e^N - 1)} \quad (5.1)$$

In this relation  $\delta_i(n)$  represents the distance to the face of the  $n$  control volume from a reference position generally a physical boundary (wall),  $L_i$  is the geometrical length that needs to be divided into the  $N$  total number of control volumes and, the  $e$  represents the grid expansion coefficient. It is recommended to keep the value of  $e$  between 1 and 1.2 for better results in the grid generation. A value of  $e=1$  means that the grid is uniform.

The following step is explains the setup configuration for the grid in each of the

three coordinate directions in this research.

The x-direction is the stream-wise flow direction and as a consequence is the largest dimension in the computational domain. According to the problem and the geometry shown in Figure 1.1, the backward-facing step length represents a small portion of the total length in the x-direction. Besides the velocity gradients in this zone are considered as negligible because at the channel inlet the flow is treated as a fully developed flow and the profile remains basically constant. In the region downstream of the backward-facing step the velocity gradients become large.

For the above reasons, in the x-direction a combination of a uniform and a non-uniform grid was used to discretize the domain. In the region upstream of the backward-facing step a uniform grid was used, and a maximum of 10 control volumes were deployed. The grid for the rest of the channel in the stream-wise direction was non-uniform according to Eq. (5.1). The result is a very fine grid in the vicinity of the step, and the control volume size grows progressively toward the channel exit.

To give a better understanding of the grid in the stream-wise direction, a bird's-eye view (constant y-plane) is shown in Figure 5.8.

As can be seen in Figure 1.1, the z-coordinate direction or the span-wise direction of the flow is the only dimension in the geometry that presents any kind of symmetry. The implementation of the grid in this direction takes advantage of this feature.



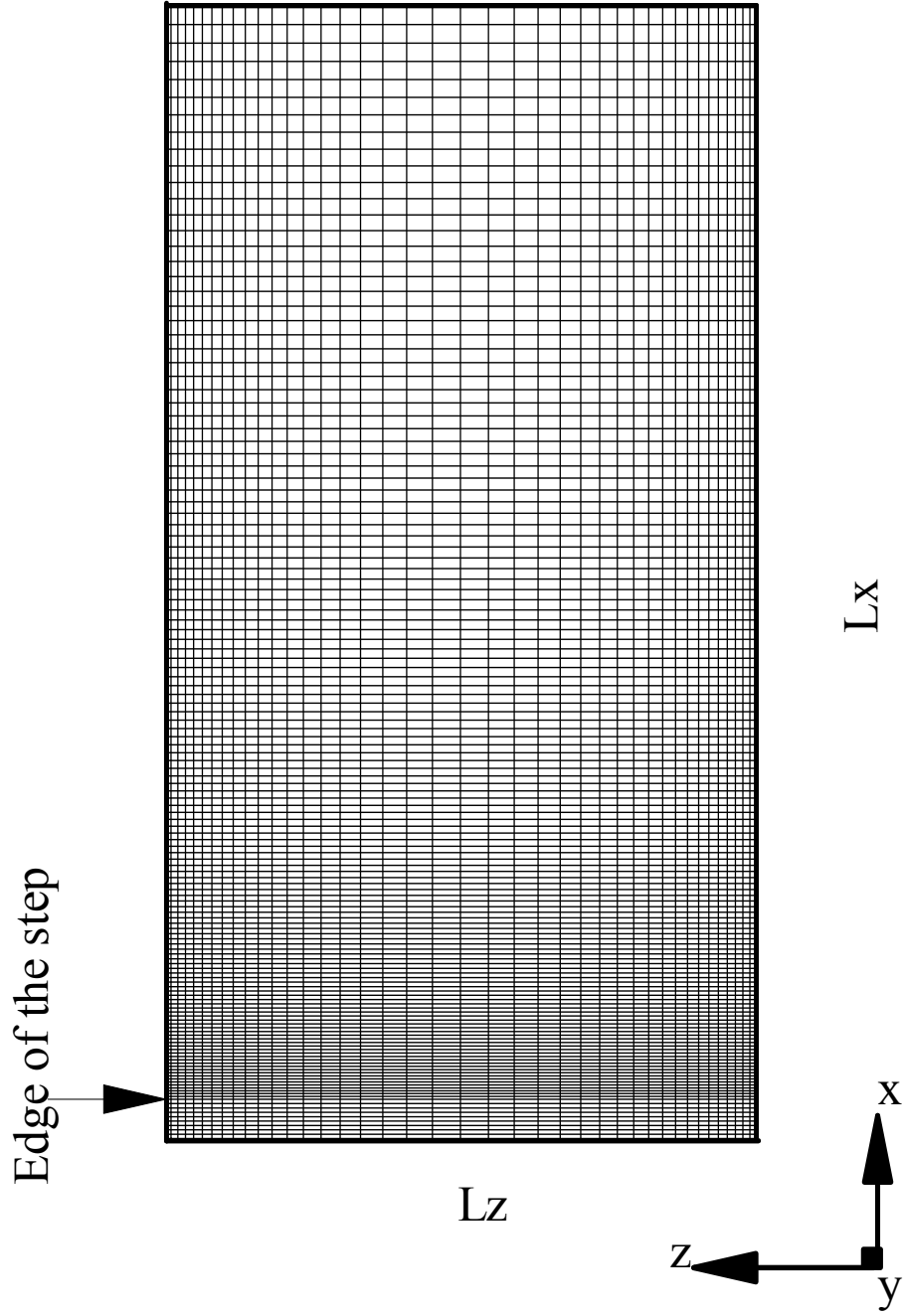


Fig. 5.8 Non-uniform grid setup in the x-direction in a constant y-plane

The smallest control volume in the  $z$ - direction is allocated at the side wall (plane  $z=0$ ), then the grid is spread using Eq. (5.1) and the largest control volume is allocated along the central plane in the span-wise direction at  $z=W/2$ . For the rest of the channel in the span-wise direction ( $W/2 \leq z \leq W$ ), the grid is a mirror image of the grid in the  $0 \leq z \leq W/2$  region. A drawing scheme for the grid in the  $z$ -coordinate direction for a constant  $x$ -plane is presented in Figure 5.9.

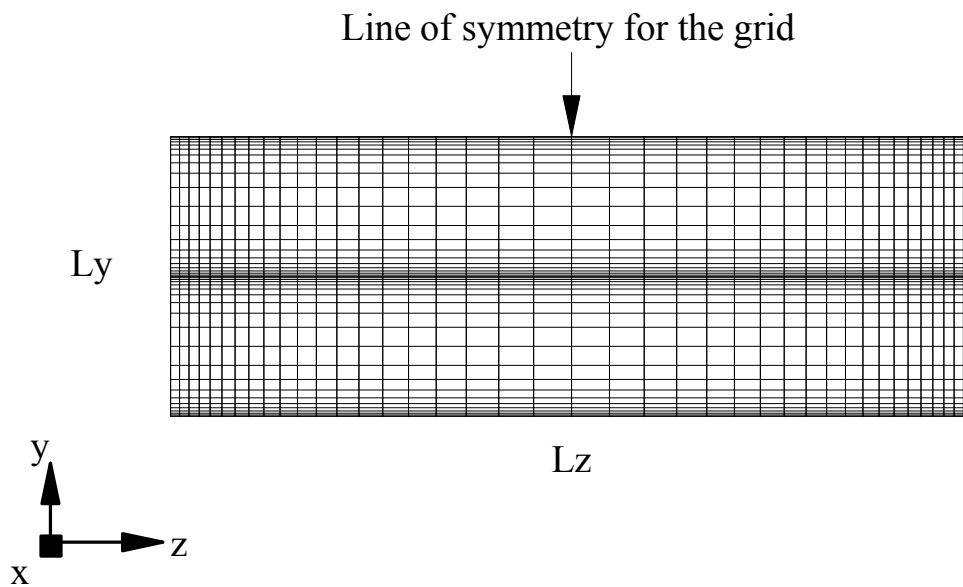


Fig. 5.9 Non-uniform grid in  $z$ -coordinate direction at a constant  $x$ -plane

The transverse flow direction or the  $y$ -coordinate direction presents three regions of significant importance. All of these regions coincide with solid boundaries like the

bottom wall, the top wall, and the top of the backward-facing step. An artificial symmetry line was considered at half of the channel in the transverse direction ( $y$ -coordinate direction) and similar to the  $z$ -coordinate direction the grid was constructed as a mirror image with respect to this artificial symmetry line by means of Eq. (5.1). In the following paragraph, details specific to the region between the bottom wall and the artificially symmetry line, are presented.

The artificial symmetry division is not only half of the channel, but also is the surface limiting the height of the channel. Also this is a critical zone where considerable gradients in velocity components and temperature will occur. For handling this situation a very fine grid is proposed in this zone as well as near the bottom wall of the channel. The result is a mirror non-uniform grid progressively increasing in the direction normal to the solid surface and to the artificial line of symmetry, such that the smallest control volumes are in the vicinity of the bottom wall and the step height and the largest control volumes are midway between these two reference surfaces. A schematic diagram of the grid generated in the transverse direction is shown in Figure 5.10 for a constant  $z$ -plane.

It is evident from Eq. (5.1) and Figures 5.8 to 5.10, that the grid spacing strongly depends on the expansion coefficient  $e$ . Selecting the appropriate value for this parameter to establish a grid independence solution is the central point of the following section.

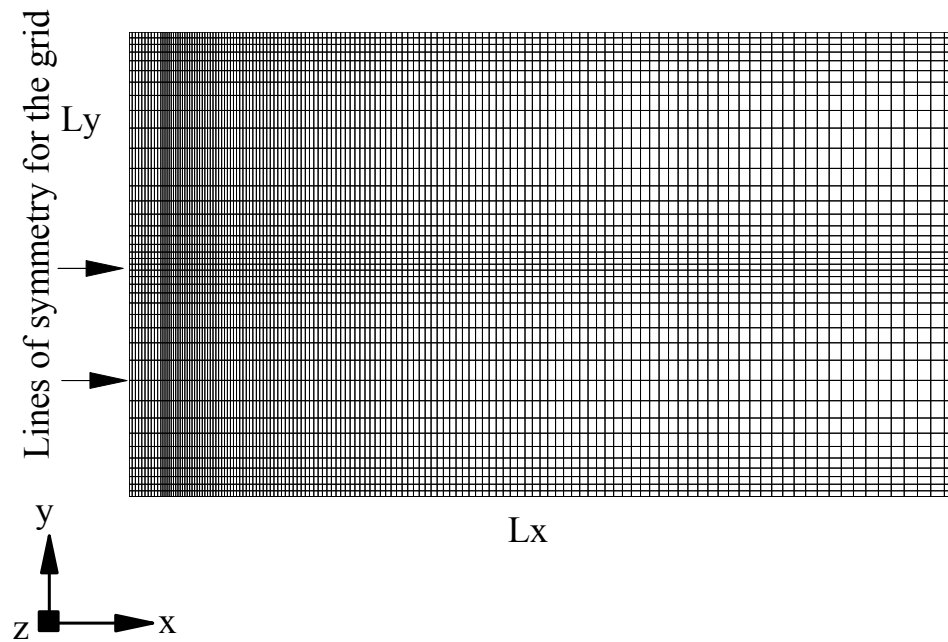


Fig. 5.10 Non-uniform grid for y-direction at a constant z-plane

#### 5.4 Grid Independence Study

It is necessary to conduct a series of tests in order to find the combination of the number of control volumes and the value for the expansion factor  $e$ , so that the numerical results will cease to be sensitive to these parameters. The grid independence study was conducted by using the most severe parametric values considered in this research for different grid densities. In all these cases the Reynolds number ( $Re$ ) and the Richardson number ( $Ri$ ) were fixed to be 200 and 3, respectively, while the fluid in consideration had a Prandtl number ( $Pr$ ) equal to 0.7. The convergence criterion was

chosen so that the normalized residuals for all the velocity components were less than  $1 \times 10^{-7}$  and less than  $1 \times 10^{-9}$  for the pressure. The parameter values monitored to declare grid independence, were the span-wise averaged Nusselt number ( $Nu_{avg\_exit}$ ) and the maximum u-velocity component ( $u_{max\_exit}$ ) at the channel exit.

The grid independence studies were conducted by varying the number of control volumes and the corresponding expansion factor in each coordinate direction at a time, while keeping the two parameters ( $n$  and  $e$ ) constant in the other two directions. A summary of the grid independence study is presented in Table 5.2.

According to Table 5.2 a value of  $e_z=1.20$  results in the minimum error for  $Nu_{avg\_exit}$  and for  $u_{max\_exit}$ . Thus this value is an appropriate value for this grid and the following comparisons are made based on this configuration and parameters.

Results for using 60 control volumes in the z-direction compared with the previous value of  $n_z=40$  and  $e_z=1.20$  are presented in Table 5.3. In this table the values of an expansion coefficient  $e_z$  do not go higher than 1.14, because for those conditions the ratio of largest to smallest control volume sizes becomes impractical. Results for the  $Nu_{avg\_exit}$  and  $u_{max\_exit}$  for 60 control volumes in the z-coordinate direction are presented in Table 5.3.

The grid independence analysis for the y-coordinate direction, using up to 60 control volumes, is summarized in Table 5.4.

As can be seen from Table 5.4 the addition of 20 control volumes in the y-coordinate direction does not impact drastically the results obtained using 40 control volumes as presented in Table 5.2.

Table 5.2 Grid independence study for the z-coordinate direction. Effects on  $e_z$ 

Grid Size: nx:ny:nz::100:40:40					
Expansion factor for x:		$e_x=1.025$			
Expansion factor for y:		$e_y=1.35$			
Expansion factor $e_z$	Smaller control volume size [m]	$Nu_{avg\_exit}$	% diff	$u_{max\_exit}$	% diff
Uniform grid	$1 \times 10^{-3}$	4.7743		0.1248	
1.04	$6.71 \times 10^{-4}$	4.5016	6.05	0.1326	5.91
1.08	$4.37 \times 10^{-4}$	4.1798	7.69	0.1324	0.11
1.10	$3.49 \times 10^{-4}$	4.0263	3.81	0.1326	0.08
1.12	$2.77 \times 10^{-4}$	3.8812	3.73	0.1326	0.0
1.14	$2.19 \times 10^{-4}$	3.7462	3.60	0.1324	0.15
1.16	$1.73 \times 10^{-4}$	3.6223	3.42	0.1323	0.07
1.18	$1.36 \times 10^{-4}$	3.5098	3.20	0.1322	0.07
<i>1.20</i>	<i><math>1.07 \times 10^{-4}</math></i>	<i>3.4085</i>	<i>2.97</i>	<i>0.1322</i>	<i>0.0</i>

Table 5.3 Grid independence study for the z-coordinate direction. Effects on the  $n_z$ 

Grid Size: nx:ny:nz::100:40:60					
Expansion factor for x:		$e_x=1.025$			
Expansion factor for y:		$e_y=1.35$			
Expansion factor $e_z$	Smaller control volume size [m]	$Nu_{avg\_exit}$	% diff	$u_{max\_exit}$	% diff
<i>Values from Table 5.2</i>	$1.07 \times 10^{-4}$	3.4085		0.1322	
1.12	$8.2873 \times 10^{-5}$	3.4772	2.27	0.1327	0.07
1.14	$5.6055 \times 10^{-5}$	3.3248	2.26	0.1326	0.07

Table 5.4 Grid independence study for the y-coordinate direction

Grid Size: nx:ny:nz::100:60:40					
Expansion factor for x:		$e_x=1.025$			
Expansion factor for z:		$e_z=1.20$			
Expansion factor $e_y$	Smaller control volume size [m]	$Nu_{avg\_exit}$	% diff	$u_{max\_exit}$	% diff
<i>Values from Table 5.2</i>	$1.07 \times 10^{-4}$	3.4085		0.1322	
1.15	$15.1 \times 10^{-5}$	3.4044	0.120	0.1322	0.0
1.25	$8.11 \times 10^{-5}$	3.4038	0.137	0.1324	0.07
1.35	$4.32 \times 10^{-5}$	3.4033	0.1525	0.1326	0.07

Table 5.5 presents the results for the grid independence on the x-coordinate direction. For this particular example the factor  $e_x$  was fixed and the numbers of control volumes in the domain were varied. The grid in this direction was no larger than 180 control volumes.

The results show that the use of 180 control volumes in the x-coordinate direction basically does not change the results using 100 control volumes. However, the use of a greater number of control volumes will allow having more points for conducting a more precise analysis of the computational results.

Table 5.5 Grid independence study for the x-coordinate direction

Grid Size: $n_x:n_y:n_z::\text{---}:40:40$						
Expansion factor for x:		$e_y=1.025$				
Expansion factor for y:		$e_y=1.35$				
Expansion factor for z:		$e_z=1.20$				
Control volumes $n_x$	Smaller control volume size [m]	$Nu_{\text{avg\_exit}}$	% diff	$u_{\text{max\_exit}}$	% diff	
<i>Values from Table 5.2</i>	$1.07 \times 10^{-4}$	3.4085		0.1322		
<i><math>n_x=100</math></i>						
180		3.4082	0.009	0.1326	0.3	
160		3.4080	0.01	0.1325	0.22	
140		3.4076	0.02	0.1323	0.07	



As a conclusion of this grid independence study, it is recommended to use up to 40 control volumes and expansion factors equal of  $e_y=1.35$  and  $e_z=1.20$ , respectively, for the y- and z-coordinate direction and if the computational resources are available to use up to 180 control volumes with an expansion factor equal to  $e_x=1.025$  for the x-coordinate direction.

Thus a grid size of  $100 \times 40 \times 40$  with  $e_x=1.025$ ,  $e_y=1.35$ , and  $e_z=1.2$  was declared to give grid independence results.

## CHAPTER VI

### PARALLEL IMPLEMENTATION

#### 6.1 Introduction

Since the time computers have been applied to solve scientific and engineering problems, their speed has increased with the needs of applications. However, fundamental technology has restricted further improvements in speed. Nevertheless, the efficiency of serial computers, measured by the cost-performance ratio, presents a sharply linear increase in performance with relatively low cost. However, beyond a particular point, even minimal improvement in the performance is accompanied by a large increase in the cost [57].

Technological advances have made it possible to construct extremely fast and low cost processors that can be connected via a network to form a parallel computer. Parallel processing offers an alternative to the limitations of serial computers.

The main idea in parallel computing is to accomplish a large computational task by dividing it into a set of small sub-tasks that are performed concurrently on multiple processors.

A detailed discussion of parallel architectures is beyond the scope of this work. This work describes an *OpenMP* based parallel implementation for the numerical solution of the *mixed convection problem over a three-dimensional horizontal backward-facing step*. The rest of this chapter includes a short theoretical description of the OpenMP, an outline of the parallel implementation, and numerical experiments on parallel computers.

## 6.2 Parallel Architecture and OpenMP

To have a better understanding of the advantages of partitioning a numerical task across multiple processors, it is worthwhile to understand the architecture of parallel computers.

### 6.2.1 Parallel Architecture

A simple and traditional model of a computer is the sequential computer, which consists of a central processing unit (CPU) and a memory unit (M). Such computers are referred to as single instruction single data stream computers (SISD) [57].

A computer's performance can be dramatically improved through the use of multiple CPUs and multiple memory units interconnected in such a way that the result is a parallel computer. Parallel computers are often described as having distributed memory or shared memory architectures [58]. Figures 6.1 and 6.2 show typical representations of distributed memory and shared memory architectures, respectively.

In the distributed memory (DMA) or private memory architecture each processor has its own exclusive memory unit and an interconnection network allows communication between processors. Parallel computers with this architecture are commonly referred to as multi-computers. On the other hand, in the shared memory architecture (SMA) all of the processors have direct access to a common shared memory address space. This kind of architecture for parallel computers is referred to as multi-processors.

Hybrid systems that combine features of both architectures are known as distributed

shared memory computers (DSM). A DSM system is similar to a distributed memory computer with additional hardware and software that provides each CPU direct access to the entire memory. Such a multi-processor behaves as a shared memory computer.

CPU requests for accessing a remote memory location are done via messages through the interconnection network. Since these remote memory accesses take longer than the local memory accesses, some memory locations seem to be farther from a CPU than others. Such a machine is defined as a non-uniform memory access (NUMA). If the time for accessing a remote memory location is no larger than the time for accessing a local one, then the computer is called a uniform memory access (UMA) [58].

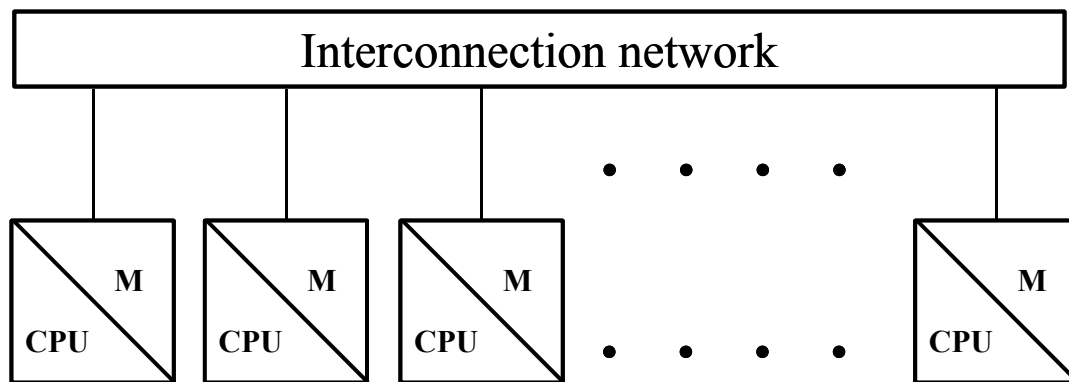


Fig. 6.1 Distributed memory architecture (DMA)

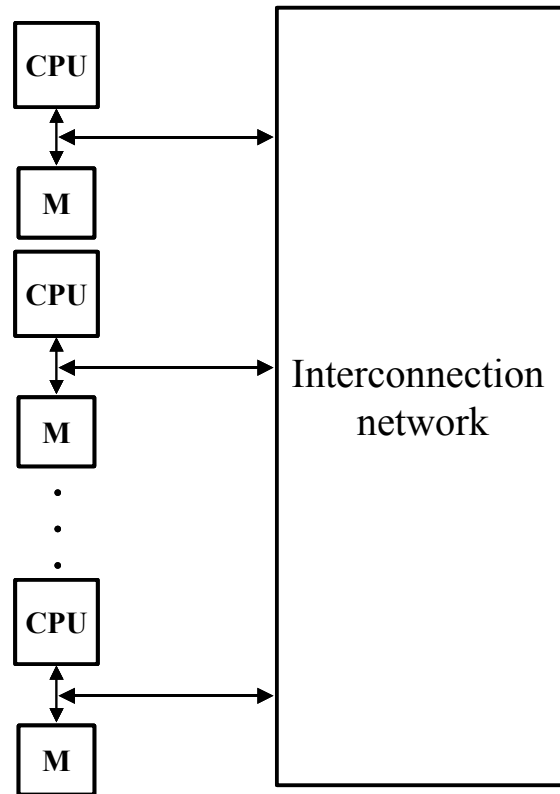


Fig. 6.2 Shared memory architecture (SMA)

The parallel computers used in this research belong to the DSM class of systems. Some of them have a non-uniform memory access (NUMA) but some of them utilize a uniform memory access (UMA).

### 6.2.2 *OpenMP*

OpenMP is a parallel programming model for SMA and DSM systems [59] that was established in 1997 through a combined effort between hardware vendors and compiler developers. OpenMP is considered a software standard for parallel applications.

OpenMP specifies a set of compiler directives, library routines, and environment variables that can be used for parallel FORTRAN and C/C++ applications.

The advantage of allowing OpenMP to be specified by a set of directives embedded within the program is that the same base code can be compiled using a single processor or multiple processors. In the first case, the OpenMP directives are treated as comments and are ignored by the compiler, leading to a serial execution. On parallel platforms these commands result in the creation of threads that allow concurrent execution [59].

The application-programming interface (API) for OpenMP is divided into three parts: [59]

- i) Directive-based language
- ii) Runtime library subroutines
- iii) Environment variables

Parts ii) and iii) are designed to control the execution parameters and to set up the conditions for the parallel applications, while part i) is the one used for defining and limiting the parallel zones, for establishing the communication between processor/memory as well as coordinating the synchronization of multiple threads. Figure 6.3 shows a schematic diagram for the API structure.

When a parallel program written with OpenMP directives finds a control structure (Fig 6.3) for expressing parallelism (*OpenMP sentinels*), the flow structure of the program is altered such that the master thread (*serial execution*) creates a group of multiple threads of execution that work concurrently on the given task. This execution model for OpenMP is known as a fork-join model [59] and is illustrated in Figure 6.4.

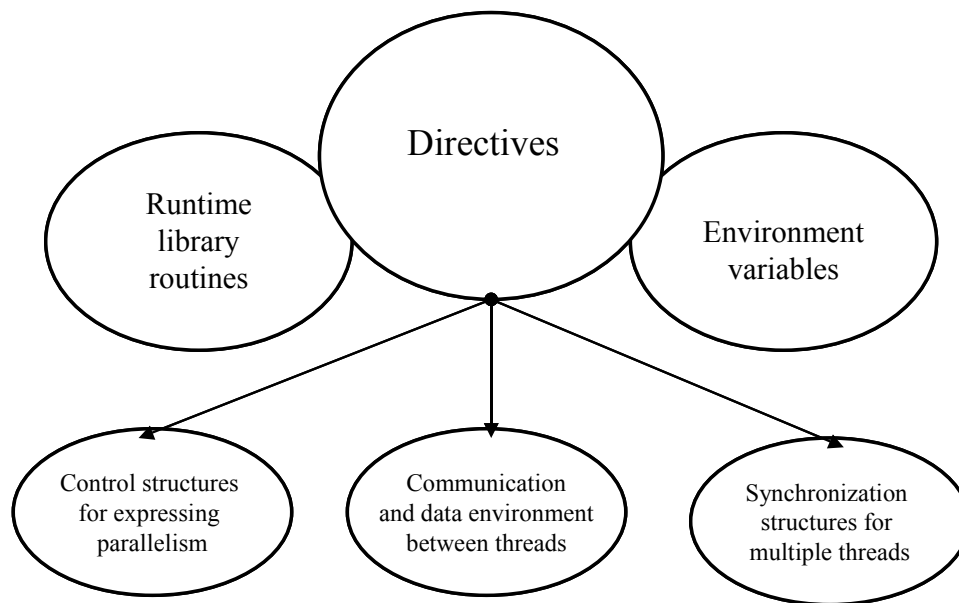


Fig. 6.3 Application-programming interface for OpenMP

When multiple threads attempt to read and write to the same memory location, the results can be different from that of a serial execution. OpenMP allows a variable to be considered private to each thread so that the writing operations for this variable are exclusive to that thread. Each thread has its own private copy of this variable and does exclusive updates to the value for the duration of the parallel construct. In contrast, a shared variable has a single memory location, which is accessible to all threads for reading and writing.

The synchronization structures (Fig. 6.3) can be used to coordinate the read-write operations for shared variables across multiple threads. These constructs are also responsible for ensuring the occurrence of an event across all threads, e.g., the start and suspension of a parallel region. In this sense each thread is guaranteed to complete its

work at the barrier placed at the end of a parallel region.

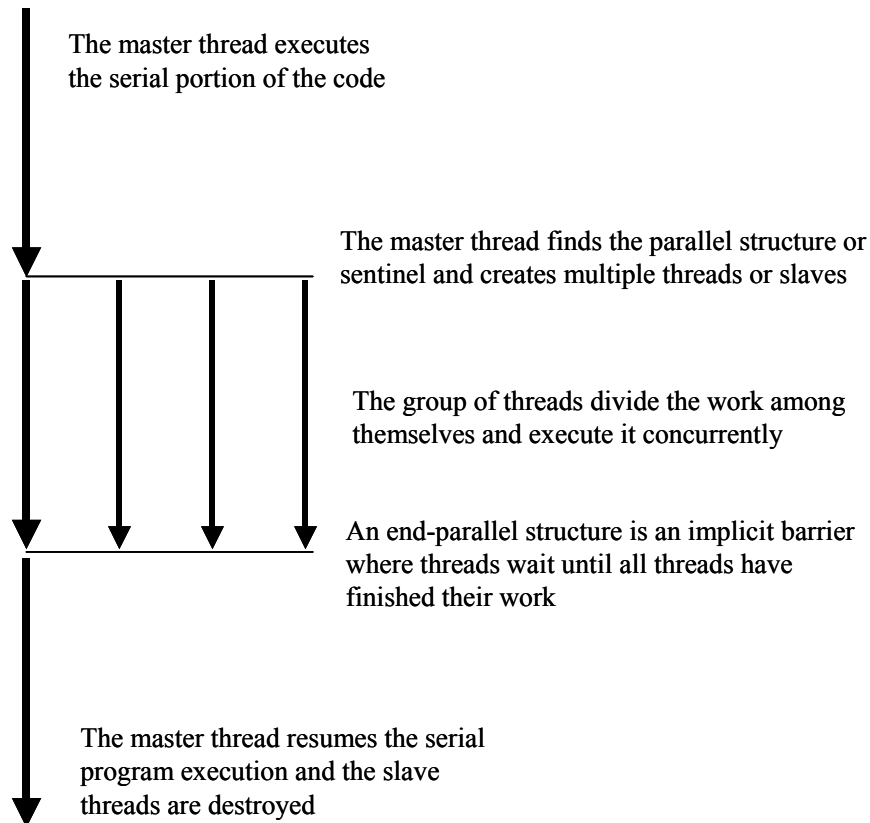


Fig. 6.4 Fork-join model execution for OpenMP

### 6.2.3 Parallel Computing Performance Measurement

The benefits achieved by parallel implementation over a serial execution are measured by the speedup [57]. *Speedup* is defined as the ratio of the time taken to solve the problem on a single process to the time taken to solve the problem on a parallel



computer with identical processors. Speedup is computed by Eq (6.1).

$$S = \frac{t_1}{t_p} \quad (6.1)$$

Where  $t_1$  is the time taken in a single processor and  $t_p$  is the time in a parallel implementation.

Theoretically, speedup should be equal to the number of processors used on the parallel computer (CPUs). However, due to the time spent in communication between multiple processors, speedup is generally less. Linear speedup is achieved when  $S=P$  for a P-processor system. One can get super linear speedup due to cache effects if parameter  $S$  is larger than  $P$

When speedup reaches an asymptotic value, the use of additional processors will not reduce the computation time.

Another parameter useful to measure the parallel performance is the *efficiency* [57]. Efficiency is defined as the ratio of speedup ( $S$ ) to the number of processors ( $P$ ). Efficiency represents the average fraction of time for which a processor is doing useful computation. A linear speedup implies an efficiency of 1.

$$E = \frac{S}{P} \quad (6.2)$$

The *cost* of solving a problem on a multiprocessor is defined as the product of the parallel runtime ( $t_p$ ) and the number of processors ( $P$ ) used. Cost should be comparable to the execution time on a single processor [57].

$$Cost = Pt_p \quad (6.3)$$

### 6.3 Parallel Implementation

One of the objectives of this research is to develop a FORTRAN code to numerically simulate the mixed convective flow over a three-dimensional horizontal backward-facing step using the finite volume discretization technique and the SIMPLE algorithm. A flow chart for this code is presented in Figure 6.5.

The first three rectangles in the flow chart in Figure 6.5 are designated to initialize the computational parameters, the boundary conditions, the grid generation, and the physical properties of the solid and liquid region within the computational domain. This stage consumes a small fraction of the total time, and therefore no extra discussion is needed in this respect.

The remaining blocks in Figure 6.5 are the most time consuming part of the computational process. In this part, the values for the three velocity components ( $u$ ,  $v$ , and  $w$ ), and the values for the pressure and temperature distributions are iteratively computed.

As was established in Chapter V, the nodal discretization for a three-dimensional geometry can be considered as a grid of nodal points (nodes) distributed along each coordinate direction. The nodes represent the points where the variables will be computed. The variables can be seen as a three-dimensional array that matches the grid [60].

According to the finite volume discretization technique discussed in Chapter IV, the governing equations give an algebraic relation between a node and its neighbors. These algebraic relations represent a balance between the nodal point and its neighbors.

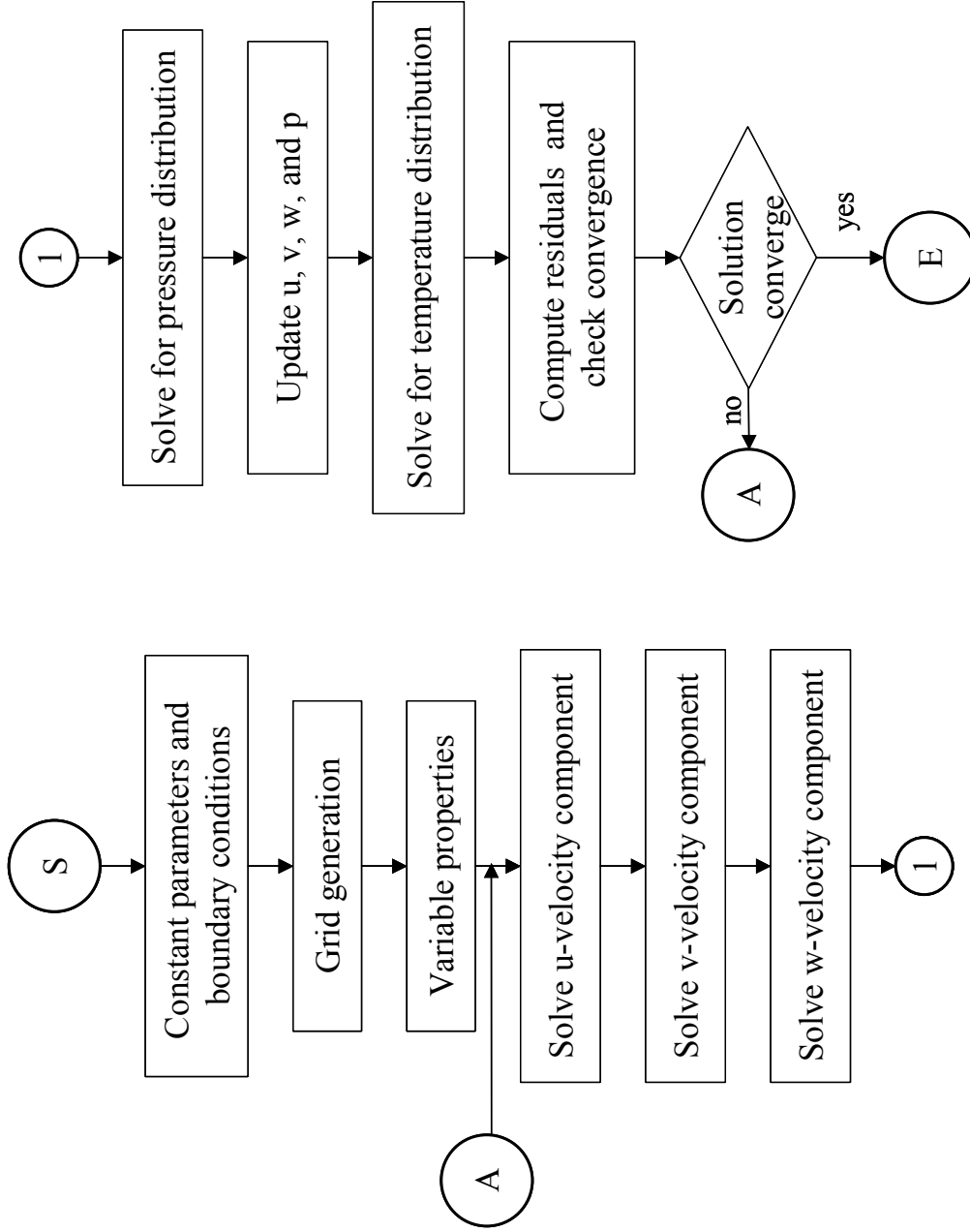


Fig. 6.5 Flow chart for the numerical code

The interaction between nodes is linked by the  $\alpha$ 's coefficients as expressed in Eqns. (4.13-4.19).

Each node needs at least seven coefficients to express each one of the governing equations. There are five governing equations that need to be solved simultaneously for the mixed convective problem. In addition, the iterative method is needed to resolve the non-linearity of the momentum equations. Therefore, it is necessary to use a parallel computer to handle the problem.

Each iteration consists of nested do-loops to update the variables in 3-dimensional arrays. These do-loops are executed concurrently across multiple processors. The loop-level parallelism features offered by OpenMP will be exploited to parallelize the code.

The uniform 3-dimensional grid allows ordering of nodes in a variety of different ways. For example, the grid can be seen as a collection of planes along a coordinate direction. Within each plane nodes can be grouped to form lines along the other two coordinate directions. This concept is graphically demonstrated in Figure 6.6 for planes in the x-coordinate direction.

The nodes in the three-dimensional array are identified by the subscripts (k, j, i) that represent each one of the coordinate direction (z, y, x), respectively. According to Figure 1.1 the z, y, and x coordinates represent the span-wise, the transversal, and the stream-wise direction of the flow, respectively.

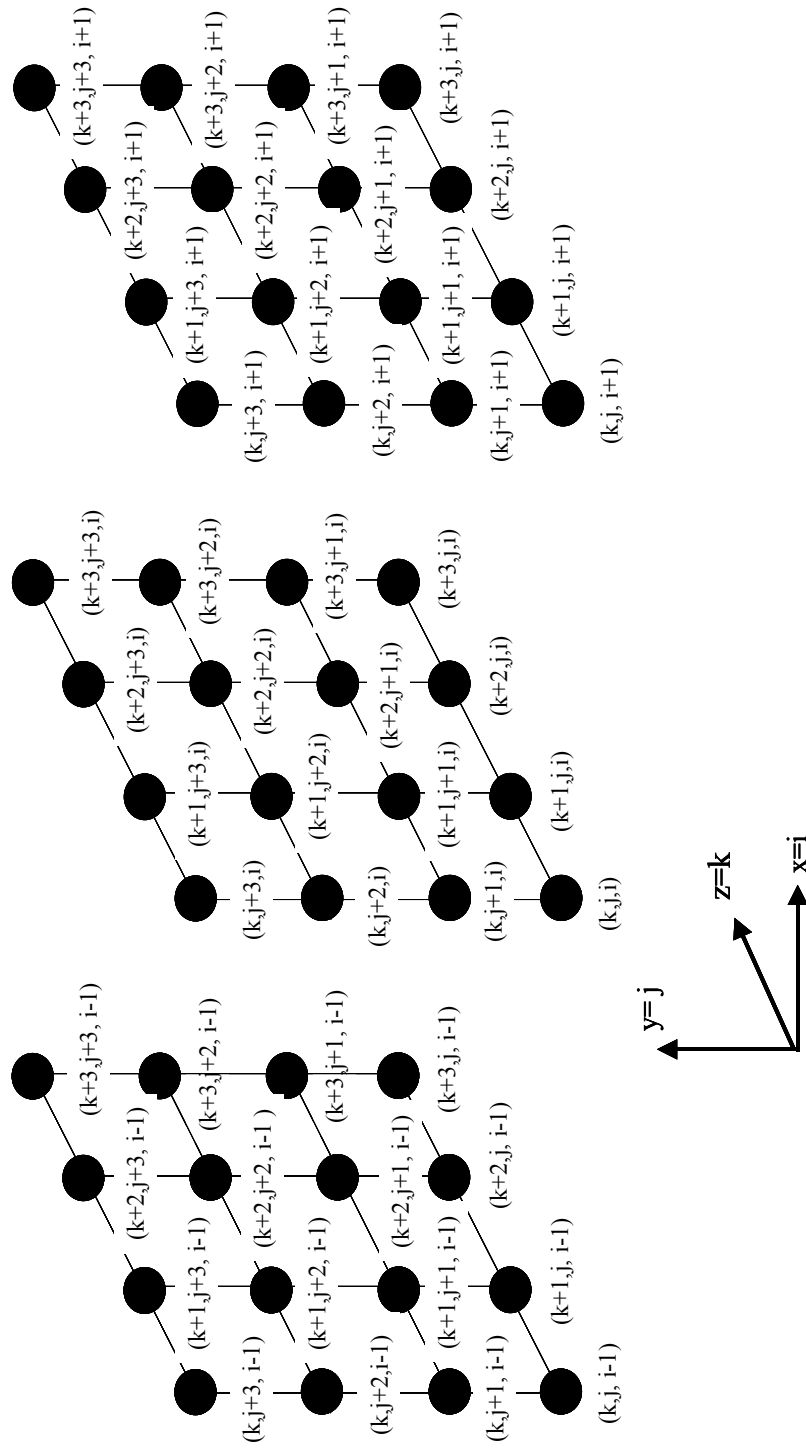


Fig. 6.6 Collection of planes for the three-dimensional computational domain in the stream-wise direction

From Figure 6.6 it is evident that within a plane the nodes having the same “j-index” represent a line (*group of nodes*) parallel to the z-coordinate direction. Similarly the nodes with the same “k-index” represent a line parallel to the “y-direction”.

Since each node represents an algebraic equation, it is obvious that each group of nodes (*line*) represents an algebraic system of equations. The associated linear system of equations is tri-diagonal, and can be easily solved by means of the TDMA algorithm as discussed in Chapter IV. In this manner, the three-dimensional problem is reduced to a two-dimensional problem defined on planes along the x-coordinate. These two-dimensional problems are simplified to a one-dimensional problem defined on the lines of nodes along the z-direction.

Under this assumption the three-dimensional numerical procedure for each variable can be solved plane by plane in a line-by-line fashion. The procedure for any i-esimo can be understood as keeping the “k-index” constant and solve line-by-line from  $k=1$  to  $k=k_{\text{maximum}}$  (swept front to back) then keeping the “j-index” constant, solve line-by-line from  $j=1$  to  $j=j_{\text{maximum}}$  (swept bottom to top). Hence solving the complete domain for  $u$ ,  $v$ ,  $w$ ,  $p$ , and  $T$  will depend on the number of lines in the z-coordinate direction ( $k=1$  to  $k_{\text{maximum}}$ ), the number of lines in the y-coordinate direction ( $j=1$  to  $j_{\text{maximum}}$ ) and on the number of planes in the x-coordinate direction ( $i=1$  to  $i_{\text{maximum}}$ ).

The parallel strategy proposed in this research consists of splitting the computational domain into planes normal to the x-axis, and then by means of OpenMP, evenly assigning blocks of these planes to each processor. This concept is schematically

presented in Figure 6.7. Thus, the parallel implementation consists in splitting the three-dimensional computational domain into blocks of  $i$ -planes and assigning them to threads. The numerical procedure for each plane is computing the  $\alpha$ 's coefficients for each node by varying the "k-index" and keeping the "j-index" constant and storing the values in a tri-diagonal matrix. Once the coefficients for the last k-index are computed and stored, the tri-diagonal matrix is solved by means of the TDMA algorithm. This procedure is repeated for line  $j=1$  to the line  $j=j_{\text{maximum}}$ . The procedure is repeated for lines that are formed by keeping the "k-index" constant and the  $\alpha$ 's coefficients are computed for each "j-index" node. In this sense each node is sweeping bottom to top and front to back. This parallel scheme is used to update the  $u$ -variable, and the  $v$ ,  $w$ ,  $p$ , and  $T$  variables according to the flow diagram in Figure 6.5.

#### **6.4 Parallel Performance**

The performance of the parallel code was studied on two parallel computers: a 32-processor IBM-p690 at the Texas A&M Supercomputer center (AGAVE) and an IBM-p690 at NCSA at the University of Illinois (COPPER). The experiments were conducted on 4 processors of AGAVE, and 16 processors on COPPER (administrative policies restricted the use of AGAVE to a maximum of 4-processors per job and a maximum of 16-processors per job on COPPER).

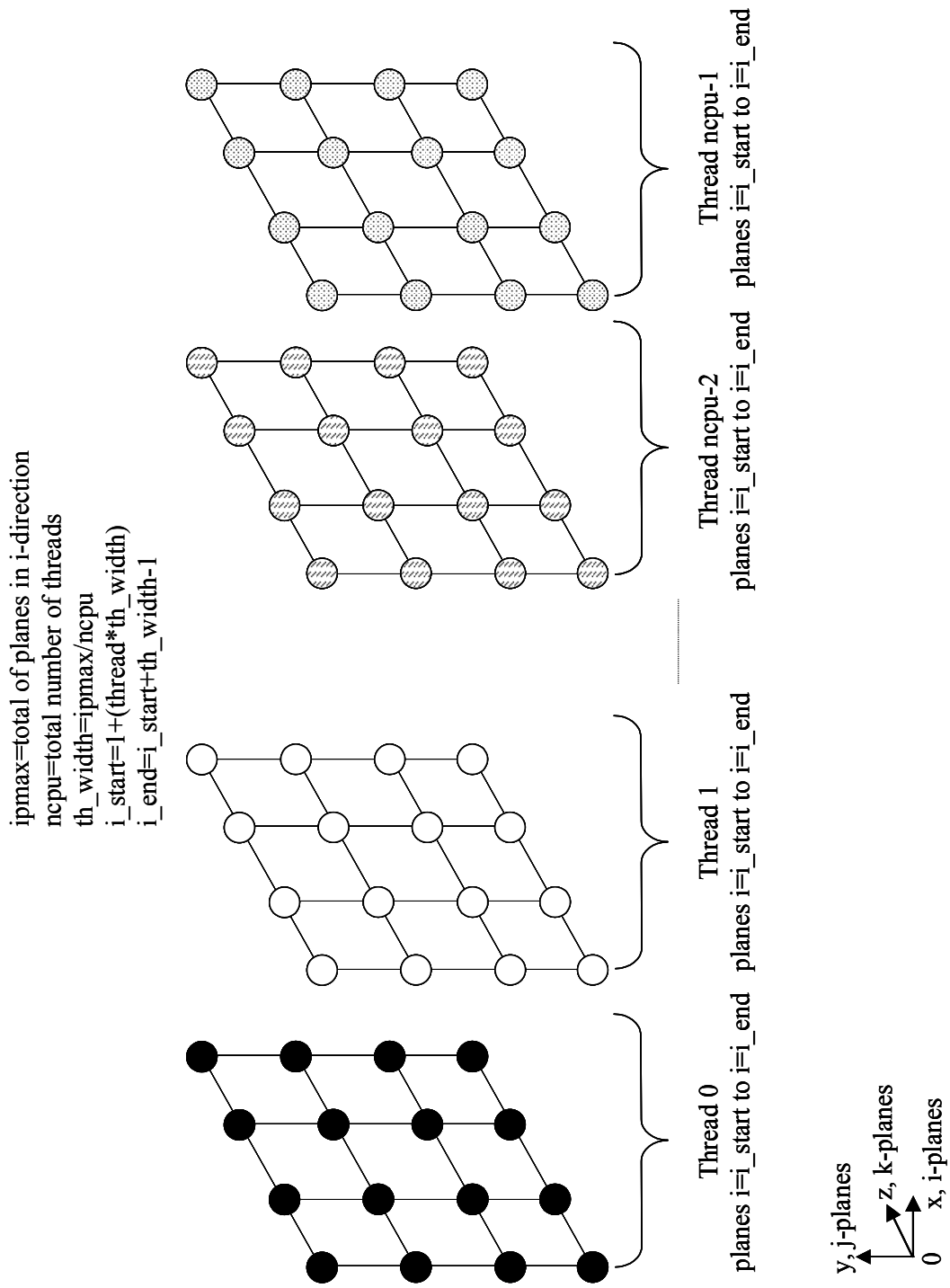


Fig. 6.7 Distribution of i-planes for an OpenMP parallel implementation



Several cases were tested for different grid sizes and for simulating different fluid-flow parameters. Initial studies were conducted for a few hundred iterations in order to test the performance of the parallel implementation. At the end of this section, results for simulating the complete solution of the problem are presented.

The first test case is that for simulating a mixed convective flow with  $Ri=1$ , a grid size of  $180:40:40::x:y:z$ , and a thermal conductivity ratio solid/fluid equal to  $k_s/k_f=k_{Cu}/k_{air}$  (Cu: Copper). This test was done on AGAVE and was simulated for a maximum of 5000 iterations. The results are presented in Table 6.1 and the total time, the speedup, and efficiency are plotted as a function of the number processors (P) in Figure 6.8, Figure 6.9, and Figure 6.10, respectively. The results for this example showed that a reasonable speedup is obtained. In general it can be seen that when using 2 processors a linear speedup is obtained, but for 4 processors the speedup is smaller than 4. In the same sense, a better efficiency is found for 2 processors than for 4 processors.

Table 6.1 Parallel performance, test 1 on AGAVE 5000 iterations

Grid 180:40:40/Ri=1-Mixed convection/ $k_s/k_f=k_{Cu}/k_{air}$			
	Number of processors (P)		
	1	2	4
CPU computing time [s]	3861	1935	1099
Speedup	1	1.99	3.51
Efficiency	100	99.76	87.82

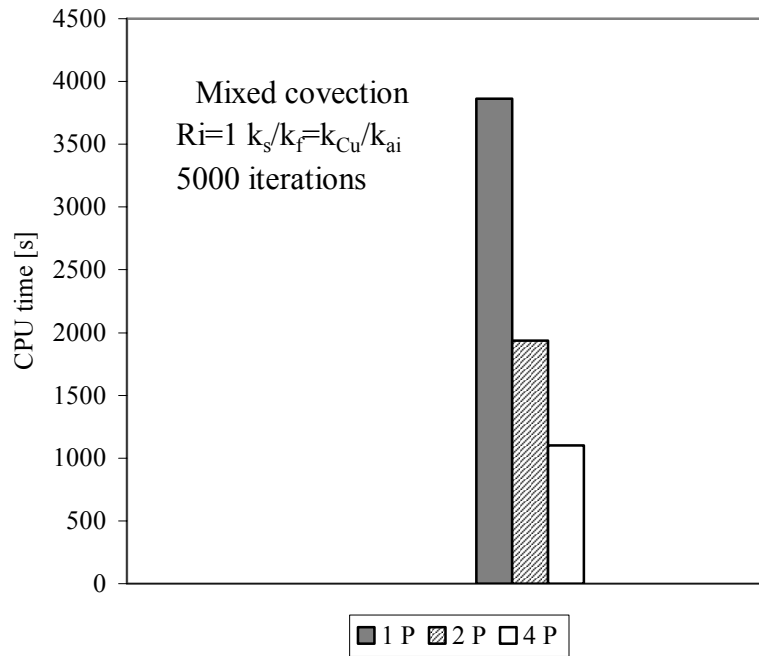


Fig. 6.8 Total time for test 1 on AGAVE

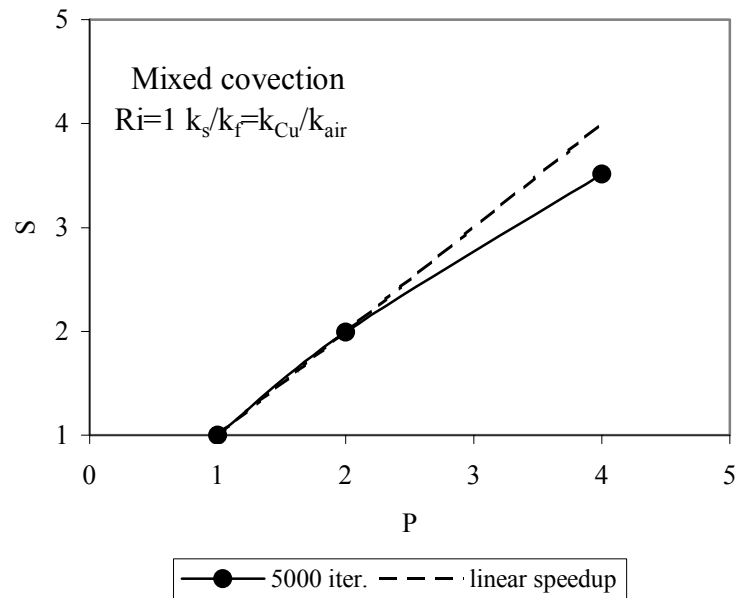


Fig. 6.9 Speedup vs. P test 1 on AGAVE

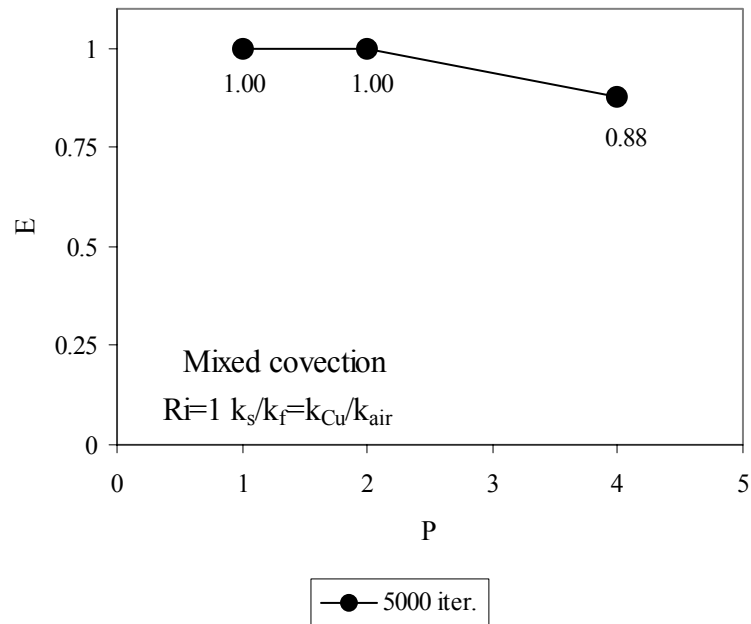


Fig. 6.10 Efficiency vs. P test 1 on AGAVE

The next test was done on COPPER. In this case, the maximum number of iterations was fixed to 5000, and the thermal conductivity solid/fluid ratio was fixed to  $k_{Cu}/k_{air}$ . In these cases different grid sizes were proposed and the results of computing time and speedup are presented in Table 6.2. Figures 6.11 and 6.12 show the speedup and efficiency of the parallel code for different sized meshes.

It can be observed from Figure 6.11 that the speedup is almost linear, and in many cases super linear. Figure 6.12 shows a better efficiency for larger grid sizes (180:40:60) than for small grid sizes (100:40:40). The super linear speedup is obtained for larger mesh sizes because the tri-diagonal solver is able to exploit the cache very effectively.

Table 6.2 Parallel performance, test 2 on COPPER

Grid size x:y:z	Maximum of iterations 5000/Ri=3-Mixed convection/ $k_s/k_f=k_{Cu}/k_{air}$				
	Total computing time [s]/(speedup)				
	1 P	2 P	4 P	8 P	16 P
100:40:40	1707/(1)	870/(1.96)	422/(4.04)	211/(8.09)	112/(15.20)
140:40:40	2526/(1)	1237/(2.04)	615/(4.10)	296/(8.53)	155/(16.29)
180:40:40	3746/(1)	1827/(2.05)	902/(4.15)	436/(8.60)	224/(16.72)
180:40:60	6112/(1)	2970/(2.06)	1470/(4.16)	693/(8.81)	347/(17.61)

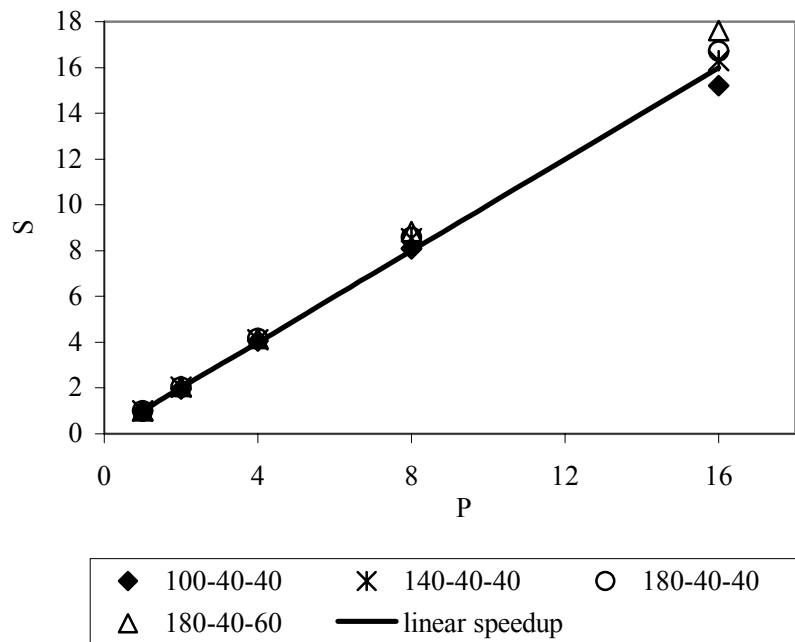


Fig. 6.11 Speedup for different grid size test 2 on COPPER

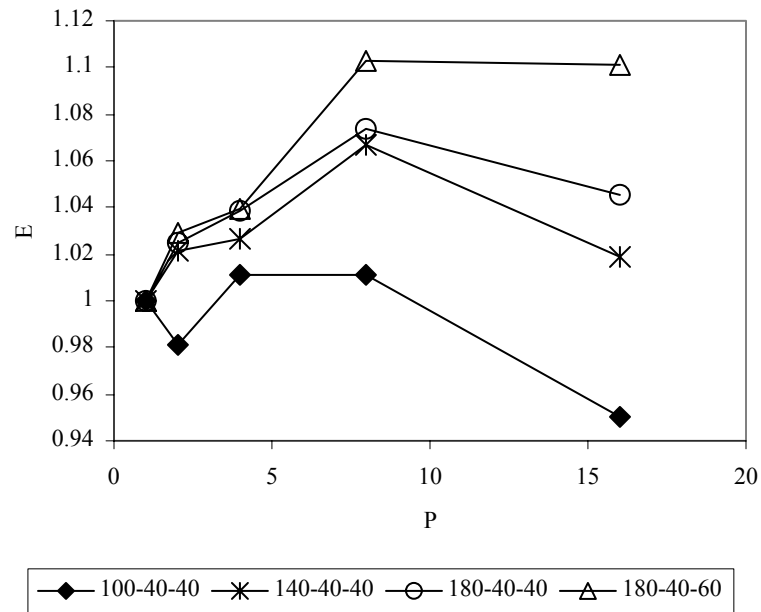


Fig. 6.12 Efficiency for different grid size test 2 on COPPER

The effect is more pronounced as  $P$  is increased because the sub-problems on each processor reduce in size. Furthermore, as the grid sizes increase the computation to communication ratio reduces, leading to higher efficiency.

These previous observations hold when different values of  $R_i$  are used.

The accuracy of the solution by partitioning the overall task between several processors is not affected. The difference between the solution using one processor or more processors is negligible (see Table 6.3).

Table 6.3 Differences for the computed values

Grid x:y:z::140:40:40/Mixed convection/ $k_s/k_f=k_{Cu}/k_{air}$			
	1 P	2 P	4 P
$U_{max}$ at the exit [m/s]	0.132396	0.132393	0.132394
$Nu_{avg}$ at the exit	3.407052	3.407054	3.407054
$\dot{m}_{inlet} / \dot{m}_{exit}$	0.999998	0.999998	0.999998

The previous experiments considered small problems to analyze the performance of the based OpenMP parallel implementation. The following test was done to analyze the behavior of full execution of the code.

In the following test 3 on COPPER, the grid was set as x:y:z::180:40:40 and the study case was that for a mixed convective flow with  $Ri=3$  and the thermal conductivity ratio was  $k_s/k_f=k_{Cu}/k_{air}$ . In this run, the results for running the program for one, eight and sixteen processor are summarized in Table 6.4 and Figure 6.13.

Table 6.4 shows that 1573s (approx. 26 m) were needed for convergence using 16 processors, while 29214s (approx. 8h 7m) were required to solve the problem using 1 processor. The computing time is dramatically reduced as the number of processors used to solve the problem is increased. Even for 8 processors the savings in total time is considerable. An 8 processors execution takes 3534s (approx. 1h). The total number of iterations required for the code was 36000.

Table 6.4 CPU computing time and speedup, test 3 on COPPER

Grid x:y:z::180:40:40/Mixed convection/ $k_s/k_f=k_{Cu}/k_{air}$					
	1 P	2 P	4 P	8 P	16 P
CPU consuming time [s]	29214	14550	7189	3534	1573
S	1	2.086	4.06	8.26	18.57
E	1.00	1.004	1.015	1.03	1.16

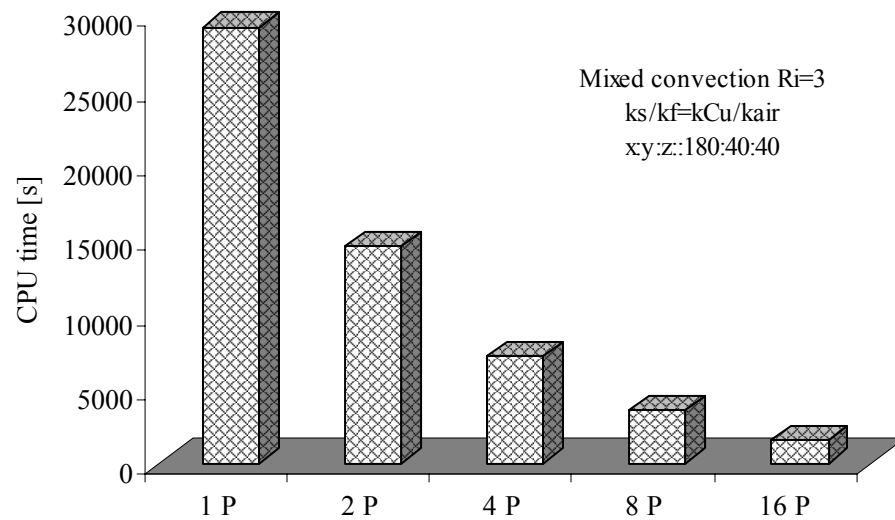


Fig. 6.13 CPU computing time for a full run, test 3 on COPPER

In this Chapter, the parallel performance of the OpenMP based implementation to solve the mixed convective flow and the forced convective flow over a three-dimensional horizontal backward facing step was presented.

Most of the study cases showed that the computing time is considerably reduced when several processors are used to run a given task. A linear speedup is obtained up to 16 processors, in many cases super linear speedup is obtained due to efficient cache utilization.



## CHAPTER VII

### RESULTS AND DISCUSSION

#### 7.1 Introduction

This chapter is designated to present the numerical results for the study of *mixed convective flow over a three-dimensional horizontal backward-facing step*. Prior to that, descriptions of the geometry, the boundary conditions, and other relevant aspects implemented in the numerical code are briefly highlighted.

The geometry in question is shown in Figure 1.1. The channel dimensions are fixed in relation to the step height ( $s=0.01\text{m}$ ) such that the expansion ratio (ER) and aspect ratio (AR) are equal to 2 and 4, respectively. The total length of the channel in the stream-wise direction is equal to 52 times the step height and the step length is equal to 2 times the step height.

The geometrical proportions for the step were fixed according to the definition of the benchmark problem established by the ASME K-12 Aerospace Heat Transfer Committee [12]. Similarly, the total length and channel expansion ratio were chosen based on values reported in the literature [17, 19-20] for flow over a backward-facing step channel. The aspect ratio was selected as four, in order to impose a stronger three-dimensional behavior in the flow.

In the following section a global description of the adopted numerical procedure is presented and a detailed explanation for the boundary conditions in the computational domain is given.

## 7.2 Numerical Procedure and Boundary Conditions

The flow through the geometry was assumed to be steady and the Boussinesq approximation was invoked to confine the variations of density in the buoyancy term. Based on these assumptions a FORTRAN code was developed to numerically study the mixed convective flow over a three-dimensional horizontal backward-facing step. Thus, the momentum and the energy equations were discretized by means of a finite volume technique and the SIMPLE algorithm was used to link the pressure and velocity fields. Solution to the one-dimensional convection-diffusion equation at the control volume interface was represented by the Power Law scheme, as previously discussed in Chapter IV.

Velocity nodes were placed at staggered locations in each coordinate direction while pressure, temperature, and other scalar properties were evaluated at the main grid points. A non-uniform grid size was considered to solve the problem as described in Chapter V.

At the channel entrance the flow is considered as a three-dimensional fully developed flow [53] with a parabolic profile and at constant temperature. No slip conditions were applied at the channel walls including those along the backward-facing step.

The channel walls were treated as adiabatic, excluding the bottom wall, which was subjected in its totality ( $0 \leq x \leq L$ ,  $0 \leq z \leq W$ ) to a constant high temperature ( $T_w$ ). No jump temperature condition was applied at this specific boundary. At the channel exit the natural outflow boundary conditions were implemented.

To simulate the channel backward-facing step inside the computational domain a

very high diffusion coefficient for the momentum equation was chosen ( $\mu=1 \times 10^{50}$ ) [46], and for the energy equation, the thermal diffusion coefficient was set equal to a thermal conductivity  $k_s$  of the solid. In this sense the backward-facing step was considered as a conducting block and its impact on the flow was analyzed.

At the solid-fluid interface (around the backward-facing step) the diffusion coefficients were evaluated by a weighted harmonic mean of the properties in the neighboring control volumes as proposed by Patankar [46], while the conjugate problem of conduction-convection at the solid-fluid interface was solved by a pseudo-solid-specific heat method, as suggested by Xi and Han [61].

The working fluid is air and the physical properties were treated as constants and evaluated at the inlet flow temperature  $T_0=293$  K, as  $\rho=1.205$  kg/m<sup>3</sup>,  $\mu=1.81 \times 10^{-5}$  kg/m-s,  $C_p=1005$  J/kg-K,  $k_f=0.0259$  W/m-K and  $\beta=0.00341$  K<sup>-1</sup>.

The numerical study presented in this research considers a mixed convective airflow over a three-dimensional horizontal backward-facing step for three different Richardson numbers ( $Ri=1, 2, \text{ and } 3$ ). Variations in the buoyancy effects were accomplished by varying the imposed temperature along the bottom wall ( $T_w$ ), which in turn modifies the Grashof ( $Gr$ ) number and thus the  $Ri$ .

All numerical experiments were conducted for a Reynolds number equal to  $Re=200$ . The Reynolds number is defined in terms of the mean flow velocity at the channel inlet ( $U_0$ ) and the channel height.

According to the mixed convection theory if the  $Ri$  parameter increases, the free convective effects are dominant over the forced convective effects in the flow and vice

versa. In this sense the impact on the flow for imposing different buoyancy forces are compared with the pure forced convective flow, as will be shown in Section 7.5. The studies on the impact of the conducting block on the flow field are properly presented and analyzed in the Section 7.6. Section 7.3 is designated to explain the convergence criteria concepts imposed on the numerical code.

### 7.3 Convergence Criteria

Since an iterative solution procedure following the discretization procedure was adopted for handling the non-linearity in the momentum equations and for solving the linkage between the momentum and the energy equations, it is necessary to define a convergence stop criteria for terminating the iterative scheme.

A common procedure in computational fluid dynamics is to declare convergence when the so-called residuals for the velocity ( $R_u$ ,  $R_v$ ,  $R_w$ ), and for the pressure ( $R_p$ ) are less than an extremely small number epsilon ( $\varepsilon$ ). The definitions [62] for the convergence criteria for the velocity components ( $\phi$ ) are presented in Eq. (7.1) and for pressure in Eq. (7.2).

$$R_\phi = \frac{\sum_{nodes} |a_p \phi_p| - [\sum |a_{nb} \phi_{nb}| - A(p_\phi - p_{\phi+1}) - b]_{nodes}}{\sum_{nodes} |a_p \phi_p|} \leq \varepsilon_\phi \quad (7.1)$$

$$R_p = \sum_{nodes} \left| \rho [A_{y-z}(u_w - u_e) + A_{x-z}(v_s - v_n) + A_{x-y}(w_b - w_t)] \right| \leq \varepsilon_p \quad (7.2)$$

In Eq. (7.1)  $\phi$  represents the u, v, and w velocity components and the  $\mathbf{a}$  coefficients were defined in Chapter IV.

For the temperature field the convergence criterion used was the absolute maximum relative difference in temperatures between successive iterations to be less than  $\varepsilon_T$  [49].

$$R_T = \left( \left| \frac{T_{k,j,i}^{n+1} - T_{k,j,i}^n}{T_{k,j,i}^{n+1}} \right| \right) \leq \varepsilon_T \quad (7.3)$$

Here, the indices represent each node in the computational domain and the  $n$  represents the iteration number.

For this research, the convergence parameters were fixed as  $\varepsilon_\phi=10^{-8}$ ,  $\varepsilon_p=10^{-10}$ , and  $\varepsilon_T=10^{-6}$  for velocity components, pressure, and temperature, respectively.

Prior to discussing results, some physical parameters and quantities of interest are defined in Section 7.4.

#### 7.4 Physical Parameters and Definitions

One parameter that is inherent in the flow over a backward-facing step is the distance from the step that the flow takes to be reattached. This dimension has been called the reattachment point for two-dimensional geometries and is identified as the point where the shear stress is equal to zero. However, for a three-dimensional geometry this parameter is no longer a point, but is a line along the span-wise direction. This line is called the  $x_u$ -reattachment line or simply the  $x_u$ -line and is identified, as the points along the span-wise direction where the stream-wise component of the wall shear stress is equal to zero. For numerical purposes these points are identified as the distance from the backward-facing step where the  $u$ -velocity component becomes equal to zero [17, 19-20].

Another parameter that will be useful to present the pertinent results for this research is the stream-wise wall shear stress averaged along the span-wise direction. From here on this parameter will be called the averaged shear stress  $\tau_{wx}$  and it is defined as:

$$\tau_{wx} = \mu \left( \frac{d\bar{u}}{dy} \right) \Big|_{y=0} \quad (7.4)$$

The definition for the local Nusselt number is given as:

$$Nu = \frac{\left( \frac{dT}{dy} \right) \Big|_{y=0} 2H}{(T_w - T_b)} \quad (7.5)$$

In Eq. (7.2) the term  $2H$  is the channel height and  $T_b$  is the bulk temperature. The definition for the bulk temperature  $T_b$  was taken from Shah and London [53] as:

$$T_b = \frac{1}{Au_b} \int_A uT dA \quad (7.6)$$

Here the  $u_b$  is the mean velocity (*bulk velocity*) and  $A$  represents the cross sectional area of the channel.  $T$  and  $u$  represent the components of the temperature and stream-wise velocity fields.

$$u_b = \frac{1}{A} \int_A u dA \quad (7.7)$$

If the local Nusselt number is averaged along the span-wise direction, then what is obtained is the averaged span-wise Nusselt number ( $Nu_{avg}$ ) defined as:

$$Nu_{avg} = \frac{\left( \frac{d\bar{T}}{dy} \right) \Big|_{y=0} 2H}{(\bar{T}_w - T_b)} \quad (7.8)$$

The averaged span-wise Nusselt number ( $Nu_{avg}$ ) will be denoted as the averaged Nusselt number from here on.

Now that the physical parameters for studying the mixed convective flow have been defined, and a global review of the theory, beyond the numerical implementation has been presented, the following section is designed to present the pertinent results achieved in this research.

### **7.5 Effects of Varying the Richardson Number**

As was presented in Chapters I and II, the flow over the backward-facing step is extremely sensitive to the abrupt geometrical change at the step. Downstream of the step and just behind the primary re-circulation zone, the flow is reattached and redevelops to a fully developed flow at the channel exit. However, in the scenario previously described the buoyancy forces due to the presence of temperature gradients was not considered. Under such circumstances the flow behavior could be completely distorted.

Hence, the main focus of this section is to analyze the effects of a mixed convective flow over a three-dimensional horizontal backward-facing step. In order to study the mixed convective effects, parameters like the  $x_u$ -line, the averaged shear stress  $\tau_{wx}$ , the averaged Nusselt number, and velocity and temperature profiles at specific planes will be examined for different Ri values and for pure forced convective flow. Results for three different Ri parameters (Ri=3, 2, and 1) were compared against the pure forced convective flow (Ri=0). The thermal conductivity of the block was fixed at a constant value corresponding to that for Copper ( $k_s=386$  W/m-K).

### ***7.5.1 The $x_u$ -line, Averaged Nusselt Number, and Averaged Shear Stress***

For pure forced convective flow ( $Ri=0$ ) the presence of the step results in a primary re-circulation zone that is limited by the so-called  $x_u$ -line. The impact of varying Richardson in the  $x_u$ -line is plotted in Figure 7.1.

As can be seen in Figure 7.1, the  $x_u$ -line is symmetric in the span-wise direction due to the symmetry in the geometry and the boundary conditions. As the value of  $Ri$  is increased to 1 the  $x_u$ -line is pushed farther downstream. However, an increase in  $Ri$  to 2 and 3 the  $x_u$ -line shifts upstream. This behavior can be explained by examining the stream trace plots presented in Figures 7.2–7.5.

From Figure 7.2 it is evident that for pure forced convective flow ( $Ri=0$ ) there are no cross-stream (stream-wise) re-circulation currents. As the  $Ri$  value is increased to 1, the mixed convective effects come into play and push the primary re-circulation zone farther downstream (Figure 7.3).

Also, it is evident from Figure 7.3 that the cross-stream components of velocity are minimal for  $Ri=1$ . As  $Ri$  is increased to 2 and 3 it is evident from Figures 7.4 and 7.5 that strong cross-stream or span-wise re-circulation zones appear which in turn suppress the primary re-circulation zone which leads to movement of the  $x_u$ -line farther upstream of that for pure forced convection ( $Ri=0$ ).



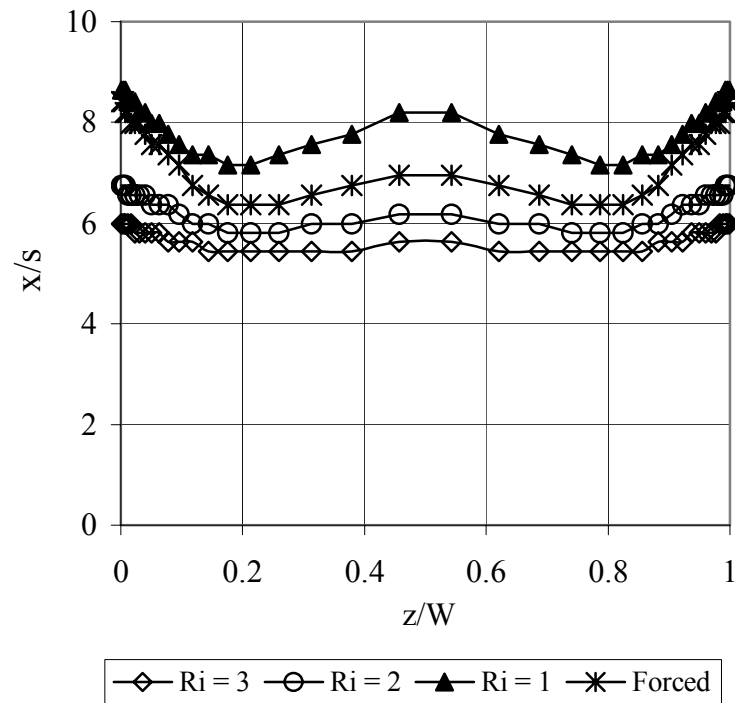


Fig. 7.1  $x_u$ -line distribution for different Ri and for pure forced convection

From Figure 7.1 it can be seen that for  $Ri=0$  and  $Ri=1$  the  $x_u$ -line resembles a “W” shape with two local minimum near each of the sidewalls and a maximum along the span-wise central plane.

For  $Ri=0$  and 1 the magnitudes of the  $v$  and  $w$  components are relatively small near the walls and leads to larger  $u$ -velocity components to satisfy the mass conservation. Thus the  $x_u$ -line values are larger near the sidewalls. The magnitude of  $v$  and  $w$  velocity components increase between the span-wise central plane and the sidewalls for  $Ri=2$  and

3 (as discussed later in Section 7.5.2). To satisfy continuity the magnitude of  $u$ -velocity decreases (as discussed later in Section 7.5.2) which results in two local minimums.

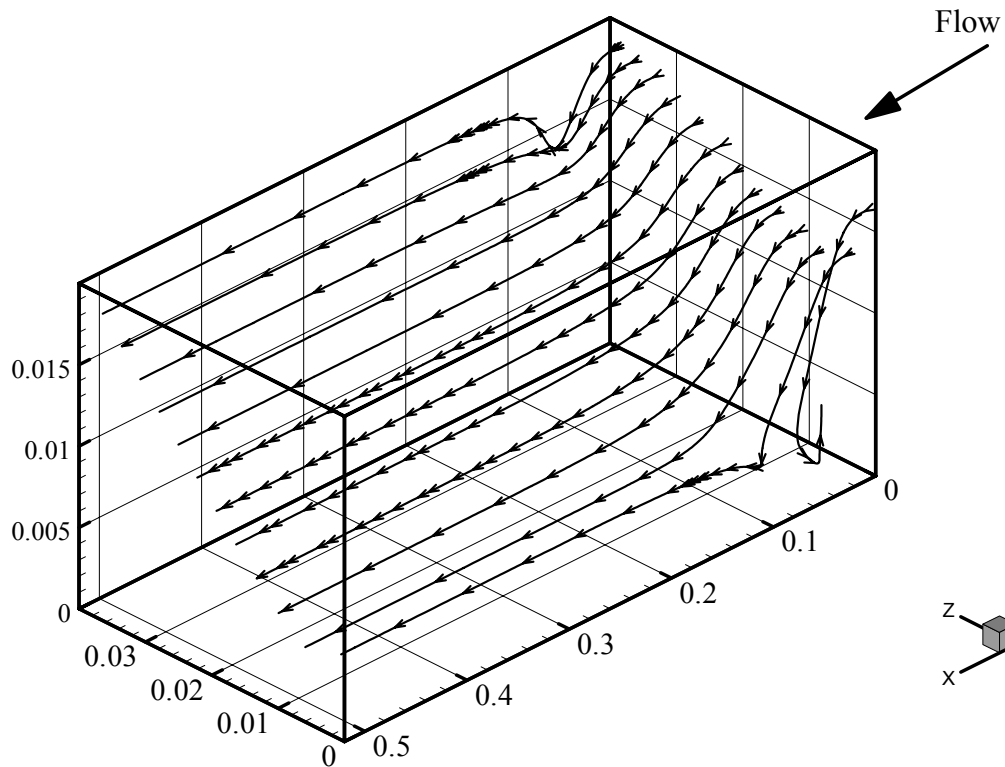


Fig. 7.2 Flow structures for a forced convective flow

In the span-wise central region the  $v$  and  $w$  components of the velocity are small and in order to satisfy continuity the magnitude of  $u$ -velocity increases resulting in a maximum in  $x_u$ -line along the span-wise central plane.

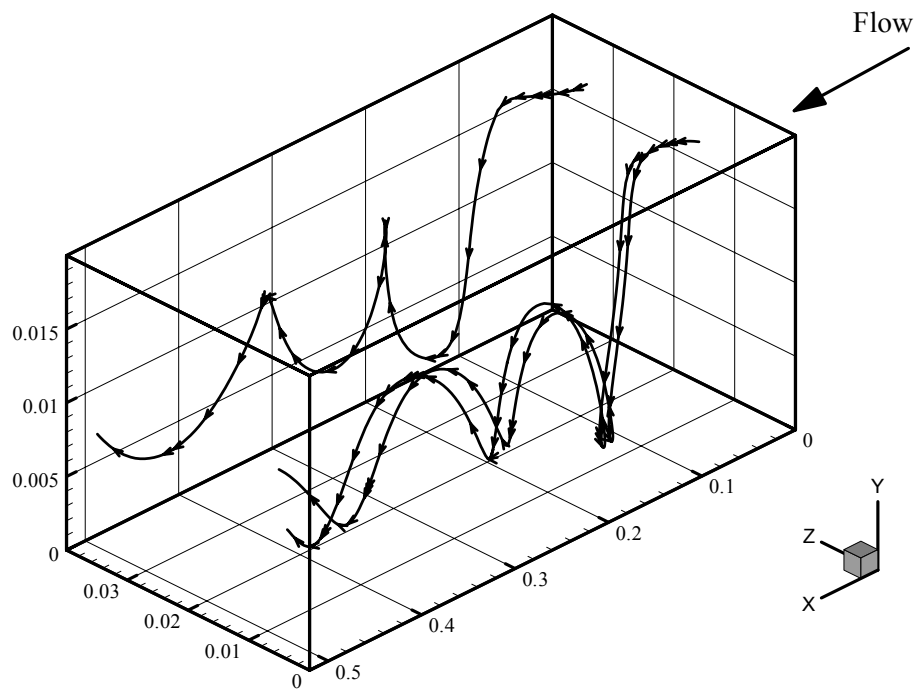


Fig. 7.3 Flow structures for a mixed convective flow  $Ri=1$

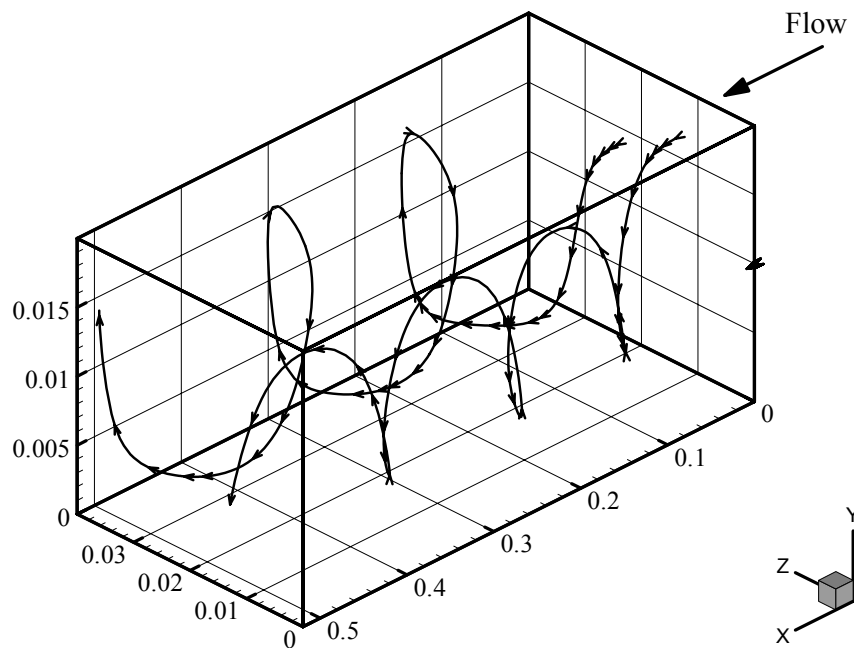


Fig. 7.4 Flow structures for a mixed convective flow  $Ri=2$

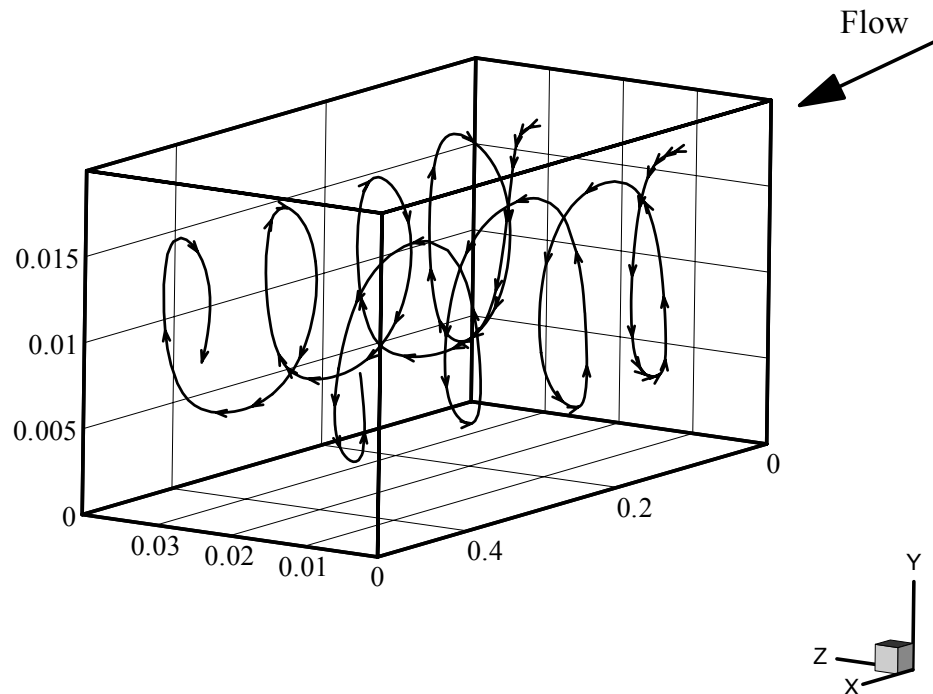


Fig. 7.5 Flow structures for a mixed convective flow  $Ri=3$

The averaged shear stress  $\tau_{wx}$  along the bottom wall is presented in Figure 7.6.

In Figure 7.6, the negative values, of the averaged shear stress, are associated with the primary re-circulation zone, and the point where  $\tau_{wx}$  changes from a negative to a positive value, could be interpreted as “the average reattachment point”. The location of this point is shifted upstream if  $Ri$  is increased and the farthest point downstream occurs for  $Ri=1$  as a consequence of the distribution for the  $x_u$ -line presented in Figure 7.1. After reaching its maximum value the  $\tau_{wx}$  monotonically decreases toward its asymptotically fully developed value at the channel exit.

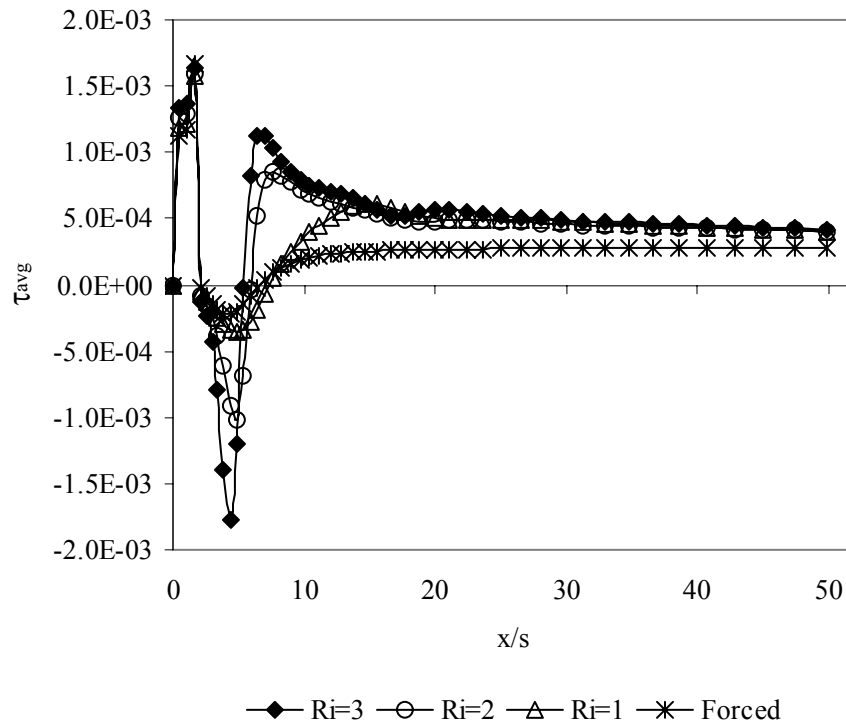


Fig. 7.6 Averaged shear stress  $\tau_{wx}$  for different Ri and pure forced convection

Figure 7.7 presents the average Nusselt number distribution for various cases considered in this study.

At the entrance of the horizontal backward-facing step channel the Nusselt number distribution has high values typical of the flow in the entry region; and then monotonically decreases until it reaches the backward-facing step end. In the vicinity of this zone the averaged Nusselt distribution presents a dramatic change due to the flow separation. In this sense, the hydraulic boundary layer and thermal boundary layer that started to develop at the channel duct entrance are abruptly interrupted. The tendency for

the averaged Nusselt number distribution is quite similar for all the study cases and higher values are associated to higher Ri as was expected.

The maximum value of the averaged Nusselt number occurs at the location of the “average reattachment point” accordingly; the location of the maximum average Nusselt number matches with the averaged reattachment point (Figure 7.6).

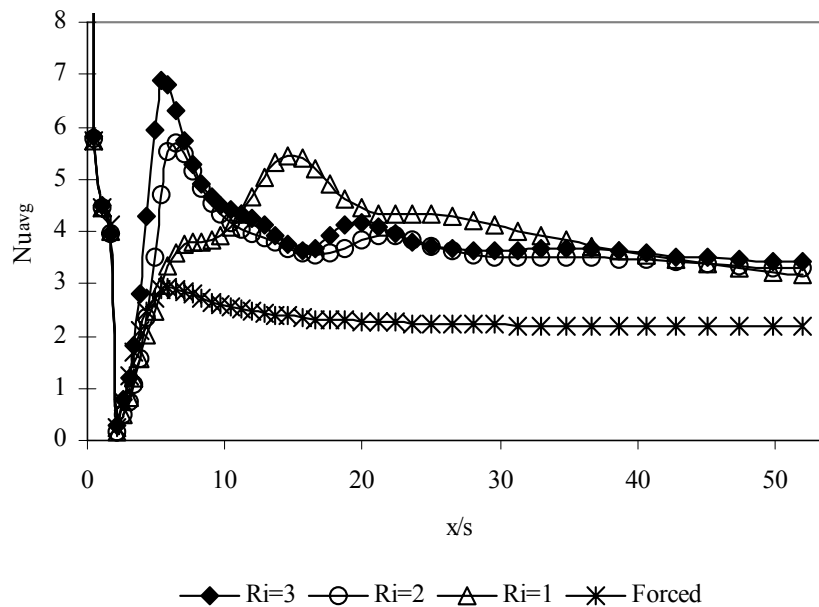


Fig. 7.7 Averaged Nusselt number distribution

The following section is dedicated to studying the effects of mixed convection on the three-velocity components of the flow over the horizontal backward-facing step heat.

### ***7.5.2 Development of the Three-Velocity Components under Mixed Convective Flow Conditions***

The analysis of the impact of the mixed convection in the developing flow is done by plotting the three-velocity components at specific planes.

The first case to be considered is for the u-velocity component alongside the central plane in the span-wise direction ( $z/W=0.5$ ). The u-velocity component is plotted as a function of the transverse axis (y-axis) at several constant planes in the stream-wise direction (x-direction) for the heating conditions in Figure 7.8.

As mentioned earlier, at the channel inlet ( $x/s=0$ ) the flow is considered to be a three-dimensional hydrodynamically fully developed flow.

In the vicinity of the step at  $x/s=2$ , the u-velocity component has a slight deviation from the fully developed flow. The major differences in these profiles, with respect to the ones at the channel inlet, occur at the corner of the step ( $y/s=0.5$ ). Similarly, in the bottom region of the channel ( $0 \leq y/s \leq 0.5$ ) negative u-velocity components are found. The most pronounced examples of this behavior are those for the highest  $Ri$  ( $Ri=3$ ).

The next stage to be discussed is for  $x/s=4.7$ . Here, the primary re-circulation zone attached to the backward-facing step is easily identified by the negative values of the u-velocity component in this zone.

The negative u-components are larger for  $Ri=3$  and  $Ri=2$  than for  $Ri=1$  and for pure forced convection. On the other hand the positive values for this velocity component are larger for pure forced convection than for any other case.

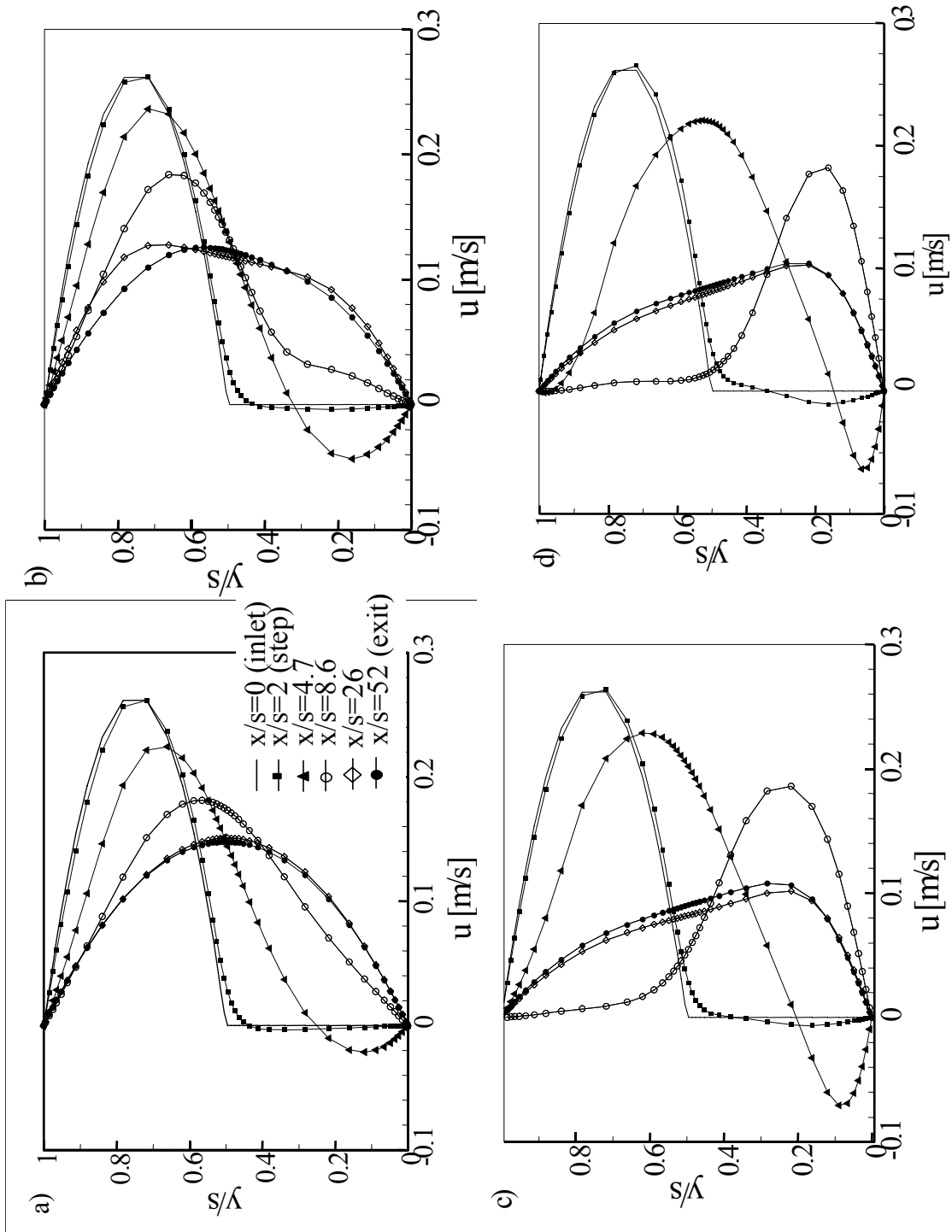


Fig. 7.8 u-velocity component at central plane  $z/W=0.5$  at different x-planes. a)  $Ri=0$ , b)  $Ri=1$ , c)  $Ri=2$ , d)  $Ri=3$



An important feature for  $Ri=2$  and  $3$  is that the size of the re-circulation zone in the transverse direction ( $y$ -direction) is shortened as  $Ri$  increases. In other words, the point for change from  $u$ -negative to  $u$ -positive is moving toward the bottom wall as  $Ri$  is increased. The reason for this particular behavior will be explained below.

At the plane  $x/s=4.7$ , Figure 7.8d reveals the presence of a small re-circulation zone attached to the channel top wall (roof) along the span-wise central plane. This effect extends until  $x/s=8.6$ . This particular behavior is found only for  $Ri=3$  and the only reasonable explanation attributed to this effect is the strength of the buoyancy forces.

At the middle of the channel ( $x/s=26$ ) the  $u$ -velocity component for pure forced convection starts to show a tendency similar to that of a fully developed velocity profile. Similarly for  $Ri=1$ ; however, for  $Ri=2$ , and  $3$  the  $u$ -velocity profile presents a distorted shape that has its maximum values in the vicinity of the channel's floor. The tendency to push the flow towards the bottom wall was discussed earlier for the plane  $x/s=4.7$ .

Viewing the plots in Figure 7.8, it becomes evident that the profile for the  $u$ -velocity component along the central plane in the span-wise direction remains basically unchanged as the axial position (stream-wise) moves from the middle central plane ( $x/s=26$ ) to the channel exit ( $x/s=52$ ). The profile for the  $u$ -velocity component for pure forced convection approaches the profile of a fully parabolic profile at the channel exit, as shown in Figure 7.8a.

At position ( $x/s=4.7$ ) for  $Ri=1$  (Figure 7.8b) the profile for the  $u$ -velocity component tends to form a parabolic profile. However, is evident that the maximum of the  $u$ -velocity component is not at the transverse central plane, but is moved slightly toward

the top half of the channel. This particular behavior can also be viewed in the flow structures in Figure 7.4.

A closer analysis of Figure 7.4, shows that for  $Ri=1$  the spiral flow structures at the channel exit tend to break down and form linear structures like a fully developed flow. By increasing the channel length it could be possible to have a parabolic profile at the exit for  $Ri=1$ .

Discussion of the u-velocity component is completed by studying the u-velocity profiles at the channel exit for  $Ri=2$  and  $3$ . For these two special cases the profile at the channel central plane ( $z/W=0.5$ ) presents a distorted shape that has the maximum values in the lower part of the channel. This comment has been remarked on more than once through this analysis and now the explanation for this behavior is presented with the help of Figures 7.2 and 7.3. In these two figures, the flow structures show the presence of a couple of symmetric spiral mixed convective rolls. In these two spirals, it is evident that the mixed convective flow is ascending toward the channel roof along the sidewall while coming down toward the bottom wall along the central plane in the span-wise direction. This is the reason why the u-velocity profile along the central span-wise plane for  $Ri=2$  and  $3$  is pushed down to the channel floor and the maximum component always appears at the lower part of the channel as can be appreciated in Figures 7.8c and 7.8d.

This theory is corroborated in Figure 7.9 which compares the u-velocity profiles at the channel exit for  $Ri=3$  at two different  $z/W$  positions. In this figure the maximum in the u-velocity profile is at a higher position ( $y/2H$ ) for the plane near the wall ( $z/W=0.05$ ) where the flow is ascending and is placed in a lower position at the central

plane ( $z/W=0.5$ ) where the flow is descending toward the bottom wall.

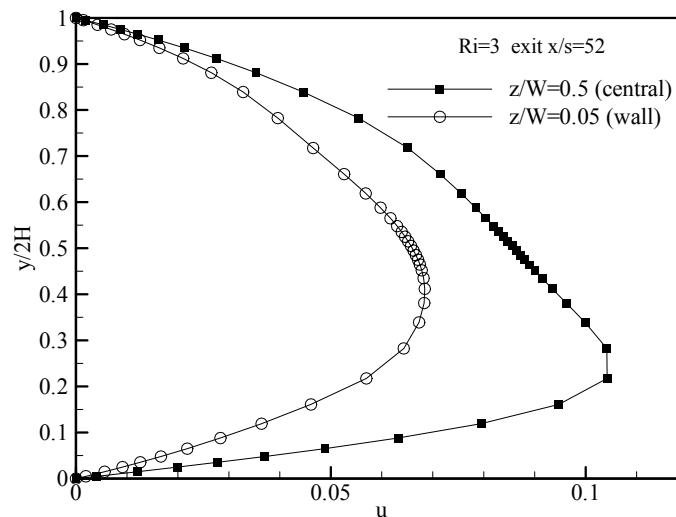


Fig. 7.9  $u$ -velocity profile at the channel exit at two different  $z/W$  planes  $Ri=3$

The transverse velocity component ( $v$ ), as a function of the span-wise distance ( $z/W$ ) at different constant stream-wise and constant transverse planes, is presented in Figure 7.10.

Figure 7.10a shows the velocity profile at the edge of the step ( $x/s=2$ ) for a constant transverse plane near the bottom wall ( $y/s=0.06$ ). Here, the  $v$ -velocity component profile presents positive values meaning that the flow is moving up. This effect is not only attributed to the buoyancy forces, but also due to the presence of the step wall normal to the stream-wise direction. The  $v$ -component values for  $Ri=3$  are almost 6 times the

values for pure forced convection, and is evident that the buoyancy forces have their impact in this region of the channel.

The effect of these positive values for the  $v$ -velocity component leads to a reduction in size of the primary re-circulation zone in both stream-wise and transverse directions.

Figure 7.10b shows the  $v$ -velocity distribution at the same  $y$ -constant plane as in Figure 7.10a near the bottom wall ( $y/s=0.06$ ), but at a farther downstream plane ( $x/s=4.7$ ). In this position the distributions for  $Ri=2$  and  $3$  show a similar behavior, while for  $Ri=1$  and pure forced convective flows the distributions remain almost constant having a value of  $v=0$  m/s. Analysis of this figure for the higher Richardson number cases, lends credence to the explained theory of convective rolls and the fluid ascending near the sidewalls ( $z/W=0$  and  $z/W=1$ ) while the fluid is displaced towards the bottom wall in the central region in the span-wise direction.

It is also clear that the buoyancy effects for  $Ri=2$  and  $3$  are strong and even inside of the re-circulation zone they considerably modify the  $v$ -velocity distribution.

The  $v$ -velocity distribution in a transverse plane near the top wall ( $y/s=1.94$ ) and adjacent to the step ( $x/s=2$ ) is presented in Figure 7.10c. The  $v$ -velocity distributions clearly show the propensity for the flow to displace toward the bottom wall along the span-wise ( $z$ ) direction. It is evident that for  $Ri=2$  and  $3$  some positive values for the  $v$ -velocity component are presented. This special behavior in the vicinity of the sidewall is due to the presence of the buoyancy forces which is not so for the cases  $Ri=1$  and  $0$ .

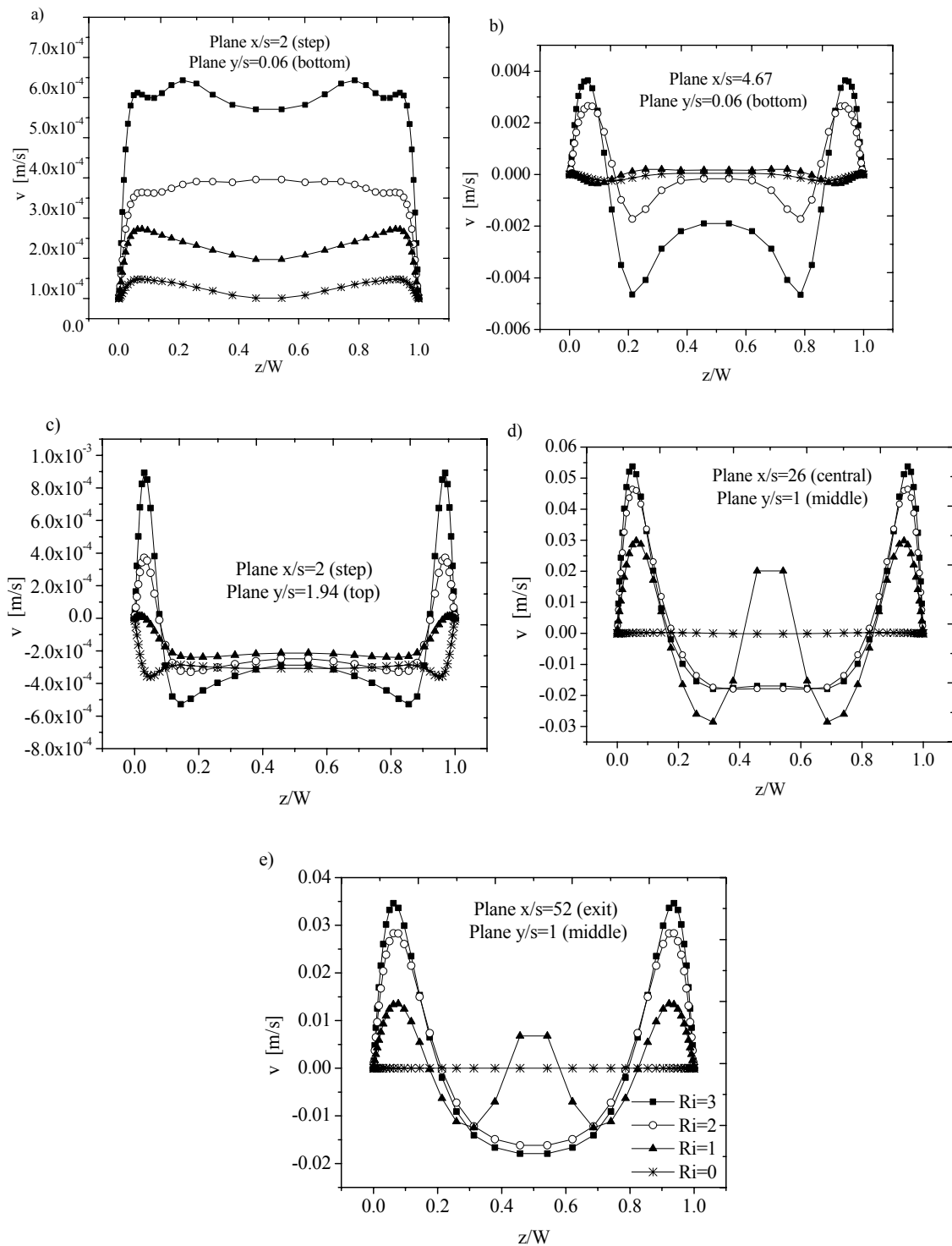


Fig. 7.10  $v$ -velocity component for different  $Ri$  at constant  $x$ - and  $y$ -planes. a)  $x/s=2$  &  $y/s=0.06$  b)  $x/s=4.7$  &  $y/s=0.06$  c)  $x/s=2$  &  $y/s=1.94$  d)  $x/s=26$  &  $y/s=1$  e)  $x/s=52$  &  $y/s=1$

In Figure 7.10d the  $v$ -velocity components for a central plane in the transverse direction ( $y/s=1$ ) and for the central plane of the channel in the stream-wise direction ( $x/s=26$ ) are plotted. It can be appreciated that for the pure forced convection the  $v$ -velocity component is equal to zero all along the span-wise distribution, thus it can be said that for this particular situation, the flow is approaching a fully developed flow condition. On the other hand for  $Ri=2$  and  $3$ , the  $v$ -velocity profiles in this specific zone are similar. But the  $v$ -velocity distribution deviates for  $Ri=1$ . In the case of  $Ri=1$ , the distribution gives the idea of an ascending flow structure at the central portion in the span-wise central portion of the channel.

Figure 7.10e shows the  $v$ -velocity distribution along a constant plane  $y/s=1$  at the channel exit. The  $v$ -velocity behavior is similar to Figure 7.10d discussed above. At the channel exit the  $v$ -component for pure forced convection is equal to zero and the flow structures report that for  $Ri=2$  and  $3$ , the flow is ascending in the vicinity of the side-wall and is descending in the central region. The consequence of this behavior was explained earlier (Figure 7.9).

Figure 7.11 shows  $w$ -velocity at two different constant  $y$ -planes ( $y/s=0.05$  and  $1.95$ ) and at two different constant  $x$ -planes ( $x/s=2$  and  $6.4$ ). The value of  $y/s=0.05$  corresponds to a transverse plane near the bottom of the channel while  $y/s=1.95$  corresponds to a transverse plane near the top of the channel. The value of  $x/s=2$  corresponds to a plane close to the step, while a value of  $x/s=6.4$  corresponds to a plane inside the primary re-circulation region.

An inverted symmetric behavior about the span-wise central plane was observed for

the  $w$ -velocity distribution (Figure 7.11). Along the central plane in the span-wise direction ( $z/W=0.5$ ) the value is equal to zero. Similarly, in the central zone it can be seen that the value for this component is extremely small even inside the primary re-circulation zone.

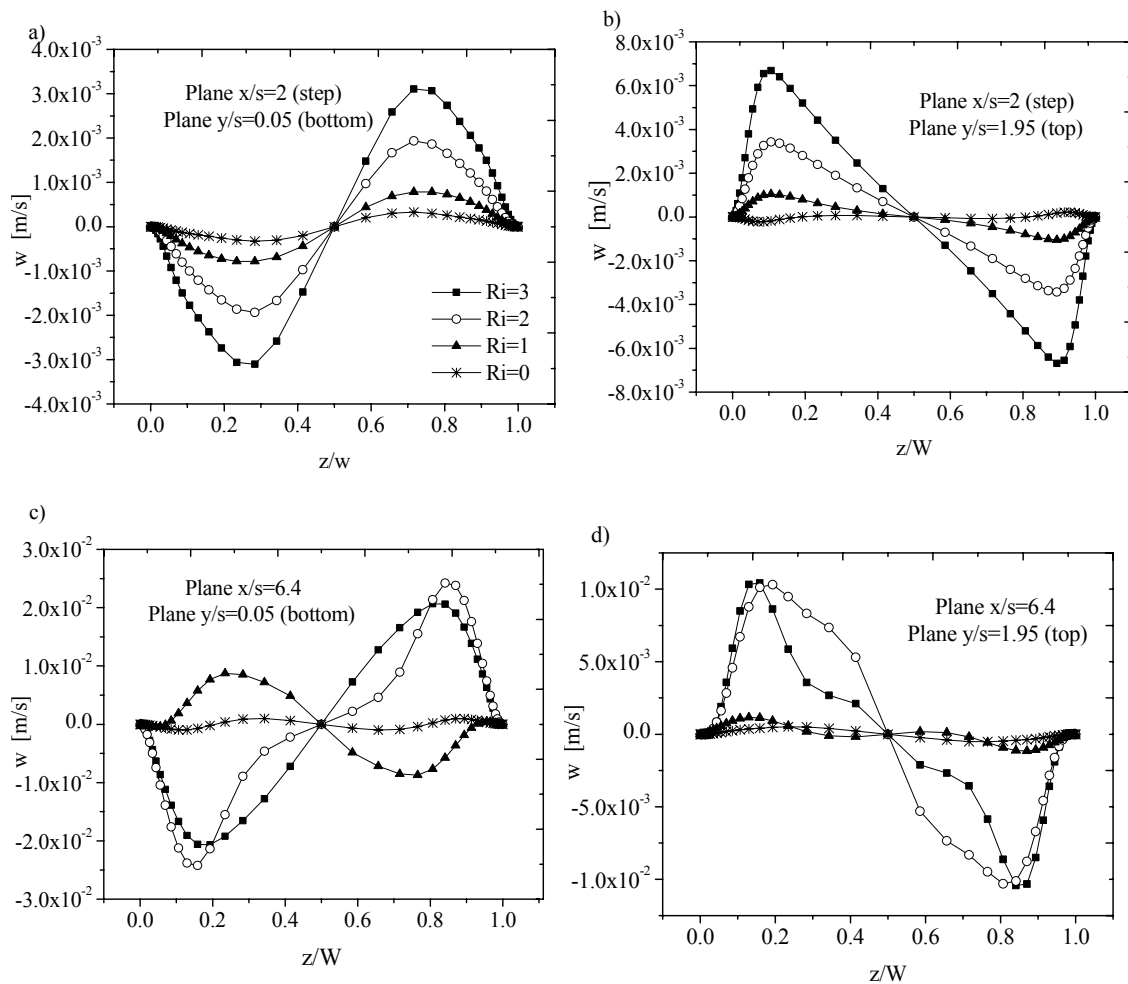


Fig. 7.11  $w$ -velocity profile at different  $x$ - and  $y$ -planes. a)  $x/s=2$  &  $y/s=0.05$  b)  $x/s=2$  &  $y/s=1.95$  c)  $x/s=6.4$  &  $y/s=0.05$  d)  $x/s=6.4$  &  $y/s=1.95$

Figure 7.11a shows the  $w$ -velocity distribution near the bottom of the channel at a constant stream-wise plane near the step ( $x/s=2$ ). It is clear from this figure that the flow is directed towards the sidewalls. A similar  $w$ -velocity distribution in a transverse plane near the top wall ( $y/s=1.95$ ) is presented in Figure 7.11b. This figure shows that the flow is directed towards the center of the channel. Thus, one can conclude the presence of two counter clock-wise convective rolls near the step.

Figures 7.11c and 7.11d show  $w$ -velocity distribution inside the primary re-circulation zone ( $x/s=6.4$ ). For pure forced convection ( $Ri=0$ ) the  $w$ -velocity components are nearly zero in both planes near the bottom and top of the channel. For  $Ri=1$  the variation of  $w$ -velocity is negligible in the plane near the channel top while Figure 7.11c indicates that the flow is directed towards the channel center in the plane close to the bottom of the channel.

For  $Ri=2$  and 3 the flow is directed toward the channel sidewalls in the region close to the channel bottom and flow is directed toward the channel center-line in the region close to the channel top wall. Thus confirming the presence of two counter clock-wise convective rolls.

The distribution for the  $w$ -velocity component, along the stream-wise direction for a constant span-wise plane ( $z/W=0.015$ ) along a constant transverse plane, adjacent to the bottom wall ( $y/s=0.05$ ), is presented in Figure 7.12.

The  $w$ -velocity components are strong in the vicinity of the step and inside the primary re-circulation zone ( $x/s \leq 10$ ), and the tendency is to pass flow toward the channel sidewalls as mentioned before. At the channel exit the  $w$ -velocity component



tends to an asymptotic value and then the variations in the  $w$ -component are not as significant as in the primary re-circulation zone.

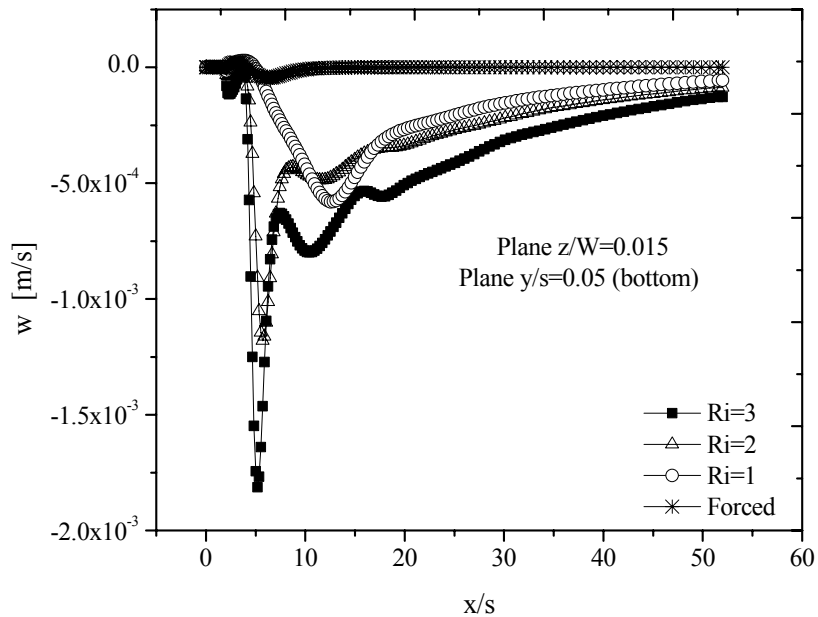


Fig. 7.12  $w$ -velocity component at a constant span-wise plane ( $z/W=0.015$ )

For pure forced convective flow the  $w$ -component reports a value equal to zero near the channel exit. On the other hand, for mixed convective flow, this velocity component reports non-zero negative values indicating that the flow is pushed toward the channel sidewalls as a consequence of the mixed convective rolls.

The strong presence of the  $w$ -velocity component inside the primary re-circulation

zone becomes clearly evident from Figure 7.12. Hence, the flow is a strong three-dimensional in mixed convective flows over a backward-facing step.

Figure 7.13 presents the w-velocity component along the stream-wise direction, but for plane  $z/W=0.93$  and a plane near the roof of the channel ( $y/s=1.92$ ). Contrary to the distribution presented in Figure 7.12, the flow tends to move to the channel span-wise central zone. This behavior is attributed to the spiral convective rolls. As can be seen in Figures 7.11 and 7.12 there is a considerable variation in the magnitude of the w-velocity component along the span-wise direction.

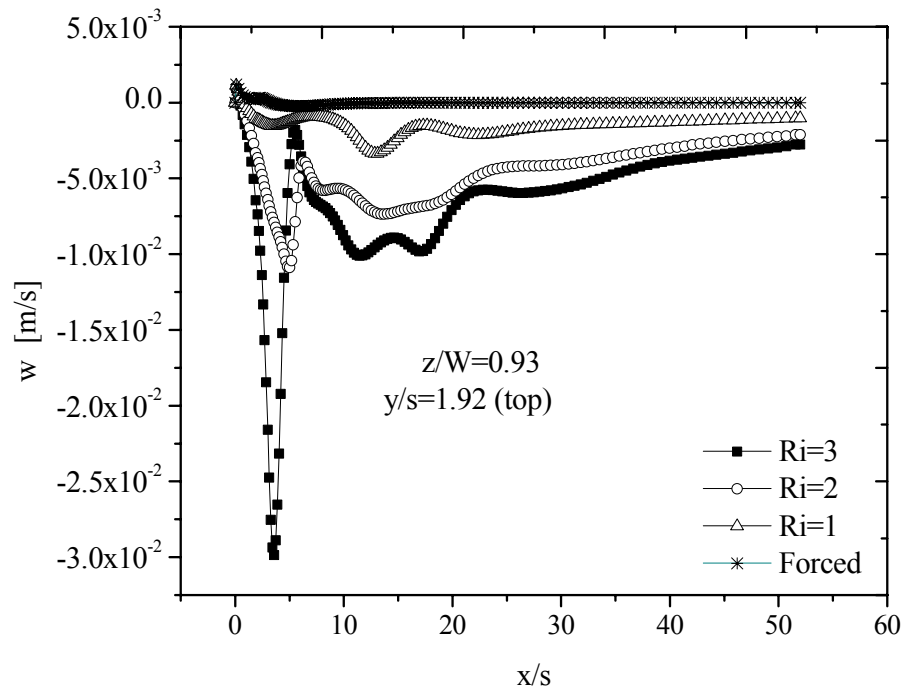


Fig. 7.13 w-velocity component at a constant span-wise plane ( $z/W=0.93$ )

### ***7.5.3 Temperature Fields for the Mixed Convective and Pure Forced Convective Flow***

Results for the temperature distribution within the computational domain for the mixed and forced convective flow are presented along different planes in Figures 7.14 to 7.17 for different  $Ri$  values.

Figure 7.14 shows the temperature contours for  $Ri=3$ . The zones for the highest temperatures are located near the bottom wall and in the vicinity of the step. This is because the bottom wall is heated and the backward-facing step is highly conducted ( $k_s=k_{Copper}=386$  W/m-K).

The temperature contours along the constant  $x$ -planes reveal that zones in the form of layers of high temperature are formed along the bottom and top walls. The high temperature near the bottom wall is a consequence of the boundary condition imposed for the computational domain, while the layer of high temperatures at the top wall is a consequence of the buoyancy effects.

It is evident from the temperature contour plots in the constant  $y$ -planes, that the temperature increases as flow approaches the channel exit. The temperature contour plot along the  $y=0.1$  plane shows that there are significant temperature gradients in the span-wise direction which is due to the presence of strong mixed convective rolls at  $Ri=3$ .

Temperature contours for a constant  $z$ -plane clearly shows that high temperatures occur in the bottom right-hand side corner. It also shows that the zones of high temperature in the top wall start very close to the channel inlet. So the mixed convective effects start to develop in the entry region of the channel.

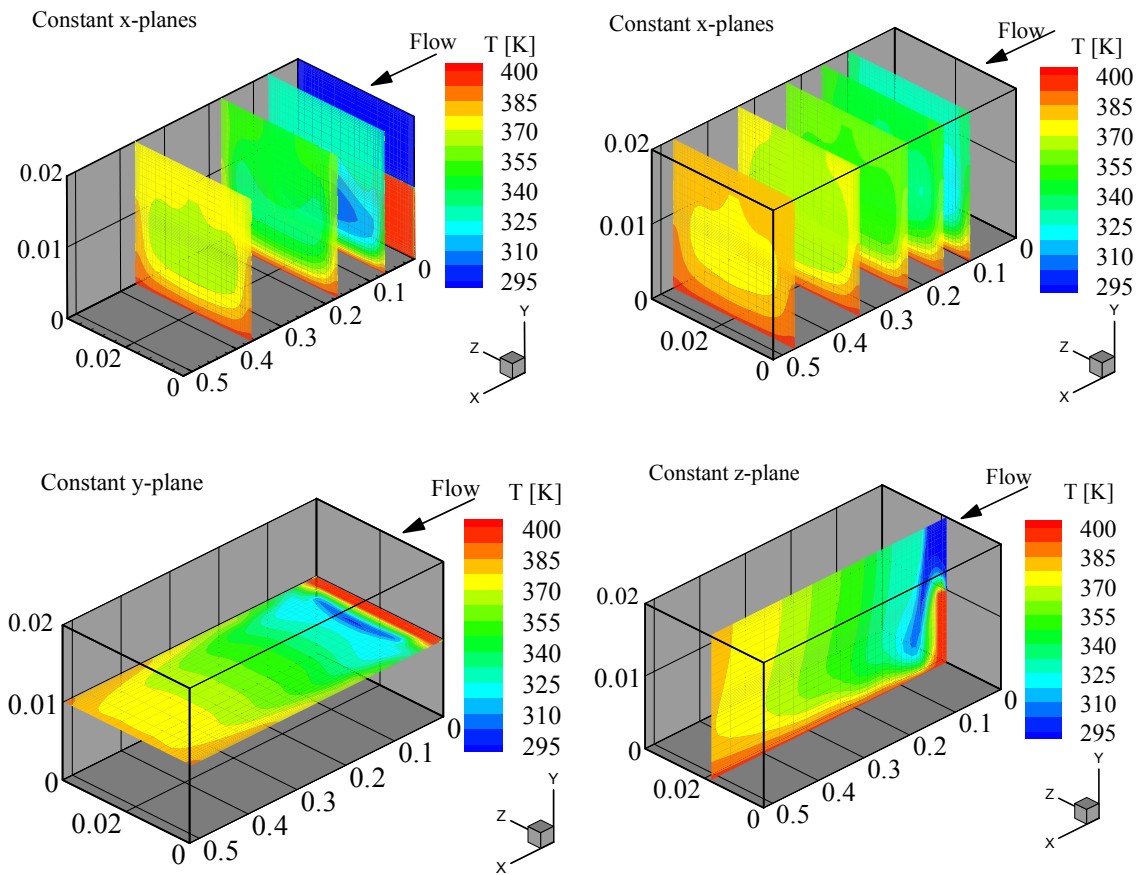


Fig. 7.14 Temperature distribution for  $Ri=3$  at different  $x$ -,  $y$ - and  $z$ -constant planes

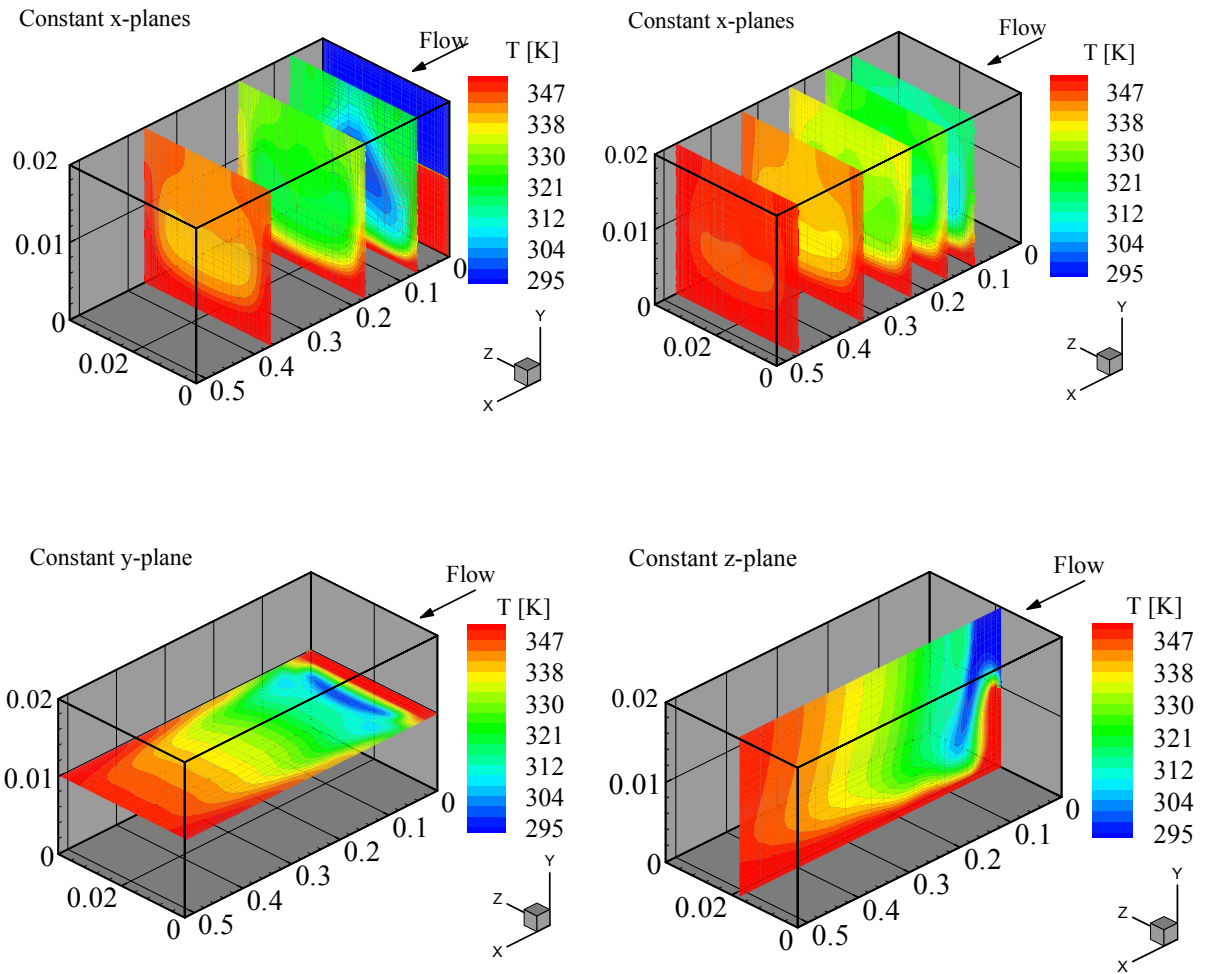


Fig. 7.15 Temperature distribution for  $Ri=2$  at different  $x$ -,  $y$ - and  $z$ -constant planes

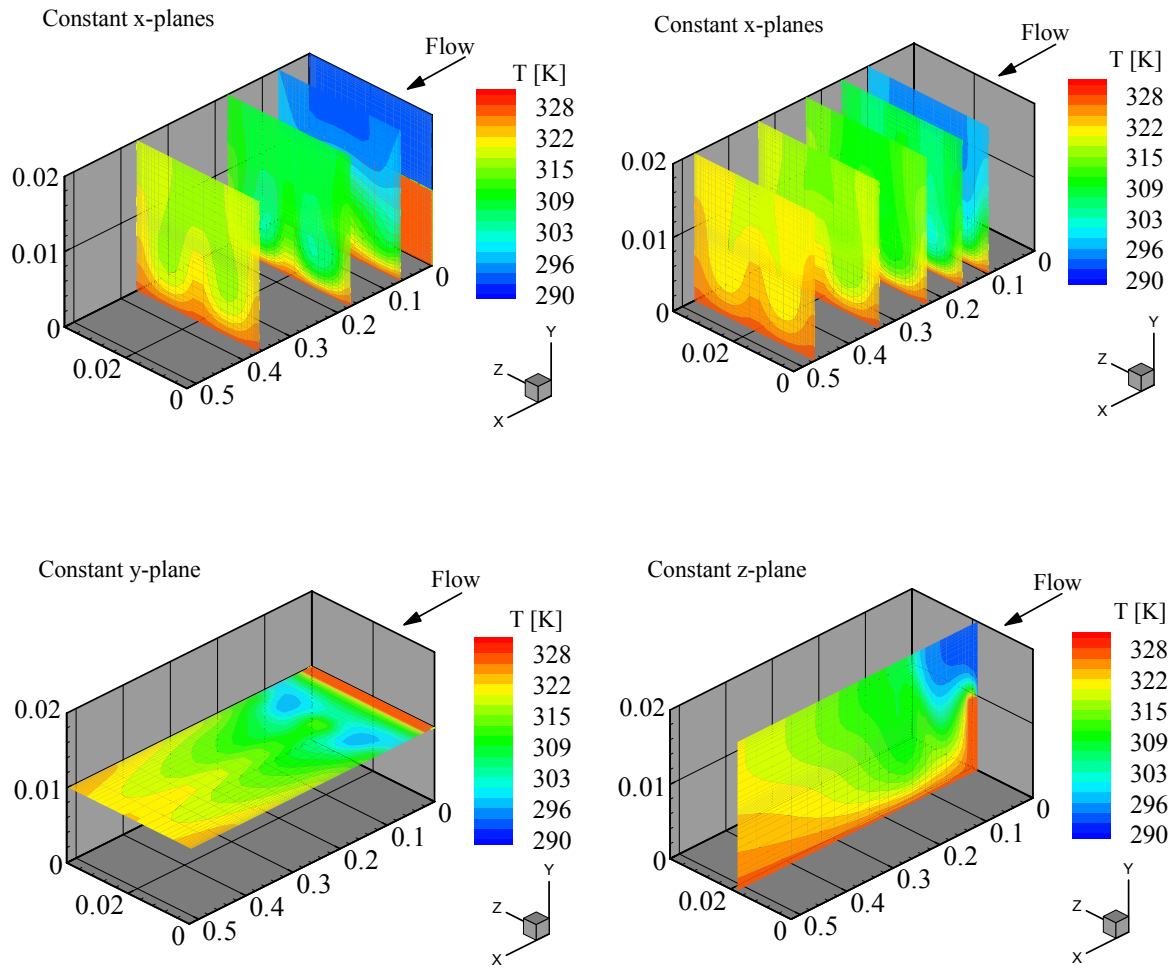


Fig. 7.16 Temperature distribution for  $Ri=1$  at different x-, y- and z-constant planes

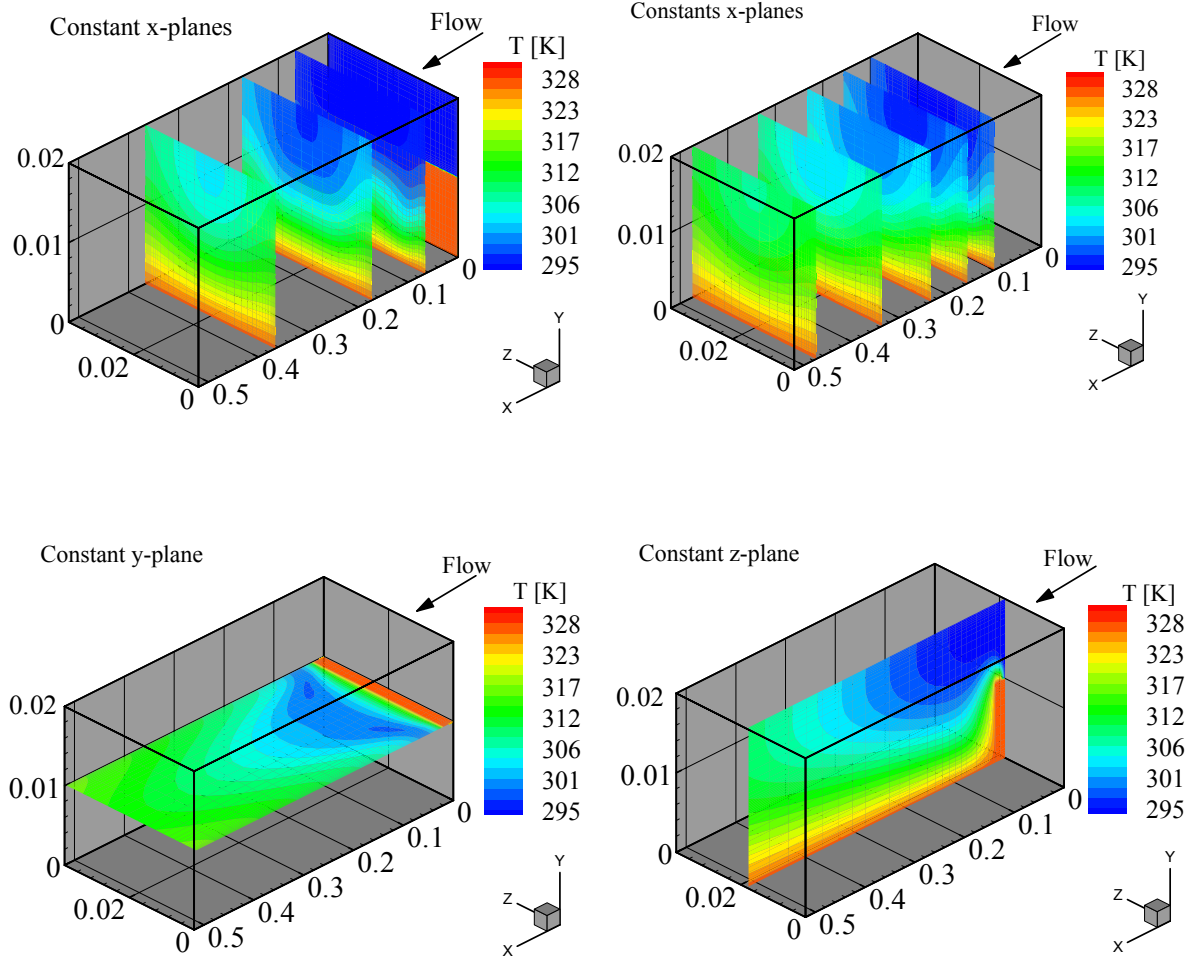


Fig. 7.17 Temperature distribution for  $Ri=0$  at different x-, y- and z-constant planes

Figure 7.15 presents the temperature distribution inside the computational domain for  $Ri=2$ . The temperature contour distributions are similar to the ones for  $Ri=3$ , hence no additional comments are warranted.

The temperature distribution contours for  $Ri=1$  are presented in Figure 7.16. In this case there is no evidence of high temperature fluid reaching the channel roof and the buoyancy effects for  $Ri=1$  are not strong enough to overcome the viscous forces.

The temperature contours for a  $z$ -constant plane reinforce the comment that no high temperature layer is found along the top wall. While the contours for the  $y$ -constant plane show the existence of temperature gradients along the  $z$ -coordinate direction.

For pure forced convective flow the temperature distribution is presented in Figure 7.17. The temperature contours show that the higher temperature is always near the bottom wall and in the vicinity of the backward-facing step. It is evident that at the channel inlet the temperature is low and it tends to increase as the fluid approaches the channel exit.

## **7.6 Impact of the Backward-Facing Step Thermal Conductivity on the Mixed Convective Flow**

In this section the influence of a thermally conductive backward-facing step is presented. The results were computed under the consideration of a mixed convective flow for  $Ri=2$  and the thermal conductivity ratio between the solid and fluid were varied from 10 to 10000. In this section,  $k_{Cu}=386$  W/m-K and  $k_{SS}=64$  W/m-K, which correspond to the thermal conductivity for Copper and Stainless Steel, respectively, and



the thermal conductivity for the air were defined before as  $k_{\text{air}}=0.0259$  W/m-K.

The temperature distribution for the central plane in the span-wise direction inside the block is presented in terms of contour plots in Figure 7.18 for all the cases.

Figure 7.18 shows that for a high conductivity ratio,  $k_s/k_f$ , the temperature inside the block is almost uniform and close to that temperature at the boundary condition as presented in Figures 7.18a-d.

In these figures it is also observed that at the edge of the step, small differences in temperature are found, but this difference is present for just a small portion in the block.

In Figures 7.18e and 7.18f the temperature gradients inside the block are greater compared to the previous cases. This is because the thermal conductivity for the block in these cases is low.

The effect of varying the thermal conductivity in the block does not impact the development of the velocity and temperature distribution for the mixed convective flow. This could be attributed to the fact that the block dimensions are relatively small compared to the channel dimensions. The ratio of channel length-step length in the stream-wise direction is equal to 25.

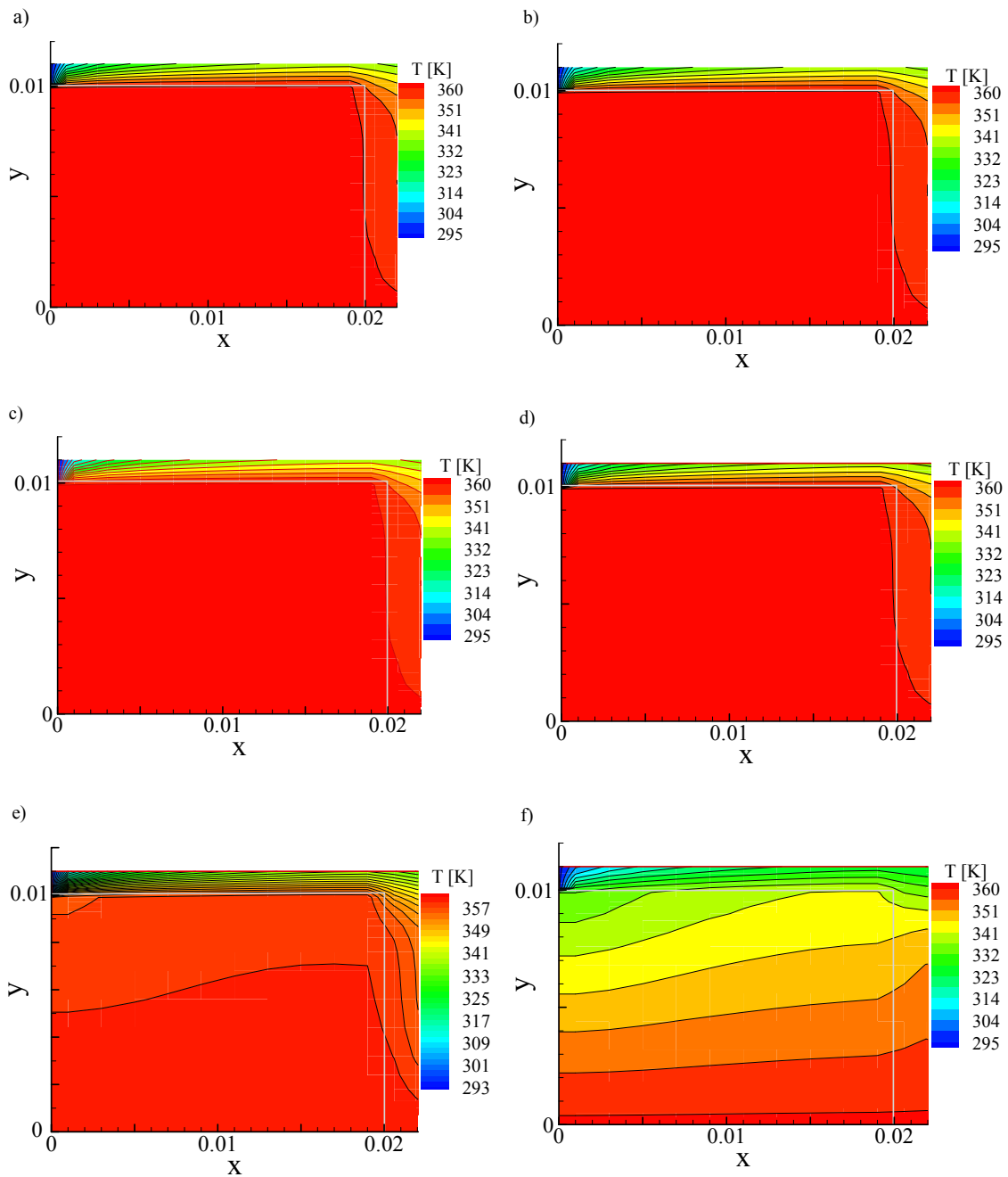


Fig. 7.18 Temperature contours inside the backward-facing step for different thermal conductivities at the z-central plane. a)  $k_s/k_{air}=k_{Cu}/k_{air}$  b)  $k_s/k_{air}=k_{SS}/k_{air}$  c)  $k_s/k_{air}=10000$  d)  $k_s/k_{air}=1000$  e)  $k_s/k_{air}=100$  f)  $k_s/k_{air}=10$

## CHAPTER VIII

### CONCLUSIONS

Numerical simulation for a mixed convective flow over a three-dimensional horizontal backward-facing step was presented for different Richardson parameters  $Ri=3$ , 2, and 1 and the results were compared with those of pure forced convective flow  $Ri=0$ . In all the cases the Reynolds ( $Re$ ) was fixed to be equal to 200.

As the buoyancy forces are increased by means of imposing larger  $Ri$ , the velocity field and the temperature distribution markedly differ from those of pure forced convective flow.

It was found that for buoyancy dominating mixed convective flows ( $Ri=3$  and 2) the  $x_u$ -line is shortened, while for equally dominant force-buoyancy mixed convective flows ( $Ri=1$ ) the  $x_u$ -line is pushed farther downstream when compared to pure forced convective flow ( $Ri=0$ ). The  $x_u$ -line is the limiting line for the primary re-circulation zone attached to the backward-facing step.

The location of the  $x_u$ -line has repercussions on the location of the maximum in the span-wise averaged Nusselt number distribution. This value is shifted upstream for  $Ri=3$  and 2 and is moved farther downstream for  $Ri=1$  when compared to the case for  $Ri=0$ .

The flow structures for mixed convective flows ( $Ri=2$  and 3) differ from those for  $Ri=1$  and for pure forced convection ( $Ri=0$ ). For  $Ri=1$  the forced convective and the mixed convective effects are equally dominant. At higher mixed convective strengths ( $Ri=2$  and 3) two convective rolls in the span-wise direction appear. The strength of the

buoyancy effects are also responsible for the shortening of the primary-re-circulation zone in both stream and transverse directions.

The temperature distributions are very different for  $Ri=2$  and  $3$  compared to those for pure forced convective ( $Ri=0$ ). For pure forced convection ( $Ri=0$ ) high temperatures are located near the bottom wall. The fluid temperature decreases in the transverse direction and increases in the stream-wise direction. For  $Ri=2$  and  $3$  high temperature fluid rises and a layer of fluid with high temperature and low density is located at the channel top wall. This layer increases in thickness as  $Ri$  is increased.

The impact of thermal conductivity of the backward-facing step on mixed convection was studied varying the ratio of the backward-facing step thermal conductivity to the fluid thermal conductivity. The parametric study showed that the thermal conductivity of the backward-facing step had no impact on the mixed convective flow. Higher temperature gradients within the backward-facing step were found for lower thermal conductivity ratios.

The numerical solution for three-dimensional geometries demands the use of high-performance computational resources. This becomes indispensable due to the complexity of the procedure for solving the mixed convective flow.

An OpenMP parallel implementation was proposed to solve the mixed convective flow over the three-dimensional horizontal backward-facing step.

The simulation results indicate that partitioning the computation across processors on a parallel machine drastically reduces the computational time. A linear speedup was observed up to 16 processors on the IBMp690. In many cases super linear speedup was

observed due to efficient cache usage.

For instance, the parallel performance measured by means of the speedup reported values around 18 on 16 processors. This results in an 18-fold reduction in computational time.

Research work involving a larger variety of Richardson numbers, different heating boundary conditions, and different geometrical dimensions of the channel could be addressed for future investigations. In addition, different parallel schemes using MPI can be considered for future work.

## REFERENCES

- [1] Kaufmann, W., and Smarr, L., 1993, *Supercomputing and the Transformation of Science*, Scientific American Library, New York.
- [2] Griebel, M., Dornseifer, T., and Neunhoffer, T., 1998, *Numerical Simulations in Fluid Dynamics*, SIAM, Philadelphia.
- [3] Aung, W., 1983, "Separated Forced Convection," *Proceedings of ASME–JSME Thermal Engineering Joint Conference*, **2**, Honolulu, pp. 494-515.
- [4] Chiang, T.P., Sheu, T.W.H., and Tsai, S.F., 1997, "Topological Flow Structures in Backward-Facing Step Channels," *Computers and Fluids*, **26**(4), pp. 321-337.
- [5] Nie, J.H., and Armaly, B.F., 2002, "Three-Dimensional Convective Flow Adjacent to Backward-Facing Step—Effects of Step Height," *Int. J. Heat and Mass Transfer*, **45**, pp. 2431-2438.
- [6] Iwai, H., Nakabe, K., and Suzuki, K., 2000, "Flow and Heat Transfer Characteristics of Backward-Facing Step Laminar Flow in a Rectangular Duct," *Int. J. Heat and Mass Transfer*, **43**, pp. 457-471.
- [7] Kawamura, T., 1974, "The Ignition Front of a Fuel Jet Flame Stabilized by a Step," *Combustion and Flame*, **22**, pp. 283-288.
- [8] Goldstein, R.J., Eriksen, V.L., Olson, R.M., and Eckert, E.R.G., 1970, "Laminar Separation, Reattachment, and Transition of the Flow over a Downstream-Facing Step," *J. Basic Engineering ASME*, **92D**(4), pp. 732-741.
- [9] Armaly, B.F., Durst, F., Pereira, J.C.F., and Schonung, B., 1983, "Experimental and

- Theoretical Investigation of Backward-Facing Step Flow,” *J. Fluid Mechanics*, **127**, pp. 473-496.
- [10] Aung, W., 1983, “An Experimental Study of Laminar Heat Transfer Downstream of Back-Step,” *J. Heat Transfer*, **105**, pp. 823-829.
- [11] Sparrow, E.M., and Chuck, W., 1987, “PC Solutions for the Heat Transfer and Fluid Flow Downstream of an Abrupt, Asymmetric Enlargement in a Channel,” *Numerical Heat Transfer*, **12**, pp. 19-40.
- [12] Blackwell, B. and Pepper, D.W., 1992, “Benchmark Problems for Heat Transfer Codes,” *Proceedings of the HTD-ASME Winter Annual Meeting*, **222**, Anaheim, pp. 1-89.
- [13] Shih, C., and Ho, C.M., 1994, “Three-Dimensional Recirculation Flow in a Backward Facing Step,” *J. Fluids Engineering*, **116**, pp. 228-232.
- [14] Steinthorsson, E., Liou, M.S., Povinelli, L.A., and Arnone, A., 1993, “Numerical Simulations of Three-Dimensional Laminar Flow over a Backward Facing Step: Flow near the Walls,” *Separated Flows FED-ASME, The Fluid Engineering Conference*, **149**, Washington, D. C., pp. 1-26.
- [15] Jiang, B.N., Hou, L.J., and Lin, T.S., 1993, “Least-Squares Finite Element Solutions for Three-Dimensional Backward-Facing Step Flow,” *NASA Technical Report Memorandum*, **106353**, pp. 1-21.
- [16] Williams, P.T., and Baker, A.J., 1997, “Numerical Simulations of Laminar Flow over a 3D Backward Facing Step,” *Int. J. Numerical Methods in Fluids*, **24**, pp. 1159-1183.

- [17] Armaly, B.F., Li, A., and Nie, J.H., 2003, "Measurements in Three-Dimensional Laminar Separated Flow," *Int. J. Heat and Mass Transfer*, **46**, pp. 3573-3582.
- [18] Carrington, D.B., and Pepper, D.W., 2002, "Convective Heat Transfer Downstream of a 3-D Backward-Facing Step," *Numerical Heat Transfer Part A*, **41**, pp. 555-578.
- [19] Nie, J.H., and Armaly, B.F., 2003, "Reattachment of Three-Dimensional Flow Adjacent to Backward-Facing Step," *Int. J. Heat Transfer*, **125**, pp. 422-428.
- [20] Armaly, B.F., Li, A., and Nie, J.H., 2002, "Three-Dimensional Forced Convection Flow Adjacent to Backward-Facing Step," *J. Thermophysics and Heat Transfer*, **16**, pp. 222-227.
- [21] Lin, J.T., Armaly, B.F., and Chen, T.S., 1991, "Mixed Convection Heat Transfer in Inclined Backward-Facing Step Flows," *Int. J. Heat and Mass Transfer*, **34**, pp. 1568-1571.
- [22] Hong, B., Armaly, B.F., and Chen, T.S., 1993, "Laminar Mixed Convection in a Duct with a Backward-Facing Step: The Effects of Inclination Angle and Prandtl Number," *Int. J. Heat and Mass Transfer*, **36**, pp. 3059-3067.
- [23] Abu-Mulaweh, H.L., Armaly, B.F., and Chen, T.S., 1993, "Measurements of Laminar Mixed Convection in a Boundary-Layer Flow over Horizontal and Inclined Backward-Facing Steps," *Int. J. Heat and Mass Transfer*, **36**, pp. 1883-1895.
- [24] Cheng, K.C., and Kimura, T., 1989, "Flow Visualization Experiments of Convective Instability Phenomena in the Laminar Separation Region Downstream of a Back-Step with Heating from Below," *HTD-Collected Paper in Heat Transfer, ASME Winter Annual Meeting*, **123**, San Francisco, pp. 23-33.



- [25] Lin, J.T., Armaly, B.F., and Chen, T.S., 1990, "Mixed Convection in Buoyancy-Assisting, Vertical Backward-Facing Step Flow," *Int. J. Heat and Mass Transfer*, **33**, pp. 2121-2132.
- [26] Blackwell, B.F. and Armaly, B.F., 1993, "Computational Aspects of Heat Transfer. Benchmark Problems," *HTD-ASME Winter Annual Meeting*, **258**, New Orleans, pp. 1-115.
- [27] Nie, J.H., and Armaly, B.F., 2002, "Buoyancy Effects on Three-Dimensional Convective Flow Adjacent to Backward-Facing Step," *J. Thermophysics*, **17**, pp. 122-126.
- [28] Li, A., and Armaly, B.F., 2000, "Mixed Convection Adjacent to a 3-D Backward Facing Step," *HTD- Proceedings of the ASME Heat Transfer Division*, **2**, Orlando, pp. 51-58.
- [29] Li, A., 2001, *Experimental and Numerical study of Three-Dimensional Laminar Separated Flow Adjacent to Backward-Facing Step*, Ph.D. Dissertation, Department of Mechanical Engineering, University of Missouri-Rolla.
- [30] Iwai, H., Nakabe, K., Suzuki, K., and Matsubara, K., 2000, "The Effects of Duct Inclination Angle on Laminar Mixed Convective Flows over a Backward-Facing Step," *Int. J. Heat and Mass Transfer*, **43**, pp. 473-485.
- [31] Iwai, H., Nakabe, K., Suzuki, K., and Matsubara, K., 1999, "Numerical Simulation of Buoyancy-Assisting Backward-Facing Step Flow and Heat Transfer in a Rectangular Duct," *Heat Transfer Asian Research*, **28**(1), pp. 58-76.
- [32] Abu-Mulaweh, H.I., 2003, "A Review of Research on Laminar Mixed-Convection

Flow over a Backward- and Forward-Facings Steps,” *Int. J. of Thermal Sciences*, **42**, pp. 897-909.

[33] Kays, W.M., and Crawford, M.E., 1993, *Convective Heat and Mass Transfer*, McGraw-Hill, Inc., New York.

[34] Incropera, F.P., and DeWitt, D.P., 1996, *Fundamentals of Heat and Mass Transfer*, John Wiley & Sons, Inc., New York.

[35] Kakac, S., and Yener, Y., 1995, *Convective Heat Transfer*, CRC Press, Inc., Boca Raton.

[36] Gebhart, B., 1988, *Buoyancy-Induced Flows and the Transport*, Hemisphere Pub. Corp., Washington, D.C.

[37] Yan, W.M., 1996, “Combined Buoyancy Effects of Thermal and Mass Diffusion on Laminar Forced Convection in Horizontal Rectangular Ducts,” *Int. J. Heat and Mass Transfer*, **39**, pp. 1479-1488.

[38] White, F.M., 1991, *Viscous Fluid Flow*, McGraw-Hill, Inc., New York.

[39] Schlichting, H., and Gersten, K., 2000, *Boundary-Layer Theory*, Springer-Verlag, Berlin.

[40] Özişik, M.N., 1985, *Heat Transfer. A Basic Approach*, McGraw Hill, Inc., New York.

[41] Burmeister, L.C., 1993, *Convective Heat Transfer*, John Wiley & Sons, Inc., New York.

[42] Moran, M.J., and Shapiro, H.N., 2000, *Fundamentals of Engineering Thermodynamics*, John Wiley and Sons, Inc., New York.

- [43] Ferziger, J.H., and Perić, M., 1997, *Computational Methods for Fluid Dynamics*, Springer-Verlag, Berlin.
- [44] Versteeg, H.K., and Malalasekera, W., 1995, *An Introduction to Computational Fluid Dynamics. The Finite Volume Method*, Prentice Hall, London.
- [45] Kreyszig, E., 1999, *Advanced Engineering Mathematics*, John Wiley and Sons, New York.
- [46] Patankar, S.V., 1980, *Numerical Heat Transfer and Fluid Flow*, Taylor & Francis, Philadelphia.
- [47] Meyer, C., 2000, *Matrix Analysis and Applied Linear Algebra*, SIAM, Philadelphia.
- [48] Harlow, F.H., and Welch, E., 1965, "Numerical Calculation of Time-Dependent Viscous Incompressible Flow of Fluid with Free Surface," *Physics of Fluid*, **8**(12), pp. 2182-2189.
- [49] Kim, S.H., 1993, *A Numerical Analysis of Convective Heat Transfer in Channels Simulating Electronic Components*, Ph.D. Dissertation, Department of Mechanical Engineering, Texas A&M University, College Station.
- [50] Barret, R., Berry, M., Chan, T., Demmel, J., Donato, J., Dongara, J., Eijkhout, V., Pozo, R., Romaine, C., and Vorst, H., 1994, *Templates for the Solution of Linear Systems: Building Blocks for Iterative Methods*, SIAM, Philadelphia.
- [51] Chapra, S.C., and Canale, R.P., 2004, *Numerical Methods for Engineers with Software and Programming Applications*, McGraw Hill, New York.
- [52] Ravi Sankar, S., Mees, P.A.J., and Nandakumar, K., 1993, "Development of Three-Dimensional, Streamwise-Periodic Flows in Mixed-Convection Heat Transfer," *J.*

- Fluid Mechanics, **225**, pp. 683-705.
- [53] Shah, R.K., and London, A.L., 1978, *Laminar Flow Forced Convection in Ducts*, Academic Press Inc., New York.
- [54] Incropera, F.P. and Schutt, J.A., 1985, "Numerical Simulation of Laminar Mixed Convection in the Entrance Region of Horizontal Rectangular Ducts," *Numerical Heat Transfer*, **8**, pp. 707-729.
- [55] Thompson, J.F., Warsi, Z.U.A., and Mastin, C.W., 1985, *Numerical Grid Generation. Foundations and Applications*, Elsevier Science Publishing Co., Inc., New York.
- [56] Patankar, S.V., 1991, *Computation of Conduction and Duct Flow Heat Transfer*, Innovative Research, Inc., Minneapolis.
- [57] Kumar, V., Grama, A., Gupta, A., and Karypis, G., 1994, *Introduction to Parallel Computing. Design and Analysis of Algorithms*, The Benjamin-Cummings Publishing Company, Inc., New York.
- [58] May, J.M., 2001, *Parallel I/O for High Performance Computing*, Morgan Kaufmann Publishers, San Francisco.
- [59] Chandra, R., Dagum, L., Kohr., Maydan. D., McDonald, J., and Menon, R., 2001, *Parallel Programming in OpenMP*, Morgan Kaufmann Publishers, San Francisco.
- [60] Ellis, T.M.R., Philips, I.R., and Lahey, T.M., 1998, *FORTRAN 90 Programming*, Addison Wesley Publishers, New York.
- [61] Xi, C., and Han, P., 2000, "A Note on the Solution of Conjugate Heat Transfer Problems Using SIMPLE-like Algorithms," *Int. J. Heat and Fluid Flow*, **21**, pp. 463-

467.

- [62] Guo, Z., and Anand, N.K., 1997, "Three-Dimensional Heat Transfer in a Channel with a Baffle in the Entrance Region," *Numerical Heat Transfer Part A*, **31**, pp. 21-35.

## VITA

Juan Gabriel Barbosa Saldana was born in Mexico City, Mexico. He received his B.S. degree in March 1996 and M.S. degree in January 2000 from the National Polytechnic Institute in Mexico (IPN, Mexico). He joined Texas A&M University in spring 2001 to pursue his Ph.D. degree.

Mr. Barbosa Saldana has been an Academic Professor at the National Polytechnic Institute in Mexico since September 1999.

Mr. Barbosa Saldana's permanent address in Mexico City is:

Avenida Instituto Politecnico Nacional s/N

Unidad Profesional Adolfo Lopez Mateos

Edif. 5, 3<sup>er</sup> piso, LABINTHAP

Col. Lindavista. C.P. 07738,

Mexico D.F. Mexico